PHYSICAL PROPERTIES OF GEOMATERIALS WITH RELEVANCE TO THERMAL ENERGY GEO-SYSTEMS

A Thesis
Presented to
The Academic Faculty

by

Shahrzad Roshankhah

In Partial Fulfillment
of the Requirements for the Degree
Doctor of Philosophy in the
School of Civil and Environmental Engineering

Georgia Institute of Technology
May 2015

PHYSICAL PROPERTIES OF GEOMATERIALS WITH RELEVANCE TO THERMAL ENERGY GEO-SYSTEMS

Approved by:

Dr. J. Carlos Santamarina, Advisor
School of Civil and Environmental Engineering
Georgia Institute of Technology

Dr. Kimberly E. Kurtis
School of Civil and Environmental Engineering
Georgia Institute of Technology

Dr. J. David Frost
School of Civil and Environmental Engineering
Georgia Institute of Technology

Dr. Paul W. Mayne
School of Civil and Environmental Engineering
Georgia Institute of Technology

Dr. Christian Huber
School of Earth and Atmospheric Sciences
Georgia Institute of Technology

Date Approved: March 23, 2015

To my parents: Roshanak Rasulian and M. Reza Roshankhah

ACKNOWLEDGEMENTS

Professor J. Carlos Santamarina, who has played the role of a kind father, a great teacher, an honest friend and a wise mentor for me throughout the last few years, deserves my sincere appreciation. I wish him a satisfying and productive career for many years to come because I believe that he will continue changing students' lives and the future of many people in the world at different levels. This PhD dissertation was made possible by the generous financial support from The Department of Energy and The Goizueta Foundation.

I am grateful to my thesis committee members for their insightful comments and suggestions: Dr. David Frost, Dr. Christian Huber, Dr. Kimberly Kurtis and Dr. Paul Mayne. Also, I would like to express my sincere thanks to other dear professors who have taught me inspiring science, exciting engineering courses, and life lessons at Georgia Tech, Amirkabir University of Technology, and Semnan University: Dr. Carlos Santamarina, Dr. Paul Mayne, Dr. David Frost, Dr. Dominik Assimaki, Dr. Mustafa Aral (CEE), Dr. Christian Huber (EAS), Dr. Sheldon Jeter (ME), Dr. Beryl Martinson (CETL), Dr. Abbas Soroush, Dr. Roozbeh Shafipour and Dr. Ali Kafi among others.

Constructive discussions and ingenious suggestions of my colleagues in the Particulate Media Research Laboratory (PMRL) cannot be overestimated. I appreciate their continuous encouragement and friendship: Dr. Hosung Shin, Dr. Minsu Cha, Dr. Sheng Dai, Dr. Seunghee Kim, Dr. Cesar Pasten, Dr. Junbong Jang, Dr. Song Hun Chong, Dr. Efthymios Papadopolous, Dr. Marco Terzariol, Aswathy Siwaram, Liang Lei, Seth Mallett, Junghee Park, Qi Liu, Adrian Garcia, Zhonghao Sun, Yuanjie Shen, and Nicolas Augsburger. Indeed, we have become a true family! I eagerly look forward to working with them on great ideas in the future throughout my career. I am very grateful for interacting with visiting scholars in PMRL: Dr. Norimasa Yoshimoto, Dr. Andrea Mezencevova, Dr. Lucio Cruz, Dr. Xingwei Ren, Dr. Cuiying Lu, Stefanous Athanasopoulos, Yan Ma, Miriam Martin Ruiz, and Dr. Enrique Asanza Izquierdo. All my dear friends and colleagues in the geosystems department, the Iranian community, the Schools of Civil and Environmental Engineering, Electrical Engineering, and Mechanical Engineering have made my family's stay in the U.S. very pleasant, and I truly express my gratitude to all of them.

Special thanks to Andrew Udell and his team in the School of Civil and Environmental Engineering (CEE) research laboratory and machine shop. The experimental devices developed in this thesis would not exist without Mr. Udell's fine expertise and willing

cooperation. Many thanks go to the CEE's IT crew, especially Michael Anderson and Winston Wang, who always made things easier with their prompt and high quality service. I would also like to extend my sincere thanks to the helpful and hardworking administrative staff: Jenny Eaton, Crystal Hanson, Carol Maddox, and Lisa Tuttle. Additionally, I deeply appreciate the valuable effort of staff in the Women Resource Center, especially Rome Lester, Colleen Riggle, and Karen Yiu, for their unquestionable commitment to women's success and excellence in Georgia Tech. Thanks must also go to the kind staff in the main library and its divisions, especially Lori Critz and Elizabeth Rolando, for their informative workshops and efficient follow up support. I gratefully acknowledge the guidance of the staff in the Center for Career Discovery and Development, especially Robbie Ouzts and Elaine Damon. Many thanks also go to the staff in the Office of International Education, especially Katie Tudini and Meghan Popick for their unwavering support for international students.

Surely, nothing could have been achieved without the nurturing guidance from my dear parents, Roshanak Rasulian and M. Reza Roshankhah, who shaped my core values on serving the society with love and honesty. I am indebted to them to the end of my life. My dearest sisters, Shiva and Sheida; sisters-in-law, Samaneh and Somaye; and parents-in-law, Khatoon Moradi and Mostafa Mohammadi, have always been an invaluable source of encouragement. Furthermore, not only this thesis, but also every other positive step in my future is devoted to my family, my dear husband Kami Mohammadi and my lovely son Ryan.

I would also like to extend my deep appreciation to my past colleagues in the Bureau of Technical Execution System - Vice Presidency for Strategic Planning and Supervision, Tehran, Iran, whose unconditional and continuous support led me to pursue my dreams and make them a reality: Behnaz Pourseyed, Ali Tabaar, Farzaneh Agharamezanali, Nasrin Abolhasani, Alireza Tutunchi, Khashayar Esfandiari, Mahmood Zafari, Ali Ghafourian and many more who will never be forgotten. Sincere thanks also go to my dearest friends in Atlanta: Pei-Yin Chu, Sevil Elmas, Elnaz Younesian, Dorsa Elmi, and Atefeh Eftekhari for their friendship and support to my family. We have indeed started a beautiful life-long friendship.

TABLE OF CONTENTS

LIST OF TABLES

LIST OF FIGURES

SUMMARY

Energy related geo-systems involve a wide range of engineering solutions from energy piles to energy geo-storage facilities and waste repositories (CO_2, nuclear). The analysis and design of these systems require proper understanding of geo-materials, their properties and their response to extreme temperature and high stress excitations, the implications of mixed-fluid conditions when contrasting fluid viscosities and densities are involved, the effect of static and cyclic coupled hydro-thermo-chemo-mechanical excitations, and rate effects on the response of long design-life facilities.

This study places emphasis on thermal geo-systems and associated physical properties. Uncemented soils and rocks are considered. The research approach involves data compilation, experimental studies and analytical methods. Emphasis is also placed to engineer geomaterials in order to attain enhanced performance in energy geo-systems.

The thermal conductivity and stiffness of most geomaterials decrease as temperature increases but increase with effective stress. This macroscale response is intimately related to contact-scale conduction and deformation processes at interparticle contacts. Pore-filling liquids play a critical role in heat conduction as liquids provide efficient conduction paths that can diminish the effects of thermal contact resistance. Conversely, grains and fluids can be selected to attain very low thermal conductivity in order to create mechanically sound thermal barriers. In the case of rock masses, heat (and gas) recovery can be enhanced by injecting fluids at high pressure to cause hydraulic fractures. Scaled experiments reveal the physical meaning of hydraulic fractures in pre-structured rocks (e.g., shale) and highlight the extensive self-propped dilational distortion the medium experiences. This result explains the higher production rate from shale gas and fractured geothermal reservoirs that is observed in the field, contrary to theoretical predictions.

CHAPTER 1

INTRODUCTION

1.1. MOTIVATION

The world's energy needs have increased significantly during the last two centuries (Figure 1.1). This trend is a consequence of the fast population growth and increased per capita demand. Conventional energy resources rely more than 85% on non-renewable, CO_2 emitting fossil fuels. Thus, we need to enhance current production methods and develop alternative energy resources.

Environmental challenges related to fossil fuels center around the emission of greenhouse gases (CH_4 and CO_2), and ensuing global warming. Consequences include arctic ice melting, pH and ionic concentration changes in seawater, sea level rise and its effect on coastal infrastructure.

The development of a sustainable system requires a detailed reanalysis of our current carbon economics (petroleum, coal, natural gas, and heavy oil); properly designed CO_2 sequestration strategies and other energy-related waste disposal and field remediation); and more emphasis on renewable energy resources (solar, tidal, wind, geothermal).

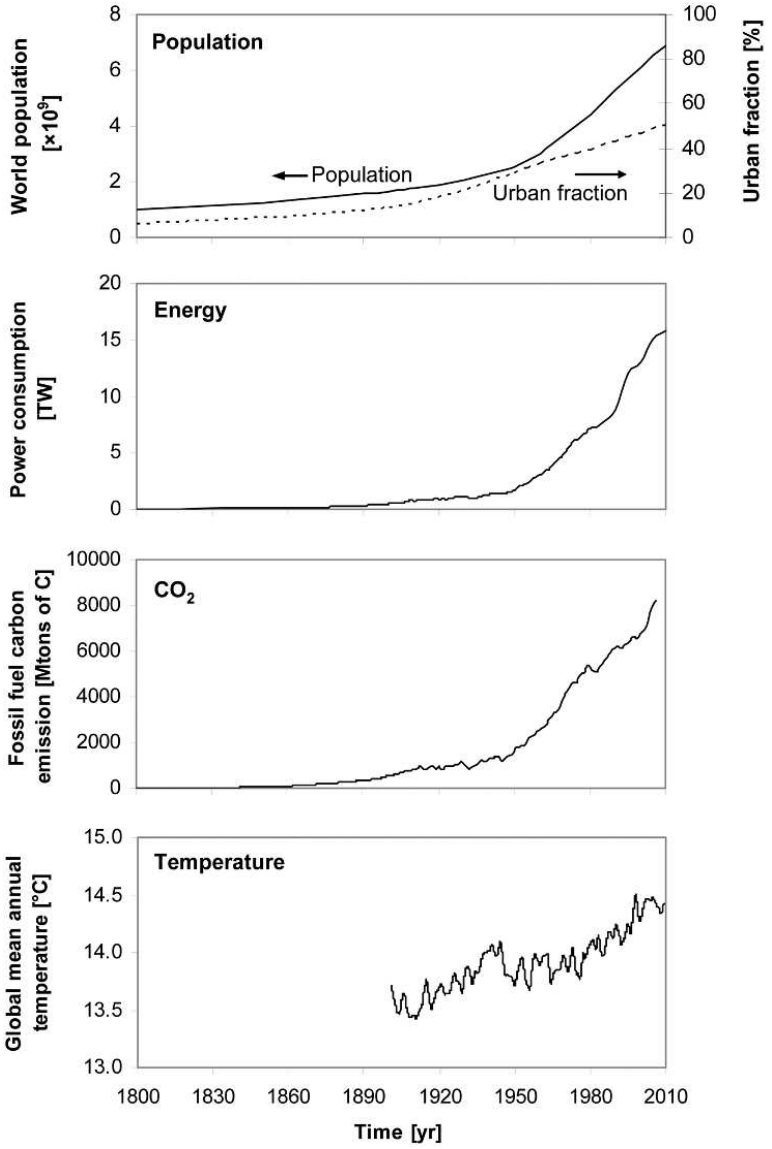

Figure 1.1. Global increase in population, energy consumption, CO_2 emission, and temperature for the last two centuries (Fragaszy et al., 2011 - Data from United Nations, Agency of Natural Resources and Energy, and Climate Research Unit at University of East Anglia).

Geotechnical engineers can play a central role in harnessing renewable energy sources (e.g., geothermal energy and wind turbine foundation design), energy storage (e.g., compressed air energy geo-storage), and energy waste disposal (e.g., CO_2, fly ash,

and nuclear waste geological deposition). However, conditions encountered in these energy-related applications are different from classical geotechnical problems; for example (Terzaghi lecture, 2014):

- Extreme temperatures: either low temperatures such as in the case of methane gas recovery from hydrate-bearing sediments (~4 ˚C) and liquified natural gas storage (-162 ˚C), or high temperature as in thermal energy geo-storage (~500 ˚C) and deep geothermal energy reservoirs (~350 ˚C).
- High overburden stresses, for example in deep geothermal reservoirs (>50 MPa).
- Extreme pore fluid density and viscosity: very high in oil sands and very low in subcritical CO_2 storage.
- Mixed fluid conditions: CO_2 sequestration, methane hydrate recovery, geothermal energy extraction, compressed air energy storage, oil recovery.
- Repetitive mechanical, thermal, chemical and hydraulic loads such as cyclic humidity, temperature and hydraulic gradients in compressed air energy storage, deep geothermal energy recovery, cyclic thermal extraction of oil sands, and repetitive mechanical loads on the foundations for wind turbines.

The proper design and operation of energy geo-systems requires a comprehensive knowledge about geo-materials subjected to the extreme conditions noted above, as well as the potential development of engineered geo-materials to satisfy performance requirements in energy geo-systems.

1.2. THESIS ORGANIZATION

The behavior of geomaterials subjected to extreme temperature and stress determine the long-term performance of energy geo-systems. Published data for thermal properties of geomaterials are compiled and interpreted in terms of underlying

phenomena in chapter 2. Physics-inspired models are proposed to capture the material response in terms of governing parameters.

Chapters 3 and 4 explore the evolution of thermal conductivity and compressibility for several natural and artificial granular materials in order to engineer sediments with extreme thermal conductivity and good mechanical properties. Chapter 3 documents the effect of state of stress and the use of conductive metal coatings to treat sand particle surfaces. Other natural and artificial granular materials are tested. The evolution of their compressibility and thermal conductivity are presented and compared according to other properties. Physical models are proposed to predict the thermal conductivity and dry mass density evolution for each material with stress.

The inter-particle coordination number determines heat conduction in dry granular materials. Dry granular mixtures made of different fractions of two different grain sizes of silica sand are tested to explore the effect of coordination in Chapter 4. The presence of liquids can increase the thermal conductivity of a soil specimen by one order of magnitude. Mechanisms responsible for heat transfer at solid-liquid interfaces are investigated in chapter 4 as well. Models are developed to predict the evolution of compressibility and thermal conductivity in both dry and water-saturated sediments.

Chapters 5 and 6 focus on exploring some mechanical, thermal, and hydraulic properties of particular geo-materials that will help more efficient extraction of oil and gas from soft sandstones and fractured shale formations. The temperature- and stress-dependent compressibility, small strain stiffness, and thermal conductivity of oil sands from the Orinoco belt in Venezuela are investigated in Chapter 5. On the other hand, Chapter 6 documents a study designed to understand resource (water, gas, heat) recovery

from tight, fractured formations with low permeability that have been “hydraulically fractured” using high pressure viscous liquid injection. Emphasis is placed on the far-field response of a pre-structured medium that has been subjected to an opening-mode discontinuity, and the role of its internal structure. Improvements in fluid conductivity are analyzed using mathematical/geometrical tools and experimental observations.

Salient conclusions and recommendations for future research are presented in Chapter 8.

1.3. REFERENCES

Fragaszy, R. J., Santamarina, J. C., Amekudzi, A., Assimaki, D., Bachus, R., Burns, S. E., Cha, M., Cho, G. C., Cortes, D. D., Dai, S., Espinoza, D. N., Garrow, L., Huang, H., Jang, J., Jung, J. W., Kim, S., Kurtis, K., Lee, C., Pasten, C., Phadnis, H., Rix, G., Shin, H. S., Torres, M. C., and Tsouris, C. (2011). "Sustainable Development and Energy Geotechnology - Potential Roles for Geotechnical Engineering." KSCE Journal of Civil Engineering, 15(4), 611-621.

United Nations: Nations-http://esa.un.org/unpp

Agency of Natural Resources and Energy, and Climate Research Unit in University of East Anglia: http://www.cru.uea.ac.uk/cru/

CHAPTER 2

THERMAL CONDUCTIVITY OF GEOMATERIALS AT HIGH TEMPERATURE AND EFFECTIVE STRESS

2.1. INTRODUCTION

The geothermal gradient originates in radioactivity in the crust, tectonism and residual formation heat. The temperature gradient varies between 10 to 60 ˚C per km of depth in the continental crust (25-45 km), yet the geothermal gradient can exceed 60 ˚C/km in the thinner oceanic crust (5-8 km) (Hurter and Schellschmidt, 2003). Extreme and mean trends for temperature T [˚C] versus depth z [km] follow (Figure 2.1 - Schwab, 1974; Seipold, 1995):

$$T_{ave} = 17 + 36.53z - 0.7986\,z^2 + 0.00964\,z^3 \quad (2.1)$$

$$T_{max} = 17 + 17.5z - 0.0694\,z^2 \quad (2.2)$$

$$T_{min} = 17 + 55.56z - 1.528z^2 + 0.01929z^3 \quad (2.3)$$

Because of the geothermal gradient, energy extraction or storage in deep geological formations require reservoir development and operation at high temperature and high stress. For example, deep geothermal reservoirs are 5-10 km deep and experience 200-to-350 ˚C and stresses as high as 100-to-200 MPa.

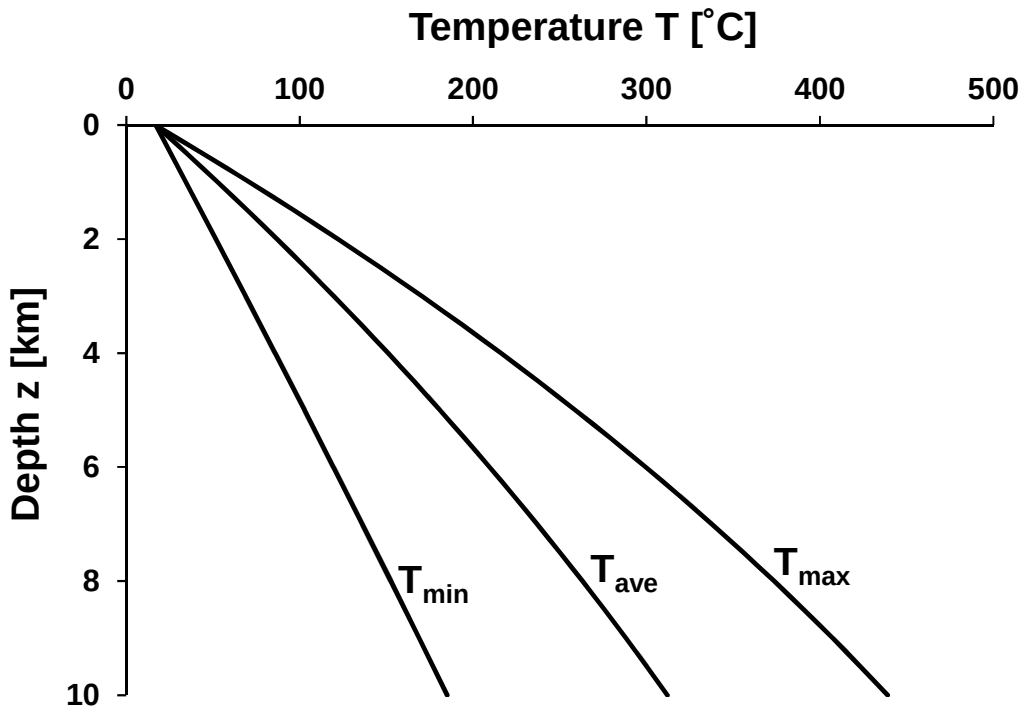

Figure 2.1. Geothermal gradient: temperature versus depth (Schwab, 1974).

The properties of monomineralic rocks at high temperature and stress may be predicted from the mineral properties; however, crystals may form with different crystallographic orientation so that the global response may change with temperature and stress. This is clearly the case when polymineralic rocks are subjected to high temperature and stress as differential thermal expansion and incompatible strains of various minerals create thermal cracks or increase the internal stresses depending on the boundary conditions.

The thermal and mechanical properties of intact rocks at high temperature and high stress conditions are studied herein. Published data for several geothermal reservoirs around the world were reviewed to compile a database on the physical properties of common rock types. The database mostly contains: granite, sandstone, volcanic tuff,

quartzite, granodiorite, andesite, gneiss, quartz monzonite and rhyolite. Some other common rocks such as rock salt and shale were added for completness and in view of other potential applications such as thermal energy geo-storage, nuclear waste repositories, and shallow geothermal foundations. Intact rocks considered in this study may include randomly distributed intra- and inter-crystalline fissures.

Physical grain-scale processes responsible for observed trends are suggested. thereafter, physically-inspired constitutive models are proposed to capture the material response in numerical simulations.

2.2. THERMAL CONDUCTIVITY - CONCEPTS

Conduction, convection and radiation are responsible for heat transfer in rocks. The other two phenomena are: convection and radiation. Convection prevails in fluids and it arises from mass density changes associated with increased temperature. Convection is negligible in geomaterials with small pore size or fracture aperture of $d<0.6$ mm (Thalmann, 1950; Woodside, 1958). Radiation does not need a material medium to transfer heat, but it becomes relevant at high temperatures. That depends on the surface characteristics and emissivity. Radiative heat transfer is negligible up to 550 ˚C in granulite (Ray et al., 2008), 880 ˚C for a mafic granulite (Kukkonen et al., 1999). In summary, conduction is the dominant heat transfer process in intact rocks with small pores and micro-farctures subjected to temperatures less than 500 ˚C.

The heat flux Q [J/s] per area A [m^2] in a medium with thermal conductivity k [$W.m^{-1}.K^{-1}$] subjected to a temperature gradient $\partial T/\partial x$ [K/m] is (Fourier's heat law):

$$Q = kA\frac{\partial T}{\partial x} \tag{2.4}$$

2.2.1. Thermal Conductivity of Non-metallic Solids

Heat is conducted by electrical carriers in metals (free electrons) and by lattice waves in non-metallic solid materials (phonons). Phonons are the fundamental mode of heat conduction in rocks. Atoms in crystals vibrate about their equilibrium positions. The vibration amplitude increases with temperature and can propagate as a wave or phonon. The propagation velocity can be anisotropic due to crystallographic arrangement. Scattering causes energy loss. The extent of scattering determines the mean free path L [m], which is the distance when the energy of the wave is reduced to e^{-1} of its initial value. The atomic mean free path is L = 30 Å for NaCl and L = 60 Å for quartz at T = 0 ˚C (Tritt, 2004).

The Thermal conductivity of a perfect isotropic crystal k [$W.m^{-1}.K^{-1}$] is a function of its lattice heat capacity C_P [$kJ.kg^{-1}.K^{-1}$], the group mean velocity of phonons V [$m.s^{-1}$] (sound velocity), the mass density of crystal ρ [$kg.m^{-3}$], and mean free path of phonons L [m] based on Debye's approximation (Tritt, 2004):

$$k = \frac{1}{3} C_P V \rho L \tag{2.5}$$

Heat transfer in hindered by phonons scattering at defects (crystal defects, grain boundaries, impurities) and from phonon collisions that affect the mean free path. The elastic wave velocity and mass density of minerals reflect similar processes that also affect their thermal conductivity. Dense minerals with higher stiffness such as quartz exhibit higher thermal conductivity than weaker minerals such as feldspars. Overall, the thermal conductivity increases from basic rocks (contain plagioclase feldspar, pyroxene, amphibole, olivine, kaolinite, and clays) to intermediate rocks (contain andesite and feldspars) and to acidic rocks (quartz, orthoclase feldspar, felsite - Scorer, 1950).

2.3. THERMAL CONDUCTIVITY OF ROCKS

The thermal conduction in fractured rocks takes place through the intact blocks, across the fracture plane and contact points, and along liquid-filled paths. Discontinuities between rock blocks add thermal resistance; hence, the thermal conductivity of fractured rocks is smaller than that of a continuous material. Heat conduction through fractured rock depends on its structure (fracture spacing and aperture), fracture thermal resistance (controlled by degree of cementation, degree of liquid-saturation, state of stress), thermal conductivity of components (mineral composition, pore-filling fluids) and temperature (Walsh and Decker, 1966).

2.3.1. Thermal Conductivity of Rocks, Minerals, and Fluids – Ranges

Tables 2.1 and 2.2 present values for mass density and thermal conductivity of common rocks and rock-forming minerals at room temperature and atmospheric pressure unless specified otherwise (Note: the heat capacity, thermal diffusivity and volumetric thermal expansion of rocks and rock-forming minerals are listed in Tables A-1 and A-2, Appendix A). If available, properties are reported in two directions: parallel and perpendicular to the crystallographic axis of rock-forming minerals, and parallel and perpendicular to bedding plane and fracture planes of rocks. It can be observed that minerals have a broad range of physical properties that reflects their atomic structure. In particular, quartz has a very high thermal conductivity k = 10 $W.m^{-1}.K^{-1}$ and a high coefficient of volumetric thermal expansion $\beta = 31\times10^{-6}\ ^{\circ}C^{-1}$. The thermal conductivity of rocks rich in quartz (felsic rocks) is higher than other rocks because of the high thermal conductivity of quartz compared to other rock-forming minerals. For example, quartzite with over 90% quartz content has a thermal conductivity k = 6 $W.m^{-1}.K^{-1}$ while most

other rocks with lower quartz content have a thermal conductivity between k=1.5 $W.m^{-1}.K^{-1}$ and k=3.5 $W.m^{-1}.K^{-1}$. Rocks rich in magnesium and iron (ultramafic), such as basalt and gabbro, show lower thermal conductivities than those rich in quartz and alumina, such as granite. Rocks consist of various minerals and fabrics as a result of formation conditions: depth, temperature, availability of chemical species (Pribnow et al., 1996; Cho et al., 2009).

Mono-minerallic salt rock (NaCl) with a very regular crystallographic structure explains its high thermal conductivity k = 5.5 $W.m^{-1}.K^{-1}$ compared to those that are a mixture of crystalline and amorphous minerals such as basalt, sandstone and Rhyolite that may contain some amorphous silica (opal).

The thermal conductivity of solid grains k_s [$W.m^{-1}.K^{-1}$] can be estimated by the volumetric content of each mineral and their thermal conductivity using the geometric mean relationship (Table 2.3). Quartz k = 10 $W.m^{-1}.K^{-1}$ dominates and other components may be assigned an average value k = 2.85 $W.m^{-1}.K^{-1}$. Other averaging relationships (harmonic and arithmetic mean) were derived assuming a series or parallel configuration of the various mineral components (Table 2.3). These estimations work well for isotropic fine- and medium-grained rocks such as Rhyolite rather than coarse-grained rocks such as granite (Kukkonen and Lindberg, 1998).

In general, thermal conductivity of rocks strongly correlates with their quartz content, but it does not correlate with their density because quartz has a high thermal conductivity, average: 7.7 $W.m^{-1}.K^{-1}$, but relatively low density, 2630 $kg.m^{-3}$ (Kukkonen and Lindberg, 1998).

Table 2.1. Selected properties of common rocks.

Rock Name	Mineral Composition	Type and General Description	Mass Density ρ [kg/m^3]	Thermal conductivity k [W.m^{-1}.˚C^{-1}]
Granite	K-feldspar (Orthoclase): 50-20% Na-feldspar(Plagioclase): 15-20% Quartz: 20-30% Mica (muscovite/biotite): 10-20% Amphibole (hornblende) or Pyroxene: 5-10%	Very common felsic (light color) - acidic, intrusive (coarse-grained), polycrystalline plutonic igneous rock. No bedding plane but broken by planar fractures parallel to the ground surface: joint sets	2330-2940	1.7 – 4.0
Syenite	Orthoclase feldspar Plagioclase feldspar Hornblende Mica Quartz	Plutonic igneous rock Felsic	2440-2860	2.2 (T = 50˚C)
Albitite	Mostly albite Some quartz, muscovite, garnet, apatite	Plutonic (dike) igneous rock Coarse-grained	2609	2.0 (T = 50˚C)
Pyroxenite	Pyroxene: >95%	Plutonic (dike) igneous rock ultrabasic	2240-3330	4.6 (T=0˚C) 3.9 (T=50˚C)

Table 2.1.Continued. Selected properties of common rocks.

Rock Name	Mineral Composition	Type and General Description	Mass Density ρ [kg/m^3]	Thermal conductivity k [W.m^{-1}.˚C^{-1}]
Granodiorite	K-feldspar (Orthoclase): 5-20% Na-feldspar(Plagioclase): 45-20% Quartz: 20-30% Mica (muscovite/biotite): 20-10% Amphibole (hornblende): 10-20%	Plutonic igneous rock. Intermediate (between felsic and mafic). Intrusive (coarse-grained).	2530-2940	2.5-2.8
Gabbro	Ca-feldspar (Plagioclase): 50-0% Pyroxene: 35-70% Olivine: 15-30% Some amphiboles	Plutonic igneous rock Mafic (dark-color) - basic Intrusive (coarse-grained) Also called “black granite”	2260-3340	2.1-2.6
Diabase	Similar to Gabbro	Also called: “Microgabbro” or “Dolerite”	2962-3013	2.1-2.5 (T=50˚C)
Dunite	Pyroxene: <10% Olivine: >90% Some chromite	Plutonic igneous rock Ultramafic or ultrabasic	3253-3269	2.8 4.18-4.77 (T=50˚C)
Serpentinite	Serpentine: >90%	Plutonic igneous rock Formed by early alteration of silica-deficient (olivine-rich)	2240-3270	-
Quartz Monzonite	K-feldspar: 50% Quartz: 50% Some biotite and hornblende	Plutonic igneous rock intermediate	2637	2.92 (T=50˚C)

Table 2.1.Continued. Selected properties of common rocks.

Rock Name	Mineral Composition	Type and General Description	Mass Density ρ [kg/m^3]	Thermal conductivity k [W.m^{-1}.˚C^{-1}]
Anorthosite	Plagioclase feldspar: >90% Pyroxene, Olivine, Magnetite	Plutonic igneous rock Acidic	2704-2740	1.69-1.88 (T=50˚C)
Diorite	K-feldspar (Orthoclase): 0-5% Ca-feldspar(Plagioclase): 45-65% Quartz: 20-0% Mica (muscovite/biotite): 15-5% Amphibole (hornblende): 20-25%	Plutonic igneous rock. Intermediate (between felsic and mafic). Intrusive (coarse-grained).	2430-3160	2.2-2.5
Andesite	Similar to Diorite	Volcanic igneous rock Extrusive (fine-grained) Intermediate	1560-2990	1.9-2.3
Rhyolite	Similar to Granite	Volcanic igneous rock. Acidic The extrusive (fine-grained) equivalent to Granite. Vesicular (isolated pores)	1360-2740	1 (T=300˚C)
Basalt	Similar to Gabbro. Ca-feldspar: labradorite; clinopyroxene: augite; iron ore: titaniferous magnetite; Some olivine, quartz, hornblende, nepheline, orthopyroxene, opal	Volcanic igneous rock, Basic Bimodal crystal size (porphyritic texture): fine-grained crystals and phenocrysts (much larger than the background), pervious. equivalent to Gabbro	1780-3060	1.7-2.1

Table 2.1.Continued. Selected properties of common rocks.

Rock Name	Mineral Composition	Type and General Description	Mass Density ρ [kg/m^3]	Thermal conductivity k [W.m^{-1}.˚C^{-1}]
Tuff	Variable (may contain all types of silicate minerals)	Consolidated volcanic ash. Analogous to sandstone Product of explosive volcanic eruptions	1410-2940	0.5 – 2.5
Quartzitic Sandstone	Quartz: >90%	Clastic sedimentary rock lithified sand	1510-3000	5.7 (T=0˚C) 5.1 (T=50˚C)
Shale	Clay-rich: 60.9% Quartz: 30.8% Feldspars: 4.5% Fe-oxides: 0.5% Other minerals: 2% Organic matter: 1%	Clastic sedimentary rock lithified mud (mostly clay and some silt)	1610-2730	1.3 – 1.7
Siltstone		Clastic sedimentary rock Mostly silt and some clay	1360-2880	2.2
Gypsum	$CaSO_4.2(H_2O)$	Chemical sedimentary (evaporite)	1249	0.43
Rock salt	Halite NaCl	Chemical sedimentary (evaporite)	2100-2200	5.3-5.5
Anhydrite	Mostly Anhydrite ($CaSO_4$)	Chemical sedimentary (evaporite)	2820-2930	5.4 4.1-6.1 (T=50˚C)
Limestone	Carbonates (calcite or dolomite): >50%	Sedimentary rock (can be organic or chemical)	1890-3010	1.3 1.7-3.5 (T=50˚C)

Table 2.1.Continued. Selected properties of common rocks.

Rock Name	Mineral Composition	Type and General Description	Mass Density ρ [kg/m^3]	Thermal conductivity k [W.m^{-1}.˚C^{-1}]
Dolomite	Mostly calcium-magnesium carbonate (dolomite) $CaMg[CO_3]_2$	Chemical sedimentary rock Dolomitic limestone (limestone treated with magnesium-rich groundwater)	2750-2826	2.2 2.5-4.31 (T=50˚C)
Coal	quartz, pyrite, calcite, dolomite, siderite, and ankerite	Organic sedimentary rock (accumulated plants)	1130-2100	0.17
Gneiss	Quartz, K-Feldspar, Hornblende, Biotite, Mica	Metamorphic rock Metamorphosed granite Coarse-grained, hard, foliated Formed deep beneath mountains	1830-3150	2.4-3.1 3.4 (∥)-2.5 (⊥) 2.93 (∥)-2.08 (⊥) (T=50˚C)
Marble	Calcium carbonate: 90%	Metamorphosed (recrystallized) carbonate rock (limestone, dolomite) but denser, No foliation	2510-3140	2.6-3.1
Quartzite	Quartz: 90%	Metamorphosed sandstone	2490-2780	5.0-6.3
Schist	highly variable composition May contain chlorite, amphibole and talc	Strongly foliated metamorphic metamorphosed shale with over-growth of new minerals from clay Rich in platy or elongated minerals like mica (schistocity: mica plates lie parallel to the foliation plane).	2120-3190	2.55

Table 2.1.Continued. Selected properties of common rocks.

Rock Name	Mineral Composition	Type and General Description	Mass Density ρ [kg/m^3]	Thermal conductivity k [W.m^{-1}.˚C^{-1}]
Amphibolite	Mostly amphiboles (hornblende) and Plagioclase feldspars May also contain little: Garnet (almandine), pyroxene, biotite, titanite, magnetite, epidote, chlorite and quartz	Metamorphic rock Coarse-grained Metamorphosed mafic igneous rocks (basalt & gabbro) or clay-rich sedimentary rocks (greywacke & marl	2630-3140	2.3
Slate	Mica (chlorite, moscuvite, biotite)	Low grade foliated metamorphic rock (formed at low T and P) Metamorphosed shale, mudstone or sometimes basalt Fine-grained, hard, durable, impervious	2763	1.84 (T=50˚C)
Granulite	Mostly feldspar Some quartz and ferromagnesian minerals	High grade non-foliated metamorphic rock (formed at high T and mid P) Medium- to coarse-grained	2530-3000	2.69-2.81

Sources: Birch and Clark, 1940a; Birch et al., 1942; Shaw and Weaver, 1965; Kappelmeyer and Haenel, 1974; Kjorholt et al., 1992; Somerton, 1992; Poelchau et al., 1997; Sharma, 1997; Kukkonen and Lindberg, 1998; Scharli and Rybach, 2001; Cote and Konrad, 2005a; ASHRAE, 2009; Nabelek et al., 2010; Eppelbaum et al., 2014; www.britanica.com; www.engineeringtoolbox.com; www.rocscience.com.

Table 2.2. Selected properties of common rock-forming minerals.

Type	**Mineral**	**Density ρ [kg.m^{-3}]**	**Moh's hardness**	**Thermal conductivity k [W.m^{-1}.˚C^{-1}]**
Framework Silicates (Tectosilicates)	Quartz SiO_2	2630-2650	7	Crystalline: 7.7 Single crystal: 12.0(∥)–6.8(⊥)
	Opal $SiO_2.nH_2O$	2100	5.5-6	1.36
	K-feldspar $KAlSi_3O_8$	Orthoclase: 2560-2580	6	Orthoclase: 2.00-2.56 Microcline: 2.08-2.76
	Plagioclase (Na/Ca-feldspar)	2690	6-6.5	Albite $NaAlSi_3O_8$: 2.24 Oligoclase: 1.92 Bytownite: 1.56 Anorthite $CaAl_2Si_2O_8$: 2.6 Labradorite: 1.53
Sheet silicates (Phillosilicates)	Muscovite $KAl_2(AlSi_3O_{10})(OH)_2$	2830	2-2.5	2.21
	Chlorite $(Mg,Fe)_3(Si,Al)_4O_{10}(OH)_2.(Mg,Fe)_3(OH)_6$	2890	6.5 (Chloritoid)	4.91
	Biotite $K(Mg,Fe)_3(AlSi_3O_{10})(OH)_2$	3100	2.5-3	2.34
	Serpentine	2520	-	2.95 (Antigorite $Mg_3Si_2O_5(OH)_4$)
	Kaolinite $Al_2SiO_2O_5(OH)_4$	-	-	-

Table 2.2.Continued Selected properties of common rock-forming minerals.

Type	**Mineral**	**Density ρ [kg.m^{-3}]**	**Moh's hardness**	**Thermal conductivity k [W.m^{-1}.˚C^{-1}]**
Chain silicates (Inosilicates)	Amphiboles (Hornblende) $(Ca,Na)_{2-3}(Mg,Fe,Al)_5Si_6(Si,Al)_2O_{22}(OH)_2$	Hornblende: 3240-3450	5-6	Hornblende: 3.08
	Augite Syenite $(Ca,Na)(Mg,Fe,Al)(Si,Al)_2O_6$	3410	5-6.5	4.1 (T=35˚C, P=3.4 MPa)
	Pyroxenes	3500	4.5-6 (Pyroxferroite, Pyroxmangite)	6.66 (Jadeite $NaAlSi_2O_6$) 3.82 (Augite $XY(Z_2O_6)$)
Disilicates (Sorosilicates)	Epidote $Ca_2(Al,Fe)Al_2O(SiO_4)(Si_2O_7)(OH)$	3450	7	2.62
	Nepheline	2600	6	1.73
Orthosilicates	Sphene (Titanite) $CaTiO(SiO_4)$	Spheniscidite : 2710	1-1.5	2.33
	Olivines	3320	6.5-7	5.15 (Forsterite Mg_2SiO_4), 3.16 (Fayalite Fe_2SiO_4)
	Zircon ZrSiO4	4650	7.5	4.54
	Garnets (Pyrope $Mg_3Al_2(SiO_4)_3$)	3617	-	3.09 (Andradite), 5.64 (Grossularite)
	Sillimanite Al_2SiO_5	3240	7	9.09
Carbonates	Calcite $CaCO_3$	2660-3120	2-5	3.59
	Dolomite $CaMg(CO_3)_2$	-	-	5.51
	Magnesite $MgCO_3$	-	-	5.83

Table 2.2.Continued Selected properties of common rock-forming minerals.

Type	**Mineral**	**Density ρ [kg.m^{-3}]**	**Moh's hardness**	**Thermal conductivity k [W.m^{-1}.˚C^{-1}]**
Sulfates	Gypsum (hydrous) $CaSO_4.2H_2O$	-	-	-
	Anhydrite (anhydrous) $CaSO_4$	-	-	-
Oxides	Magnetite Fe_3O_4	5145	-	3.7 (T=80˚C)
	Hematite Fe_2O_3	5143	-	6.1 (T=80˚C)
Halides	Halite NaCl	2170-2180	2.5	5.4
	Fluorite CaF_2	3130	4	9.71
Sulfides	Pyrite FeS_2	4915	-	19.20
	Chalcopyrite $CuFeS_2$	4089	-	8.20
	Sphalerite ZnS	4050-4103	3.5-4	12.72

Sources: Birch and Clark, 1940a; Birch and Clark, 1940b; Sass, 1965; Horai and Simmons, 1969; Horai, 1971; Molgaard and Smeltzer, 1971; Cermak and Rybach, 1982; Rybach and Cermak, 1987; Diment and Pratt, 1988; Klein et al., 1999; ASHRAE, 2009, www.webmineral.com.

Table 2.3. Models for thermal conductivity of rocks with respect to other paramaters.

Equation	Parameters	Notes	References
$k_s = \prod_j k_{mj}^{x_j}$ where $\sum_j x_j = 1$	k_{mj} [$W.m^{-1}.K^{-1}$]: thermal conductivity of mineral j xj: volumetric fraction of mineral j	Geometric mean	
$k_s = 7.7^{Q} \times 2.85^{(1-Q)}$	k_{mQ}=7.7 $W.m^{-1}.K^{-1}$: thermal conductivity of mineral quartz k_{mO}=2.85 $W.m^{-1}.K^{-1}$: thermal conductivity of other minerals Q: volumetric quartz content	First approximate geometric mean	
$k_s = 2^{1-Q} \times 7.7^{Q}$ for $Q > 0.2$ $k_s = 3^{1-Q} \times 7.7^{Q}$ for $Q \leq 0.2$		Second approximate geometric mean	Johansen, 1975
$k_s = 7.7Q + 2.85(1-Q)$	Defined above	Arithmetic mean Parallel configuration of minerals Upper bound	
$k_s = \frac{1}{\frac{Q}{7.7} + \frac{1-Q}{2.85}}$	Defined above	Harmonic mean Series configuration of minerals Lower bound	
$k = \frac{\rho^4}{9.56 \times 10^{-3}}$ $\rho = 2.65 \times 10^{-3}(1-n)$ $k = 5.16 \times 10^{-9}(1-n)^4$	k [$W.m^{-1}.K^{-1}$]: thermal conductivity of rock ρ [$kg.m^{-3}$]: bulk mass density n: porosity	For sandstones	Anand, 1973

Table 2.3.Continued Models for thermal conductivity of intact rocks with respect to other paramaters.

Equation	Parameters	Notes	References
$\log(\frac{k}{1 W.m^{-1}.K^{-1}}) = \frac{475e^{-12.3n}}{F}$	F: formation electrical resistivity factor n: porosity	For sandstones	Anand, 1973
$k = 0.6\times10^{-3}\rho - 5.52n + 0.92k_h^{0.1} + 0.22F - 0.054$	k_h [m^2]: permeability		Anand, 1983
$k = -1.1864 + 0.006UCS + 0.1493\rho + 0.0134n + 0.0004V_P$	UCS [Pa]: uniaxial compression strength V_P [$km.s^{-1}$]: P-wave velocity		Gegenhuber and Schoen, 2012; Khandelwal, 2012
$k = k_\ell^n.k_s^{1-n}$		Geometric mean	
$k = nk_\ell + (1-n)k_s$		Arithmetic mean Parallel configuration of grain and water Upper bound	
$k = \frac{1}{\frac{n}{k_\ell} + \frac{1-n}{k_s}}$		Harmonic mean Series configuration of grain and water Lower bound	
$\frac{k}{k_\ell} = (\frac{k_s}{k_\ell})^{A+B\log(\frac{k_s}{k_\ell})}$	$A = 0.362 - 0.65\log(n)$ B=-0.057	For single liquid-saturated granular medium	Krupiczk, 1967

Fluids. Common pore fluids have lower thermal conductivity than minerals (Compare values in Tables 2.2 and 2.4). Therefore, rocks with lower porosity have higher thermal conductivity. Thus porosity is often selected as a control parameter (Somerton, 1992).

Heat conduction takes place through liquid-filled pores adds to other heat transfer phenomena. Furthermore, the presence of liquids reduces the thermal resistance in fractures. For example, there is a 4 – to – 8 times increase in the thermal conductivity of an uncemented sand specimen (Chapter 4) and 50% increase in the thermal conductivity of a low porosity sandstone upon saturation with water (SOMERTON, 1992). Relationships between the thermal conductivity and indicator parameters of spatial state of rocks and pore fluids are given in Table 2.4.

2.4. TEMPERATURE EFFECTS

Rocks and rock forming minerals melt at temperatures above ~1000 ˚C (Yoder, 1976; Best, 1982; Hall, 1996; Hewins et al., 1996; Del Gaudio et al., 2009), which is beyond relevant temperatures being considered in energy geo-systems.

Other phase transitions are encountered at lower temperatures. For example, serpentinization of olivine minerals in Dunite rocks takes place at T = 400 ˚C, the α-β transition point for quartz is at T = 573 ˚C, feldspar converts to sericite and kaolinite at T=330 ˚C (Birch, 1961; Eggleton and Banfield, 1985; Pilchin and Eppelbaum, 1997). Most clay minerals decompose in the 400-700 ˚C range, and calcite decomposes in the 700-830 ˚C (Tian et al., 2012). These transition temperatures are higher than temperatures relevant to most energy geo-systems being considered.

Table 2.4. Physical properties of common fluids underground at room temperature and atmospheric pressure unless specified.

Fluids	Density ρ [kg/m^3]	Thermal conductivity k [W.m^{-1}.K^{-1}]	Heat capacity C_p [kJ.kg^{-1}.˚C^{-1}]	Viscosity μ [Pa.s]
Air	1.2	0.024	1.005	1.8×10^{-4}
CO_2 gas	1.842	0.0146	0.837	7.03×10^{-5}
Methane gas	0.717	0.030	2.177	1.03×10^{-5}
SO_2 gas	2.927	0.0086	0.633	1.17×10^{-5}
Brine (T=15˚C)	1.034(C=5%) 1.148(C=15%)	0.56(C=5%) 0.48(C=15%)	3.93(C=5%) 3.41(C=15%)	1.2×10^{-3} (C=5%) 1.8×10^{-3} (C=15%)
Water	998	0.56 – 0.60	4.186	0.001
Light crude oil	< 870	0.12-0.15		0.006
Heavy oil	920 - 1000	0.14		0.01 – 0.1
Bitumen	> 1000	0.17		$10 – 10^4$
Methane hydrate	929 (T= -10 ˚C)	0.575		-
Ice	921	2.2 (T=0˚C)	2.038	2×10^{13}
Molten NaCl	1490	0.3	1.44	

Sources: OZBEK AND PHILLIPS, 1979; SOMERTON, 1992; HUANG AND FAN, 2005; ASHRAE, 2009; www.engineeringtoolbox.com; www.wikipedia.com (brine); www.webserver.dmt.upm.es; www.pipeflowcalculations.com; www.apithailand.com/carbon; www.see.ed.ac.uk.

There are still changes in properties at lower temperatures than thermal decomposition point. For example, the thermal expansion starts as soon as the temperature gradient is imposed, and it increases with increasing T (Appendix A, Figure A-3) depending on micro- and macro-structure of geomaterials, the thermal expansion of the discrete constituents may create micro-cracks or close the pre-existing discontinuities. Consequently, two geomaterials with similar mineralogy can show two opposite responses to temperature rise.

Moreover, different thermal expansion of different mineral grains (in poly-mineralic rocks), crystals with different orientations (in poly- and mono-mineralic rocks), and that of grains and pore fluid(s) can result variety of mechanical, hydraulic and thermal responses of the whole medium subjected to coupled processes. These may exert tremendous amount of stress on boundaries or cause tremendous amount of deformations depending on the governing initial and boundary conditions. Any change that alters the state of effective stress and contact resistance between discrete constituents will influence the thermal conductivity of the medium significantly. A micro-scale investigation of responsible phenomena in various rock-forming minerals and in rocks as a composite of these materials follows.

2.4.1. Thermal Conductivity of Crystalline Materials vs. Temperature

In non-metallic crystalline solids, energy carrying phonons are scattered not only by interaction with each other but also by presence of impurities and other irregularities in crystal structure or large-scale lattice interruptions such as grain boundaries. Mean free path and consequently thermal conductivity of the crystal decreases by scattering by any of these sources of phonon scattering (Makinson, 1938). Each of phonon scattering

phenomena becomes relevant at different temperatures for various materials. Experimental studies show that for crystals, mean free path sharply decreases due to phonon scattering as the temperature and amplitude of lattice vibrations increase (Tritt, 2004).

However, the elastic wave velocity and heat capacity do not change much; thus, based on Equation 2.5 the thermal conductivity decreases with increasing temperature for $T > T_D$ (Debye temperature, beyond which the heat capacity remains almost constant). When the temperature decreases, the mean free path increases until the heat carrying lattice waves get scattered by the boundaries while the elastic wave velocity remains almost constant and the heat capacity decreases. The resultant trend is decreasing thermal conductivity with decreasing temperature. The peak for thermal conductivity of a crystalline solid usually occurs at temperature about $T_D/10$. T_D for silicate minerals is ranged between 210 ˚C for muscovite and 910 ˚C for quartz (Robie, 1988). Even small amounts of impurities in a crystal lowers the mean free path of phonons by adding additional scattering spots while they do not influence the mass density, heat capacity and elastic wave velocity of the material significantly. Therefore, impurities affect the thermal conductivity of a material at low temperatures more, at which the mean free path would be limited by boundaries otherwise (Tritt, 2004). The thermal resistivity (inverse of the thermal conductivity) of crystalline materials increases linearly with temperature (Birch and Clark, 1940a). This relationship is stronger up to 300 ˚C for rocks (Blesch et al., 1983). Figure 2.2 shows the variation of thermal conductivity of quartz, calcite and halite versus temperature.

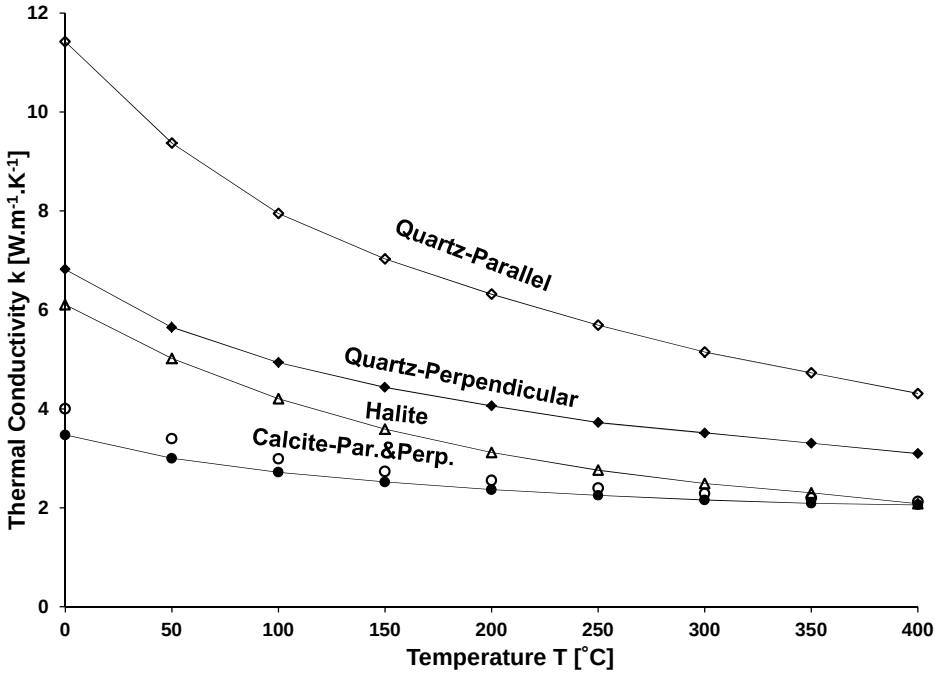

Figure 2.2. Thermal conductivity of quartz, calcite and halite minerals versus temperature (Birch and Clark, 1940a).

2.4.2. Thermal Conductivity of Amorphous Materials vs. Temperature

For amorphous materials with lower thermal conductivity than their equivalent crystalline analogies, the thermal conductivity increases with increasing temperature. For example, the thermal conductivity of a single crystal of quartz is about 10 $W.m^{-1}.K^{-1}$ in average at room temperature, but that of amorphous SiO_2 (opal) is about 1 $W.m^{-1}.K^{-1}$ (Eucken, 1911). The mean free path of phonons and mass density hardly change in glasses (the same order of magnitude of the scale of disorder or the average random inter-atomic distance in the structure of glass material, ~7 Å) with temperature and the elastic wave velocity remains constant; therefore, the thermal conductivity follows the variation of heat capacity with changing temperature in amorphous materials (Kittel, 1949). The universal temperature-dependency of amorphous materials shows increase in heat

capacity and thermal conductivity for temperatures above -253 ˚C (20 K) (Cahill and Pohl, 1988).

2.4.3. Thermal Conductivity of Rocks vs. Temperature

The thermal conductivity of crystalline minerals and hard rocks with high initial thermal conductivity (room temperature and atmospheric pressure) decreases with temperature (Ratcliffe, 1959; Powell et al., 1966; Horai and Susaki, 1989; Abdulagatov et al., 2006). In average, the thermal conductivity of these materials decreases to 40-50% of its original value when the temperature increases from 20 to 1000 ˚C (Clauser, 2009; Miao et al., 2014). Data show that the higher is the initial thermal conductivity, the higher is its decrease with temperature rise. Felsic rocks (contain feldspars and quartz), such as granite, have a high thermal conductivity (k_o=4 $W.m^{-1}.K^{-1}$), and its decrease with increasing temperature is greater than mafic rocks (contain magnesium and iron) such as anorthosite, basalt, diabase and gabbro, which have lower initial thermal conductivity (k_o=1.8-2 $W.m^{-1}.K^{-1}$). The thermal conductivity of Quartzite (k_o=5.6 $W.m^{-1}.K^{-1}$) may decrease as much as 200% with 500 ˚C increase in temperature (Clauser, 2009). Overall, the following percentages have been reported for decline in thermal conductivity of various types of rocks: 37% for igneous rocks, 46% for metamorphic rocks and 42% for sedimentary rocks with 300 degrees increase in temperature (Vosteen and Schellschmidt, 2003). However, the thermal conductivity of rocks containing a mixture of crystalline and amorphous minerals (mineraloids) increases slightly with increasing temperature (Birch and Clark, 1940b). A rule of thumb has been suggested that in general, the thermal conductivity of materials with k>2 $W.m^{-1}.K^{-1}$ at room temperature decreases with increasing temperature and thermal conductivity of materials with k<2 $W.m^{-1}.K^{-1}$ at room

temperature increases with increasing temperature (Anand, 1973; Lee and Deming, 1998).

2.4.4. Compiled Data and Proposed Models

Variation of the thermal conductivity of various rocks versus temperature is shown in Figure 2.2. Table 2.5 presents the models proposed in the literature to predict the thermal conductivity of rocks with respect to temperature.

Data show that the rise in the thermal conductivity with temperature occurs only for few rocks including anorthosite ($k_{50^\circ C}$=1.7-1.9 $W.m^{-1}.K^{-1}$), shale ($k_{20^\circ C}$=1.3-1.7 $W.m^{-1}.K^{-1}$), gabbro ($k_{20^\circ C}$=2.1-2.6 $W.m^{-1}.K^{-1}$), and diabase ($k_{50^\circ C}$=2.1-2.5 $W.m^{-1}.K^{-1}$) with 34% increase in 450 degrees temperature rise (50-500 ˚C) for shale as the highest change and 1.3% increase in 400 degrease temperature rise (0-400 ˚C) for gabbro as the lowest change (2.1% for diabase and 6.2% for anorthosite). Note that this group is not limited to soft, clastic sedimentary rocks, it contains rocks that have a low quartz content, and all have thermal conductivities around 2 $W.m^{-1}.K^{-1}$ (not necessarily lower than 2) at room temperature.

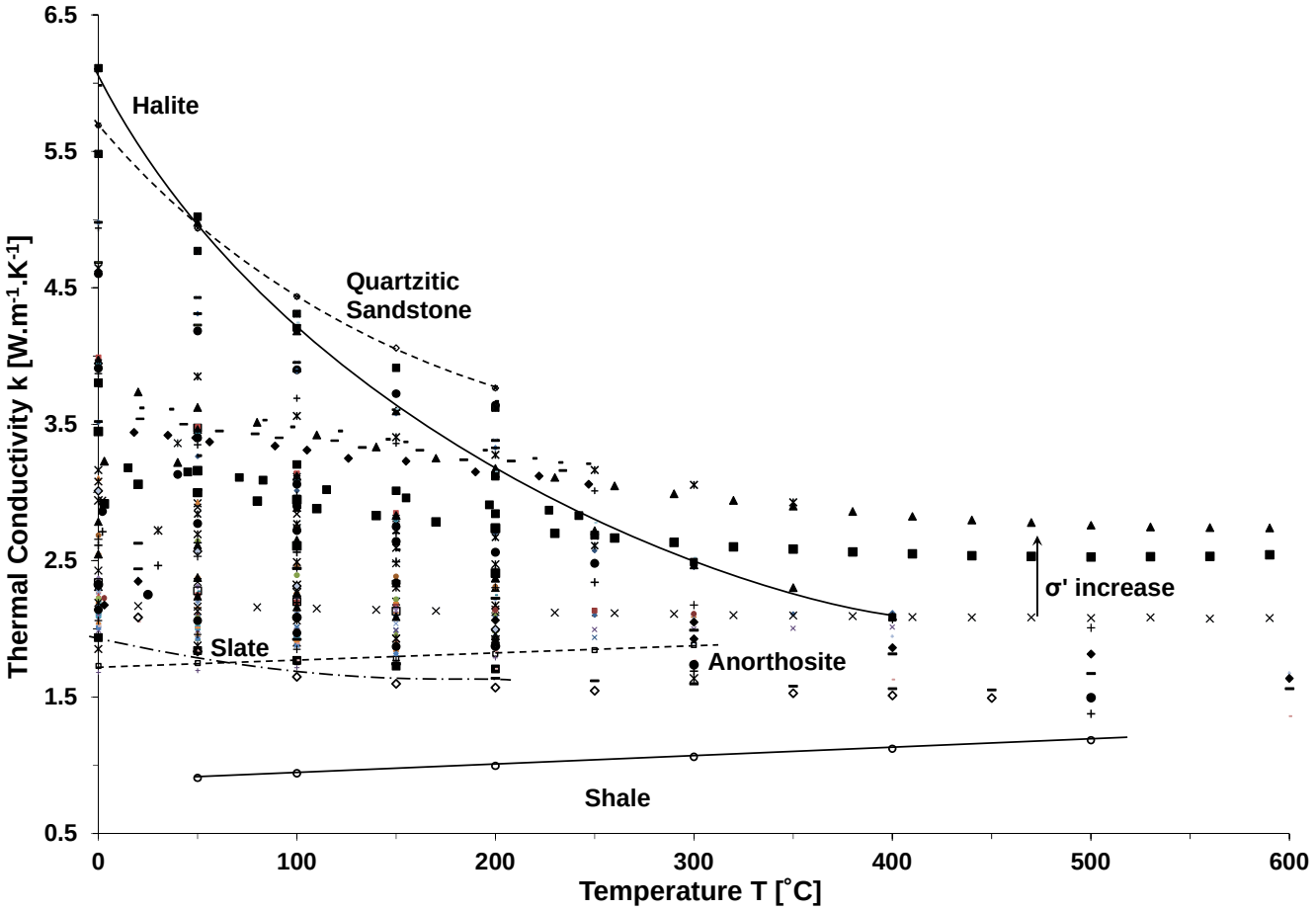

Figure 2.3. Thermal conductivity of various intact rocks versus temperature (Birch and Clark, 1940a; Durham and Abey, 1981b; Seipold, 1998; Vosteen and Schellschmidt, 2003; Abdulagatov et al., 2006; Mottaghy et al., 2008; Abdulagatova et al., 2009; Abdulagatova et al., 2010; Alishaev et al., 2012; Miao et al., 2014).

Table 2.5. Models for thermal conductivity of intact rocks with respect to temperature.

Equation	Parameters	Notes	References
$k(T) = k_o + AT$	T [˚C]: temperature k_o [$W.m^{-1}.K^{-1}$]: thermal conductivity at room temperature	For porous and soft rocks	Kukkonen et al., 1999; Abdulagatov et al., 2006; Clauser and Huenges, 2013
$k(T) = (c + dT)^{-1}$	c [$m.K.W^{-1}$]: thermal resistance at T = 0 K d [$m.W^{-1}$]: rate of increase in thermal resistance with increasing temperature T [K]	Most types of rocks	Birch and Clark, 1940a; Blesch et al., 1983; Seipold, 1995; Miao et al., 2014
$k(T) = k_o(1 + 0.001T)^{-1}$	k_o [$W.m^{-1}.K^{-1}$]: thermal conductivity at 0 ˚C T [˚C]	Most types of rocks	Cermak and Rybach, 1982
$k(T) = A + B(350 + T)^{-1}$	A [$W.m^{-1}.K^{-1}$] and B [$W.m^{-1}$]: fitting parameters	Most types of rocks	Haenel et al., 1988
$k(T) = k_{20}[1 + 0.0005(T - 20)]^{-1}$	k_{20} [$W.m^{-1}.K^{-1}$]: thermal conductivity at 20 ˚C T [˚C]	Most types of rocks	Funnell et al., 1996
$k_o = k_{25}[1.007 + 25(0.0037 - \frac{0.0074}{k_{25}})]$ $k(T) = k_o[1.007 + T(0.0036 - \frac{0.0072}{k_o})]^{-1}$	k_o [$W.m^{-1}.K^{-1}$]: thermal conductivity at 0 ˚C k_{25} [$W.m^{-1}.K^{-1}$]: thermal conductivity at 25 ˚C T [˚C]	For rocks with k > 2 $W.m^{-1}.K^{-1}$ and temperatures up to 300 ˚C For k_o<2 $W.m^{-1}.K^{-1}$, shows increase in k with T, and for k_o=2 $W.m^{-1}.K^{-1}$, remains constant $k(T)=k_o$.	Sass et al., 1992

Table 2.5.Continued Models for thermal conductivity of intact rocks with respect to temperature.

Equation	Parameters	Notes	References
$k(T) = k_{20} - (k_{20} - 3.3)[e^{0.725\frac{T-20}{T+130}} - 1]$	$k \times 10^{-3}$ [$cal.s^{-1}.cm^{-1}.C^{-1}$] T [˚C]	Most of rocks for temperatures up to 300 ˚C	Kutas, 1977
$k(T) = k_{20} - k_{20}^{0.64}(T - 293)(k_{20} - 1.38) \times [k_{20}(1.8\times10^{-3}T)^{-0.25k_{20}} + 1.28]\times10^{-3}$	k_{20} [$W.m^{-1}.K^{-1}$]: thermal conductivity at 20 ˚C T [K]	For rocks with $k_{20} < 2.5$ $W.m^{-1}.K^{-1}$	Somerton, 1992
$k(T) = k_{20}\frac{293}{T+273}$	k_{20} [$W.m^{-1}.K^{-1}$]: thermal conductivity at 20 ˚C T [˚C]	Most types of rocks	Chapman et al., 1984
$k(T) = 1.8418 + \frac{1473T_r}{1473\ \ T_r} \times (k_r - 1.8418)(\frac{1}{T} - \frac{1}{1473})$	k_r [$W.m^{-1}.K^{-1}$]: thermal conductivity at room temperature T_r [K]: room temperature T [K]	Most types of rocks	Sekiguchi, 1984
$k(T) = \frac{T}{F(T-314)+122}$	F [$m.K.W^{-1}$]: fitting parameter	Most of rocks for temperatures up to 300 ˚C	Seipold, 1998
$k(T) = \frac{474}{T+77} + 1.18$	T [˚C]	For basic rocks	Haenel et al., 1988
$k(T) = \frac{807}{T+77} + 0.64$	T [˚C]	For acidic rocks	Haenel et al., 1988
$k(T) = \frac{705}{T+77} + 0.75$	T [˚C]	For metamorphic rocks	Haenel et al., 1988
$k(T) = \frac{k_o}{0.99 + T\frac{a-b}{k_o}}$	a and b: fitting parameters k_o [$W.m^{-1}.K^{-1}$]: thermal conductivity at room temperature T [˚C]	For metamorphic rocks	Vosteen and Schellschmidt, 2003

Data show that the thermal conductivity of gabbro, diabase, and anorthosite may also decrease slightly with temperature that may be associated to different initial spatial state or the uncertainty of experimental apparatus. However, the amount of increase in thermal conductivity of shale is large, and the responsible phenomenon for this increase is its layered structure. Minerals expand upon heating and they fill the gaps between layers. This increases the number and area of contact between mineral grains and provides larger heat pathways. The trend for shale is linear with the following relationship:

$$k(T) = 0.88 + 0.0006T \qquad \text{For shale} \qquad (2.6)$$

Figure 2.4.a shows the physical process taking place in an idealized model of layered philosilicate minerals in shale. Compiled data in this study show that the thermal conductivity decreases 1% for Diabase (Westfield) and 66% for halite (rock salt) with 400 degrees increase in temperature (0-400 ˚C) as the highest and lowest changes. Decreasing trends include rocks from all types with thermal conductivities k_o>2 $W.m^{-1}.K^{-1}$. However, there are several recognizable categories.

The thermal conductivity of the first group decreases less than 25 percent with a 500 degree temperature rise. Rocks in this group have a low quartz content, initial thermal conductivities around 2 $W.m^{-1}.K^{-1}$, and some have a weathered macro structure such as: gabbro, diabase, albitite, syenite, soft limestone, soft sandstone, soft pyroxenite (with low k_o), gneiss, weathered granulite and weathered slate (with low k_o). Some of these rocks may even show increase in their thermal conductivities as mentioned above (diabase and gabbro) depending on the fabric they have developed in different environments so that they are on the transitional boundary. The following linear

relationship is proposed to predict the thermal conductivity of these rocks with temperature T [˚C]:

$$k(T) = k_o - 0.0013T \qquad \text{For } 1.9 \text{ W.m}^{-1}.\text{K}^{-1} < k_o < 2.5 \text{ W.m}^{-1}.\text{K}^{-1}, \text{ and } Q<0.2 \qquad (2.7)$$

Equation 2.7 is restricted by two criteria, and both of them have to be satisfied. These criteria highlight two important factors: suppressed overwhelming effect of quartz content and sufficiently soft (open, discontinuous, discrete) structure that the thermal expansion of components and generation of inter-particle/crystal cracks does not decrease the thermal conductivity significantly. For example Equation (2.7) cannot predict the thermal conductivity of hard pyroxenite that mostly contains pyroxene (>95%) and dunite that mostly contains Olivine (>90%), although they do contain less than 20% quartz, because they can have initial thermal conductivity k_o = 3.7-4.7 W.m^{-1}.K^{-1} that means they have a tight structure (Birch and Clark, 1940a; Seipold, 1998). Other potential candidates to fit in this group are basalt, serpentinite, siltstone, gypsum, coal, and schist with $Q<0.1$ and $k_o<2$ W.m^{-1}.K^{-1}, but there are no data available at this time for their thermal conductivity versus temperature.

Chemical and physical alteration of rock mineral composition and macro-structure differentiates rocks from the same origin from being in the same group. For example, dolomite is a limestone being treated in a magnesium-rich environment. This process improves the heat transfer characteristics of limestone so that the initial thermal conductivity of dolomite is higher than that of limestone and its temperature dependency does not follow the same trend. Marble is a limestone or dolomite treated at high temperature and high pressure for long time in the nature (metamorphosed). The process of recrystallization of limestone/dolomite, originally with 50% calcite, excludes all the

impurities and Marble with over 95% calcite is formed. Hence, its initial and temperature-dependency of thermal conductivity is totally different than those two rocks that it originated from so that it behaves similar to felsic rocks. The other example is anhydrite that is dehydrated gypsum. Initial thermal conductivity of anhydrite is close to that of felsic rocks. Data is not available to examine its temperature-dependent response, but it is postulated to decrease more than gypsum under the same temperature rise.

The thermal conductivity of the third group decreases nonlinearly about 60% with a 400 ˚C temperature rise. Rock salt is in this group. Its initial thermal conductivity at room temperature is ~7 $W.m^{-1}.K^{-1}$. The very regular and hard crystalline structure of sodium chloride and the high purity of this rock lead it to follow the behavior of its single mineral. Figure 2.2 shows the thermal conductivity of quartz, halite and calcite versus temperature. The thermal resistivity of rock salt increases linearly with temperature as follows:

$$k(T) = (0.0008T + k_o)^{-1} \quad \text{For rock salt} \tag{2.8}$$

The thermal conductivity of the middle group decreases between 25-40%. This group contains rocks from all types, and they all have thermal conductivities higher than 2 $W.m^{-1}.K^{-1}$ and lower than 5.5 $W.m^{-1}.K^{-1}$. Based on the compiled data in this study, this group includes: granites, granodiorite, quartz monzonite, quartzitic hard sandstone, hard limestone, hard dolomite, marble and quartzite. In order to identify the responsible processes that cause decrease in thermal conductivity of these rocks, we can subcategorize them into (1) polymineralic felsic rocks such as granite, granodiorite, quartz monzonite that were formed by crystallization from a melt; (2) almost mono-mineralic mostly containing quartz or carbonate minerals such as quartzitic sandstone,

limestone and dolomite that were formed by sedimentation or chemical reactions in wet environment and subjected to high overburden stresses to consolidate extensively or such as marble and quartzite that have experienced extreme chemical, mechanical and thermal treatments to convert to very hard and impervious rocks.

Physical models to explain the processes involved in heat transfer upon temperature rise in these rocks are shown in Figure 2.5. The differential thermal expansion of different minerals in poly-mineralic rocks and randomly oriented crystals in mono-mineralic rocks opens micro-cracks between the mineral grains and crystals that adds a significant thermal resistance to the medium. The coefficient of volumetric thermal expansion of some rock-forming minerals are listed in Table A-2. Note that the thermal expansion of quartz is the highest among other common minerals ($\beta=31\times10^{-6}$ $^{\circ}C^{-1}$ at T=60 $^{\circ}C$) and it increases with temperature (Figure A-3). This explains why the amount of decrease in thermal conductivity of rocks with high quartz content is higher than that for basic and ultrabasic rocks. The relationship proposed by Sekiguchi et al. (1984) fits the data well by only providing the room temperature T_r [K] and thermal conductivity measured at that temperature k_r [$W.m^{-1}.K^{-1}$]:

$$k(T) = 1.8418 + \frac{1473T_r}{1473 - T_r} \times (k_r - 1.8418)\left(\frac{1}{T} - \frac{1}{1473}\right) \qquad (2.9)$$

T is in [K]. The measured versus predicted data are shown in Figure 2.5.

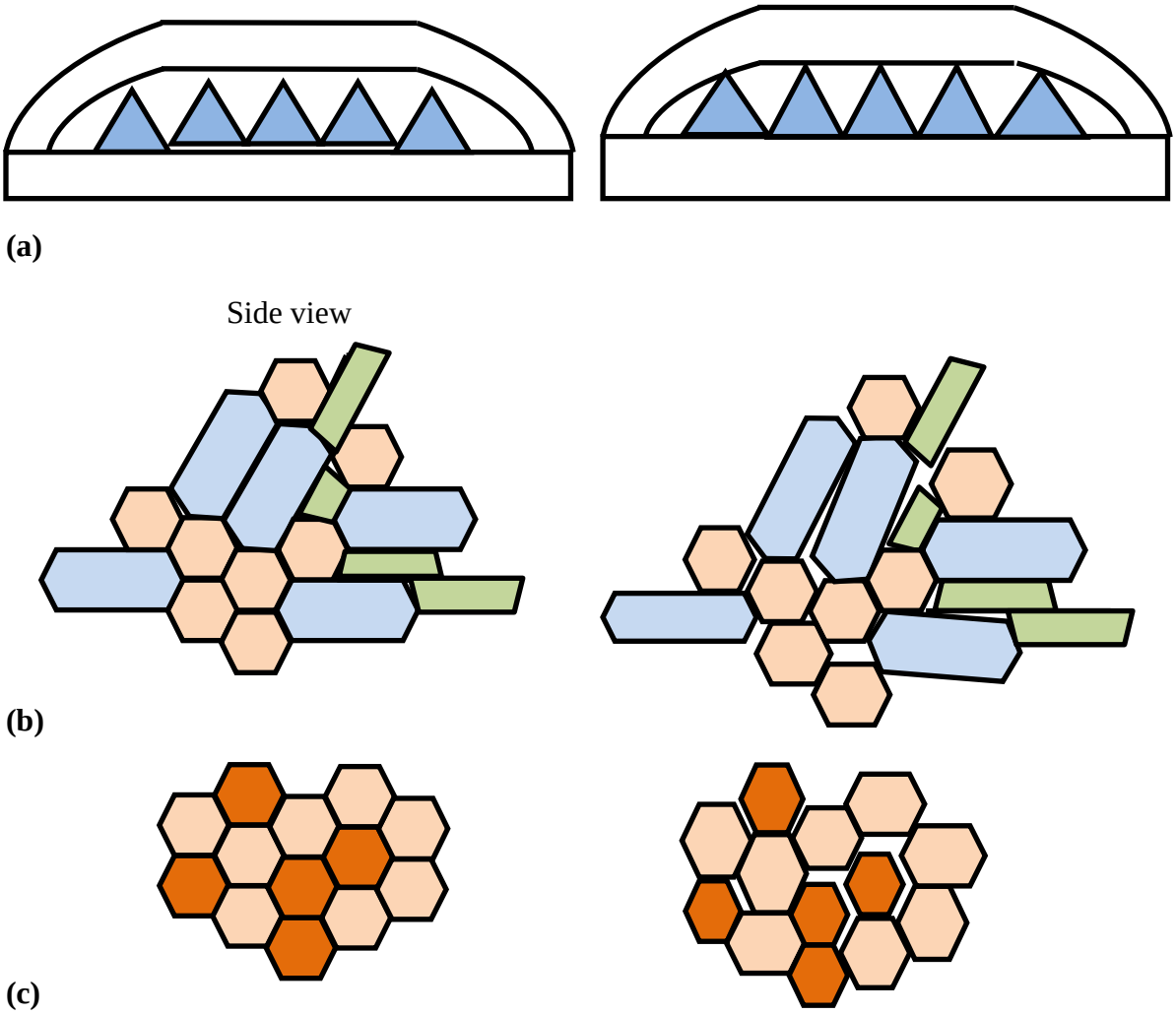

Figure 2.4. Physical model for initial (at room temperature-left) and final (at elevated temperature- right) configurations of (a) Shale with layered structure (both micro and macro). Philosilicate minerals are platy and they arrange in a preferred orientation that causes a layered structure for the whole medium. There are micro and macro crack between minerals and layers. Mineral grains expand upon heating and fill the gaps between layers so that thermal conductivity increases with temperature. (b) Poly-mineralic rocks consist of various minerals with different physical properties. The differential thermal expansion of mineral grains generates inter-particle/crystal cracks that add thermal resistance to the medium and thermal conductivity decreases with temperature. (c) Mono-mineralic rocks consist of randomly oriented crystals. The differential thermal expansion of crystals along different axes causes micro-cracks between them and the thermal conductivity decreases upon heating.

The thermal conductivity change versus temperature was discussed for dry intact rocks. The thermal conductivity of fluids also changes with temperature. Figure 2.6 shows the variation of thermal conductivity of water, air and steam with temperature. The thermal conductivity of a water (or brine)-saturated rock can be significantly higher than that of the same rock at dry condition. This enhancement may cause a transition in the response of a soft rock. For example an anorthosite rock that shows slight increase in thermal conductivity with temperature when it is dry; it may show decrease if it is subjected to the temperature rise in water-saturated condition.

2.5. STRESS EFFECTS

Thermal conductivity of geomaterials with contractive behavior increases with increasing effective stress because of closure of discontinuities and improvement of grain contacts. Variation of thermal conductivity of rocks with increasing effective stress depends on their initial porosity, micro-cracks and fractures, the state of stress, and the elastic properties of rock skeleton. Thermal conductivity of porous and soft rocks is more effective stress-sensitive than that of crystalline and hard rocks.

Intact rocks, particularly sedimentary rocks, can be treated as cemented soils. Cementation decreases the stress-sensitivity of granular materials properties (Fernandez and Santamarina, 2001). Most of the change in the thermal conductivity of rocks upon increase in effective stress occurs at low to medium effective stress levels (Abdulagatov et al., 2006; Clauser and Huenges, 2013). The thermal conductivity increases relatively significantly compared to its initial value when the stress reaches to the level sufficient to break the bond between grains (called break-down stress), which can be different for various rock types. Beyond some effective stress level (called cross-over stress), the

porosity or density does not change with further increase in effective stress. Therefore, at high effective stress levels, the thermal conductivity shows no or very little change with effective stress (Abdulagatov et al., 2006).

2.5.1. Compiled Data and Proposed Models

A linear relationship is observed between the thermal conductivity and effective stress using its value at atmospheric pressure and room temperature k_{po} [$W.m^{-1}.K^{-1}$] (Hurtig, 1970; Kappelmeyer and Haenel, 1974):

$$k(\sigma') = k_{po}(1 + \delta\sigma') \tag{2.9}$$

δ [Pa^{-1}] has been extracted from experimental data for different rock types, and its small values (in the order of 10^{-5}) show that the thermal conductivity of rocks (particularly, intact rocks with low porosities) is not stress-dependent.

Correlation developed based on the compiled data in this study for sedimentary rocks (sandstone and limestone) is a hyperbolic model to capture the increasing trend that gets to an asymptotic value at higher stresses, and it is shifted by the value of thermal conductivity at atmospheric pressure k_{po} [$W.m^{-1}.K^{-1}$] as follows:

$$k(\sigma') = k_{po} + \sigma'(a + b\sigma')^{-1} \tag{2.10}$$

In Equation 2.10: a^{-1} [$W.m^{-1}.K^{-1}.MPa^{-1}$] shows the maximum gradient (maximum slope) of increase in k with increasing effective stress $(\partial k/\partial \sigma')_{max}$. b^{-1} [$W.m^{-1}.K^{-1}$] shows the asymptotic value that k reaches k_{ult} under a characteristic stress. The ratio of these two parameters (a/b [MPa]) is the characteristic effective stress σ'_{chr}, at which the thermal conductivity reaches to its ultimate or asymptotic value k_{ult}.

The highest stress-sensitivity is shown by some sedimentary rocks such as limestone. For limstones tested under increasing stress from 0.1 to 250 MPa and at

various temperatures (0, 50, 100, and 150 ˚C – kept constant for each series under variable stress) Abdulagatov et al., 2006 b^{-1} is constant for all temperatures k_{ult}=0.34 [$W.m^{-1}.K^{-1}$]. However, a^{-1} increases with increasing temperature, that shows the gradient of thermal conductivity increases with temperature with the following relationship:

$$(\frac{\partial k}{\partial \sigma'})_{max} = 8\times10^{-7}T^2 + 4\times10^{-5}T + 0.0086 \quad (2.11)$$

The initial thermal conductivity k_{po} [$W.m^{-1}.K^{-1}$] measured under 0.1 MPa at various temperatures (0, 50, 100, and 150 ˚C) in the above-mentioned study, decreases from 1.94 to 1.55 [$W.m^{-1}.K^{-1}$] with the following relationship:

$$k_{po}(T) = 1.9 - 0.003T \quad (2.12)$$

Data is shown in Figure 2.7. Stress- and temperature-dependency of thermal conductivity of limestone can be obtained by combining Equations 2.10, 2.11, and 2.12, taking into account the constant value of b=2.94 $m.K.W^{-1}$. Trends for sandstone tested under the same conditions (Abdulagatov et al., 2006; Abdulagatova et al., 2009) are similar to those of limestone.

For geomaterials with dilative behavior, the failure under high stress is followed by an extensive dilation that decreases thermal conductivity

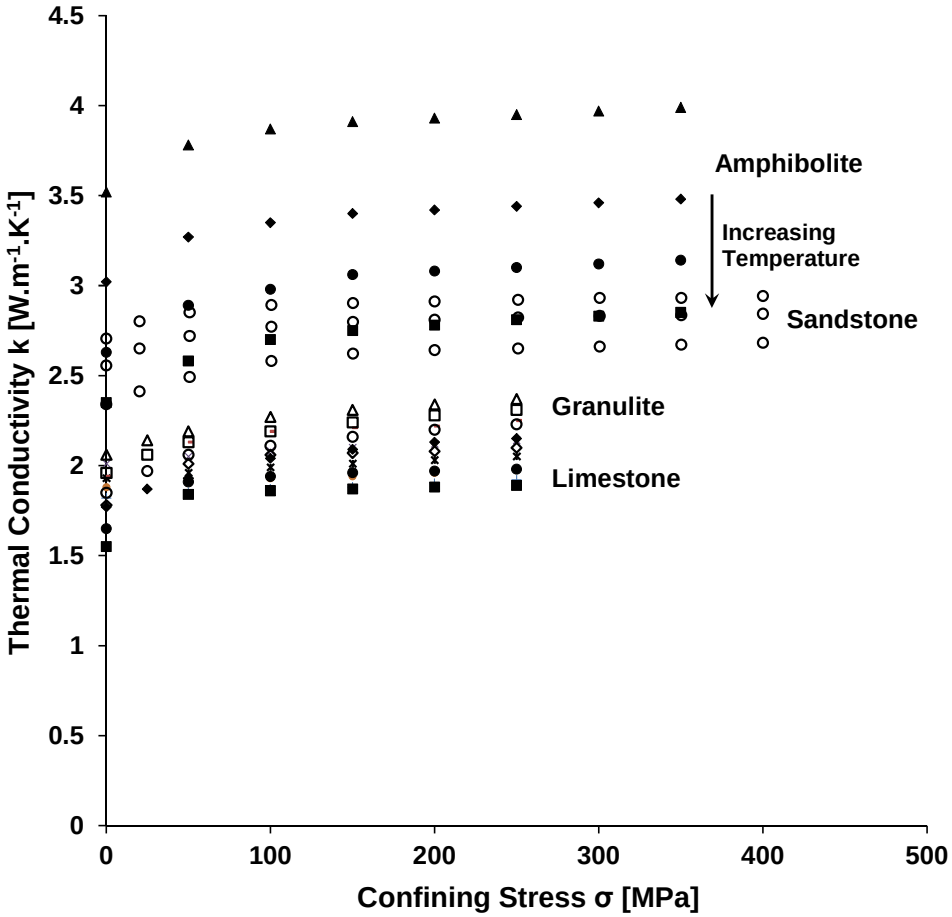

Figure 2.5. Thermal conductivity versus stress for two sedimentary and two metamorphic rocks – Data from: Abdulgatov et al. 2006; Abdulgatova et al. 2009.

2.6. CONCLUSIONS

Salient conclusions follow:

- The thermal conductivity of tight and hard crystalline rocks decreases with temperature, because the differential thermal expansion of tightly and randomly arranged mineral grains (relevant to poly-mineralic rocks) and randomly oriented crystals (relevant to poly- and mono-mineralic rocks) creates cracks between them that adds a significant thermal resistance.

- The higher is the quartz content of a rock, the higher is its thermal conductivity and the higher is its thermal conductivity decline with temperature.
- The thermal conductivity of crystals is directly proportional to the mean free path of phonons that decreases with increasing temperature.
- The thermal conductivity of amorphous minerals increases with temperature because their heat capacity increases.
- The thermal conductivity of rocks with fractured or open structure such as shale increases with temperature. The thermally expanded mineral grains fill the inter-particle and inter-layer gaps.
- Despite a very low porosity of rocks, their thermal conductivity is still stress-sensitive. It increases slightly with confining effective stress because the stress closes the micro-fractures and collapses the weak pores. The trend is hyperbolic so that an asymptotic value is reached at a characteristic stress level.

2.7. REFERENCES

Abdulagatov, I. M., Emirov, S. N., Abdulagatova, Z. Z., and Askerov, S. Y. (2006). "Effect of Pressure and Temperature on the Thermal Conductivity of Rocks." Journal of Chemical and Engineering Data, 51(1), 22-33.

Abdulagatova, Z., Abdulagatov, I. M., and Emirov, V. N. (2009). "Effect of Temperature and Pressure on the Thermal Conductivity of Sandstone." International Journal of Rock Mechanics and Mining Sciences, 46(6), 1055-1071.

Abdulagatova, Z. Z., Abdulagatov, I. M., and Emirov, S. N. (2010). "Effect of Pressure, Temperature, and Oil-Saturation on the Thermal Conductivity of Sandstone up to

250 MPa and 520 K." Journal of Petroleum Science and Engineering, 73(1-2), 141-155.

Alishaev, M. G., Abdulagatov, I. M., and Abdulagatova, Z. Z. (2012). "Effective Thermal Conductivity of Fluid-Saturated Rocks Experiment and Modeling." Engineering Geology, 135, 24-39.

Anand, J. (1973). "Predicting Thermal Conductivities of Formations from other Known Properties." Society of Petroleum Engineers Journal, 13, 267-273.

Anand, J. (1983). Thermal Conductivity of Fluid Saturated Rocks at Elevated Pressures and Temperatures, University of California, Berkeley, General Library.

ASHRAE (2009). ASHRAE Handbook - Fundamentals (I-P Edition), American Society of Heating, Refrigerating and Air-Conditioning Engineers, Inc.

Best, M. G. (1982). Igneous and Metamorphic Petrology, San Francisco : Freeman, c1982.

Birch, F. (1961). "Velocity of Compressional Waves in Rocks to 10 Kilobars, Part 2." Journal of Geophysical Research, 66(7), 2199-&.

Birch, F., and Clark, H. (1940a). "The Thermal Conductivity of Rocks and Its Dependence upon Temperature and Composition-Part 1." American Journal of Science, 238(9), 613-635.

Birch, F., and Clark, H. (1940b). "The Thermal Conductivity of Rocks and Its Dependence upon Temperature and Composition-Part 2." American Journal of Science, 238(8), 529-558.

Birch, F., Schairer, J. F., and Spicer, H. C. e. (1942). "Handbook of Physical Constants." Special Papers (Geological Society of America).(36), 1-325.

Blesch, C. J., Kulacki, F. A., and Christensen, R. N. (1983). "Application of Integral Methods to Prediction of Heat Transfer from a Nuclear Waste Repository." Open file report ONWI-495, Battelle Memorial Institution, Columbus, OH, 12-17.

Cahill, D. G., and Pohl, R. O. (1988). "Lattice-Vibrations and Heat-Transport in Crystals and Glasses." Annual Review of Physical Chemistry, 39, 93-121.

Cermak, V., and Rybach, L. (1982). "Thermal Conductivity and Specific Heat of Minerals and Rocks." Physical Properties of Rocks, Springer, Berlin, Heidelberg, 213-256.

Chapman, D. S., Keho, T. H., Bauer, M. S., and Picard, M. D. (1984). "Heat-Flow in the Uinta Basin Determined from Bottom Hole Temperature (BHT) Data." Geophysics, 49(4), 453-466.

Cho, W. J., Kwon, S., and Choi, J. W. (2009). "The Thermal Conductivity for Granite with Various Water Contents." Engineering Geology, 107(3/4), 167-171.

Clauser, C. (2009). "Heat Transport Processes in the Earth's Crust." Surveys in Geophysics, 30(3), 163-191.

Clauser, C., and Huenges, E. (2013). "Thermal Conductivity of Rocks and Minerals." Rock Physics & Phase Relations, American Geophysical Union, 105-126.

Cote, J., and Konrad, J. M. (2005a). "Thermal Conductivity of Base-Course Materials." Canadian Geotechnical Journal, 42(1), 61-78.

Del Gaudio, P., Di Toro, G., Han, R., Hirose, T., Nielsen, S., Shimamoto, T., and Cavallo, A. (2009). "Frictional Melting of Peridotite and Seismic Slip." Journal of Geophysical Research - Part B - Solid Earth, 114(B6), (19 pp.).

Diment, W. H., and Pratt, H. R. (1988). Thermal Conductivity of Some Rock-Forming Minerals: A Tabulation, Denver, CO : U.S. Geological Survey ; [Denver, Colo. : Books and Open-File Reports Section, distributor], 1988.

Durham, W. B., and Abey, A. E. (1981b). "Thermal Conductivity and Diffusivity of Climax Stock Quartz Monazite at High Pressure and Temperature." Lawrence Livermore National Laboratory Report.

Eggleton, R. A., and Banfield, J. F. (1985). "The Alteration of Granitic Biotite to Chlorite." American Mineralogist, 70, 902-910.

Eppelbaum, L., Kutasov, I., and Pilchin, A. (2014). "Applied Geothermics." <https://symbiose.uqo.ca/apps/LoginSigparb/LoginPourRessources.aspx?url=http://dx.doi.org/10.1007/978-3-642-34023-9>.

Eucken, A. (1911). "Dependence of the Thermal Conductivity of Certain Gases on the Temperature." Physical Zeitsch, 12, 1101-1107.

Fernandez, A. L., and Santamarina, J. C. (2001). "Effect of Cementation on the Small-Strain Parameters of Sands." Canadian Geotechnical Journal, 38(1), 191-199.

Funnell, R., Chapman, D., Allis, R., and Armstrong, P. (1996). "Thermal state of the Taranaki Basin, New Zealand." Journal of Geophysical Research-Solid Earth, 101(B11), 25197-25215.

Gegenhuber, N., and Schoen, J. (2012). "New Approaches for the Relationship between Compressional Wave Velocity and Thermal Conductivity." Journal of Applied Geophysics, 76, 50-55.

Haenel, R., Rybach, L., and Stegena, L. (1988). Handbook of Terrestrial Heat-Flow Density Determination with Guidelines and Recommendations of the

International Heat Flow Commission, Kluwer Academic Publishers, Place of Publication: Dordrecht, Netherlands. Country of Publication: Netherlands.

Hall, A. (1996). Igneous Petrology, Harlow : Longman, 1996.

2nd ed.

Hewins, R. H., Jones, R. H., and Scott, E. R. D. (1996). Chondrules and the Protoplanetary Disk, Cambridge University Press.

Horai, K. (1971). "Thermal Conductivity of Rock-Forming Minerals." Journal of Geophysical Research, 76(5), 1278-1308.

Horai, K., and Susaki, J. (1989). "The Effect of Pressure on the Thermal-Conductivity of Silicate Rocks up to 12 Kbar." Physics of the Earth and Planetary Interiors, 55(3-4), 292-305.

Horai, K.-i., and Simmons, G. (1969). "Thermal Conductivity of Rock-Forming Minerals." Earth and Planetary Science Letters, 6, 359-368.

Huang, D. Z., and Fan, S. S. (2005). "Measuring and Modeling Thermal Conductivity of Gas Hydrate-Bearing Sand." Journal of Geophysical Research-Solid Earth, 110(B1).

Hurter, S., and Schellschmidt, R. (2003). "Atlas of Geothermal Resources in Europe." Geothermics, 32(4-6), 779-787.

Hurtig, E. "Heat Conductivity Measurements under Uniaxial Pressure." Proc., IASPEI/IAGA general assembly (programme and abstracts), Comite Espanol Organizador de las Asambleas generales Cientificas IASPEI/IAGA Internat. Assoc Seismology and Phys. Earth's Interior Internat. Assoc Seismology and Phys. Earth's Interior.

Johansen, T. A. (1975). "Thermal Conductivity of Soils." US Army Corps of Engineers, Trondheim, Hanover, New Hampshire.

Kappelmeyer, O., and Haenel, R. (1974). Geothermics with Special Reference to Application, Berlin, Gebrüder Borntraeger, 1974.

Khandelwal, M. (2012). "Application of an Expert System to Predict Thermal Conductivity of Rocks." Neural Computing & Applications, 21(6), 1341-1347.

Kittel, C. (1949). "Interpretation of the Thermal Conductivity of Glasses." Physical Review, 75(6), 972-974.

Kjorholt, H., Dahlo, T. S., and Broch, E. (1992). Geotechnical Design of Air-Cushion Surge Chambers.

Klein, C., Hurlbut, C. S., and Dana, J. D. (1999). Manual of Mineralogy, Wiley.

Krupiczk, R. (1967). "Analysis of Thermal Conductivity in Granular Materials." International Chemical Engineering, 7(1), 122-&.

Kukkonen, I., and Lindberg, A. (1998). "Thermal Properties of Rocks at the Investigation Sites: Measured and Calculated Thermal Conductivity, Specific Heat Capacity and Thermal Diffusivity." L. Eskola, ed., Posiva, Finland, 32.

Kukkonen, I. T., Jokinen, J., and Seipold, U. (1999). "Temperature and Pressure Dependencies of Thermal Transport Properties of Rocks: Implications for Uncertainties in Thermal Lithosphere Models and New Laboratory Measurements of High-Grade Rocks in the Central Fennoscandian Shield." Surveys in Geophysics, 20(1), 33-59.

Kutas, R. I. (1977). "Investigation of Heat Flow in the Territory of the Ukraine." Tectonophysics, 41(1), 139-145.

Lee, Y. M., and Deming, D. (1998). "Evaluation of Thermal Conductivity Temperature Corrections Applied in Terrestrial Heat Flow Studies." Journal of Geophysical Research, 103(B2), 2447-2454.

Makinson, R. E. B. (1938). "The Thermal Conductivity of Metals." Proceedings of the Cambridge Philosophical Society, 34, 474-497.

Miao, S. Q., Li, H. P., and Chen, G. (2014). "Temperature Dependence of Thermal Diffusivity, Specific Heat Capacity, and Thermal Conductivity for Several Types of Rocks." Journal of Thermal Analysis and Calorimetry, 115(2), 1057-1063.

Molgaard, J., and Smeltzer, W. W. (1971). "Thermal Conductivity of Magnetite and Hematite." Journal of Applied Physics, 42(9), 3644-&.

Mottaghy, D., Vosteen, H. D., and Schellschmidt, R. (2008). "Temperature Dependence of the Relationship of Thermal Diffusivity Versus Thermal Conductivity for Crystalline Rocks." International Journal of Earth Sciences, 97(2), 435-442.

Nabelek, P. I., Whittington, A. G., and Hofmeister, A. M. (2010). "Strain Heating as a Mechanism for Partial Melting and Ultrahigh Temperature Metamorphism in Convergent Orogens: Implications of Temperature-Dependent Thermal Diffusivity and Rheology." Journal of Geophysical Research - Part B - Solid Earth, 115(B12), (17 pp.).

Ozbek, H., and Phillips, S. L. (1979). "Thermal Conductivity of Aqueous NaCl Solutions from 20 C to 330 C." Lawrence Berkeley Laboratory, University of California Berkeley, California, USA, 25.

Pilchin, A., and Eppelbaum, L. (1997). "Determination of the Lower Edges of Magnetized Bodies by Using Geothermal Data." Geophysical Journal International, 128(1), 167-174.

Poelchau, H. S., Baker, D. R., Hantschel, T., Horsfield, B., and Wygrala, B. (1997). "Basin Simulation and the Design of the Conceptual Basin Model." Petroleum and Basin Evolution, D. Welte, B. Horsfield, and D. Baker, eds., Springer Berlin Heidelberg, 3-70.

Powell, R. W., Ho, C. Y., and Liley, P. E. (1966). Thermal Conductivity of Selected Materials, Washington, D.C. : U.S. Dept. of Commerce, National Bureau of Standards : For sale by the Supt. of Docs., U.S. G.P.O., [1966].

Pribnow, D., Williams, C. F., Sass, J. H., and Keating, R. (1996). "Thermal Conductivity of Water-Saturated Rocks from the KTB Pilot Hole at Temperatures of 25 to 300 degC." Geophysical Research Letters, 23(4), 391-394.

Ratcliffe, E. H. (1959). "Thermal Conductivities of Fused and Crystalline Quartz." British Journal of Applied Physics, 10(1), 22-25.

Ray, L., Roy, S., and Srinivasan, R. (2008). "High Radiogenic Heat Production in the Kerala Khondalite Block, Southern Granulite Province, India." International Journal of Earth Sciences, 97(2), 257-267.

Robie, R. A. (1988). Debye Temperatures of Selected Silicate Minerals, [Denver, Colo.?] : Dept. of the Interior, Geological Survey : [Books and Open-File Reports Section, distributor], 1988.

Rybach, L., and Cermak, V. (1987). "The Depth Dependence of Heat-Production in the Continental Lithosphere, Derived from Seismic Velocities." Geophysical Research Letters, 14(3), 311-313.

Sass, J. H. (1965). "The Thermal Conductivity of Fifteen Feldspar Specimens." Journal of Geophysical Research, 70(16), 4064.

Sass, J. H., Lachenbruch, A. H., Moses, T. H., and Morgan, P. (1992). "Heat-Flow from a Scientific-Research Well at Cajon Pass, California." Journal of Geophysical Research-Solid Earth, 97(B4), 5017-5030.

Scharli, U., and Rybach, L. (2001). "Determination of Specific Heat Capacity on Rock Fragments." Geothermics, 30(1), 93-110.

Schwab, R. G. (1974). "What Do We Know about the Deeper Layers of the Earth?" Angewandte Chemie International Edition, 13(9), 580.

Scorer, J. (1950). "Relationship between Thermal Conductivity and other Rock Properties." M.S. Thesis, University of California, Berkeley.

Seipold, U. (1995). "The Variation of Thermal Transport-Properties in the Earths Crust." Journal of Geodynamics, 20(2), 145-154.

Seipold, U. (1998). "Temperature Dependence of Thermal Transport Properties of Crystalline Rocks - A General Law." Tectonophysics, 291(1-4), 161-171.

Sekiguchi, K. (1984). "A Method for Determining Terrestrial Heat-Flow in Oil Basinal Areas." Tectonophysics, 103(1-4), 67-79.

Sharma, P. V. (1997). Environmental and Engineering Geophysics, Cambridge University Press.

Shaw, D. B., and Weaver, C. E. (1965). "The Mineralogical Composition of Shales." Journal of Sedimentary Petrology, 35(1), 213-&.

Somerton, W. H. (1992). Thermal Properties and Temperature-Related Behavior of Rock/Fluid Systems, Elsevier, California.

Thalmann, R. E. (1950). "Thermal Conductivity of Dry Soils." M.S., Univ. of Kansas, Lawrence.

Tian, H., Kempka, T., Xu, N. X., and Ziegler, M. (2012). "Physical Properties of Sandstones after High Temperature Treatment." Rock Mechanics and Rock Engineering, 45(6), 1113-1117.

Tritt, T. M. (2004). Thermal Conductivity: Theory, Properties and Applications, Springer.

Vosteen, H. D., and Schellschmidt, R. (2003). "Influence of Temperature on Thermal Conductivity, Thermal Capacity and Thermal Diffusivity for Different Types of Rock." Physics and Chemistry of the Earth, 28(9-11), 499-509.

Walsh, J. B., and Decker, E. R. (1966). "Effect of Pressure and Saturating Fluids on the Thermal Conductivity of Compact Rock." Journal of Geophysical Research, 71, 3053-3061.

Woodside, W. (1958). "Calculation of the Thermal Conductivity of Porous Media." Canadian Journal of Physics, 36(7), 815-823.

Yoder, H. S. (1976). Generation of Basaltic Magma, Washington : National Academy of Sciences, 1976.

CHAPTER 3

ENGINEERED GRANULAR MATERIALS FOR HEAT CONDUCTION AND LOAD TRANSFER IN ENERGY GEO-TECHNOLOGY

3.1. INTRODUCTION

Heat transfer is a critical process in many energy geo-systems. Examples include thermal energy geo-storage, near-surface thermal foundations, deep geothermal energy reservoirs, buried high voltage power transmission cables and liquified natural gas storage among others. The performance of these systems is determined by the sediments' thermal capacitance and heat conduction, in addition to their ability to sustain mechanical loads and allow for fluid flow as needed.

Thermally engineered composites have been developed to satisfy a wide range of industrial and consumer product needs such as low thermal expansion to minimize thermo-mechanical stresses and high thermal conductivity for fast heat dissipation; at the same time, materials may be required to satisfy other constrains such as low specific gravity, high strength and low compressibility (Zweben, 1998). Typically, these composites have a polymer, metal, ceramic or carbon matrix, and include additives to attain high conductivity (e.g., boron nitride, aluminum nitride, silicon carbide, alumina, fused silica, metallic flakes or ceramic powders - Mallik et al., 2011). Materials are designed for low thermal conductivity as well; for example, there are alloys that hinder heat dissipation (Golosnoy et al., 2009; Gupta et al., 2013).

Thermally engineered materials and composites for the construction industry often involve low thermal conductivity components such as hollow glass microspheres (Yun et al., 2013), petroleum coke, fly ash, polypropylene fibers and air entraining additives (Jiang et al., 2013; Olmeda et al., 2013). High thermal conductivity concrete and grouts used in geothermal systems contain high conductivity aggregates (e.g., silica sand, limestone sand, pulverized fuel ash, electric arc furnace slag) and are mixed at a low water-cement ratio with the addition of superplasticizers (Allan, 2000; Borinaga-Trevino et al., 2013).

The purpose of this manuscript is to explore the range of thermal conductivity values attainable with granular materials. The experimental study documented herein explores natural and engineered granular materials under a wide range of stress conditions. Fundamental concepts and previous studies are reviewed first.

3.2. PREVIOUS STUDIES

3.2.1. Fundamentals of Heat Conduction

Heat conduction in non-metal solids takes place via lattice vibrations or phonons whereby normal mode harmonic oscillations transport thermal energy across the medium. While heat conduction in metals also includes phononic transmission, it is mainly dominated by collision and diffusion of free electrons – Note: electron movements are not organized as in macroscopic electric currents (Chaikin and Lubensky, 2000). Heat conduction in liquids and gases takes place through inter-molecular collisions so that the internal energy of atoms and molecules diffuses throughout the medium by random motions (Wachsmuth, 1901). Thermal conductivity is lower in gases than in liquids or solids due to the larger distance between neighboring molecules in gas.

3.2.2. Heat Conduction across Solid-Solid and Solid-Liquid Interfaces

Consider two bodies in contact subjected to a thermal gradient. A temperature difference develops across the interface between the two bodies; this implies the presence of thermal contact resistance. In fact, there is an interface thermal resistance even between pure and atomically smooth surfaces and between a solid with a smooth surface and a liquid (Kapitza, 1941). Contact resistance results from phonon scattering, and electrons and molecular elastic impacts at boundaries. Consequently, the geometric and physical characteristics of the two bodies in thermal contact affect the thermal contact resistance (Fletcher, 1972). The thermal contact resistance is defined as the ratio of the temperature discontinuity at the interface and the power per unit area across the interface (Swartz and Pohl, 1989).

The free electron movement in metals vanishes at the contact with a non-metal body (Luo and Lloyd, 2010). Experimental measurements show lower thermal contact resistance than model predictions in metal-nonmetal interfaces probably due to the coupling between phonons (either in the metal or in the non-metal) and metal electrons (Cahill et al., 2003; Majumdar and Reddy, 2004).

3.2.3. Heat Conduction in Soils

Granular materials, including soils, are inherently multi-phase. Grains are much smaller than the length scale of the system under analysis, and the granular medium can be treated as an equivalent continuum with effective properties (Torquato, 2001). Still, a particle-scale understanding of heat transport is needed to engineer geomaterials in view of thermal applications. Heat transfer in granular materials combines conduction, convection and radiation processes (Gemant, 1950; Woodside and Messmer, 1961a). In

addition, grain motion and mixing are important heat transfer processes where soils are subjected to high-strain shear, for example within shear bands and during granular flow (Rognon and Einav, 2010). Convective transport is negligible in static dry granular materials and in water-saturated sediments with small pore size when $D_{50} < 6$ mm (Thalmann, 1950; Woodside, 1958). Radiation gains relevance at high temperature, above ~ 1000˚C. In summary, conduction is the dominant heat transfer process in dry soils under static conditions. The presence of liquids facilitates heat transfer through granular contacts and across the porous medium. The underlying processes include: heat conduction through the pore filling liquid, improved heat conduction across contacts as liquids fill voids within surface roughness, convection in the pore space and advection in cyclic fluid flow (Vafai and Thiyagaraja, 1987; Yun et al., 2011).

Analytical and experimental studies have explored the evolution of thermal conduction in granular materials with changes in effective stress, water content, fines content, mineral composition and temperature (Farouki, 1981; Hadley, 1986; Watson and McCarthy, 2002; Huetter et al., 2008; Yun and Santamarina, 2008; Tarnawski et al., 2009a; Tarnawski et al., 2009b; Malherbe et al., 2012). Research results show that the number and quality of contacts between particles, and the thermal conductivity of the material that makes the grains determine the thermal conductivity of the dry granular medium. Interparticle coordination and contact area are functions of grain size distribution, particle shape, current state of effective stress and stress history. Furthermore, interparticle coordination and contact areas can increase due to diagenetic processes such as cementation, precipitation and pressure dissolution/precipitation (Cortes et al., 2009).

3.2.4. Summary of Properties

The thermal conductivity of common geomaterials and fluids are summarized in Table 3.1; heat capacity and mass density are included for completeness.

Table 3.1. Physical properties of geomaterials and fluids (at room temperature)

Material Category	Material		Thermal Conductivity k [$W.m^{-1}.K^{-1}$]	Specific Heat Capacity C_p [$J.kg^{-1}.K^{-1}$]	Density ρ [kg/m^3]
Metals	Silver (pure)		424	235	10476
	Copper		392	385	8906
	Nickel		60	440	8890
Coats	Copper/Silver-filled coating		9.1[(a)]	-	2110
	Nickel-filled coating		2.58[(a)]	-	2030
Geomaterials	Quartz (single crystal)		12 (∥) - 6.8 (⊥)	753	2650
	Quartz (crystalline silica)		1.4	712	2203
	Glass (amorphous silica)		1.02	753	2467
	Granite		1.7 – 4	795	2700
	Limestone		1.3	921	2560
	Marble		2.6	879	2595
	Shale		1.56	628	2675
	Sandstone		1.7	921	2580
	Gypsum		0.43	1084	1249
	Coal		0.17	1256	1442
	Sand	dry	0.15 - 0.33	795	1800
		water saturated	2 – 4	2151 (n=0.4)	2000
Pore filler fluids	Thermal grease (silver-based)		8.9	1005	2450
	Nanofluid (water + Al_2O_3)		0.72	2302	1350 (c=10%)
	Water		0.6	4186	998
	Ice (0 ˚C)		2.2	2038	921
	Kerosene		0.15	2093	820
	Air		0.024	1005	1.2
Insulators	Silica aerogel		0.004 – 0.03	840	3
	Polystyrene		0.03	100	1050

Sources: ASHRAE (2009); [(a)] mgchemicals (2013).

Thermal conductivity values confirm efficient heat conduction in metals, the advantages of crystal structure over liquid phase (e.g., ice vs. water), and the effect of crystal structure and phonon wavelength on conduction (e.g., methane hydrate vs. ice, and quartz vs. glass).

3.3. EXPERIMENTAL PROCEDURE

The bulk thermal conductivity of natural and engineered dry granular materials and its changes upon loading and unloading are studied next. The tested materials are selected to obtain the widest possible range in thermal conductivity for load-bearing dry granular materials; moreover, two additional quartzitic sand specimens are prepared by spraying the sand with high thermal conductivity silver/copper and nickel paints under continuous mixing to prevent cementation. The mineral composition and mean grain size are summarized in Table 3.2.

Table 3.2. Materials tested in this study

Material		Mean size D_{50} [mm]	Density*		Thermal conductivity*	
			ρ_1 [kg/m^3]	χ [%]	k_1 [W.m^{-1}.K^{-1}]	β [%]
Quartzitic sand (40/50)	uncoated	0.36	1594	0.6	0.157	40
	Nickel coated	0.4	1596	0.7	0.201	36
	Silver/Copper coated	0.4	1595	0.6	0.103	100
Fly ash		0.012	1137	1.3	0.131	7.8
Diatomaceous earth		0.008	543	3.3	0.086	4.4
Ceramic microspheres		0.2	400	2.3	0.093	2.9
Glass microspheres		0.018	326	1.5	0.056	3.7

*Note: values reported for the unloading trend.

Tests are conducted inside a k_o oedometer chamber under zero-lateral strain conditions. The cell wall is coated with petroleum gel and covered with a thin polymer wrap to minimize the effect of wall friction on thick specimens. The selected sediment is poured inside the chamber and tapped to obtain a dense, mechanically stable specimen. The vertical stress is doubled at each loading stage, and the thermal conductivity is measured at every stage after a 10 minute equilibration period.

The thermal needle probe used in this study consists of a thin heating wire (length l_{HW} = 68 mm and electrical resistance R_{HW} = 70.7 Ω) and a type E thermocouple; both are housed within a stainless steel cylindrical hollow tube (length L_N = 55 mm, diameter D_N = 1.3 mm). The needle perimeter exceeds the mean diameter of tested particles ($\pi.D_N$ = 4.1 mm > d_{grain} ~ 0.4 mm). Figure 3.1 shows the test configuration and peripheral devices.

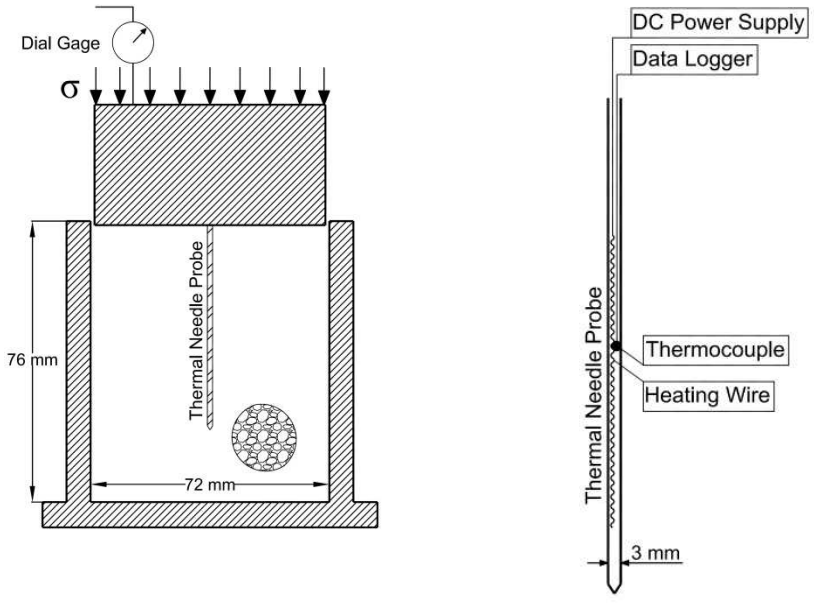

Figure 3.1. Schematic view of devices. (a) Chamber for concurrent thermal conductivity and settlement measurements. (b) Thermal needle probe.

A specified voltage (V = 3 Volt) is applied across the heating wire for 180 s. The thermocouple measures the temperature evolution during heating and cooling. Figure 3.2 shows typical data gathered for quartzitic sand. The early part of the curve is affected by diffusion, while temperatures measured towards the end of the heating period are affected by boundaries. Hence, the thermal conductivity coefficient k [$W.m^{-1}.K^{-1}$] is calculated from the slope of the central part of the temperature versus log(time) trend:

$$k = \frac{Q}{4\pi}\frac{\log(t_2/t_1)}{T_2 - T_1} \tag{3.1}$$

where Q [W/m] is the imposed power per unit length of the heating wire, and T_1-t_1 and T_2-t_2 are temperature-time pairs in the linear part of the curve. The test procedure is validated by measuring the thermal conductivity of water stabilized with 5 g/l of agar (Von Herzen and Maxwell, 1959; ASTM Standard D5334, 2008).

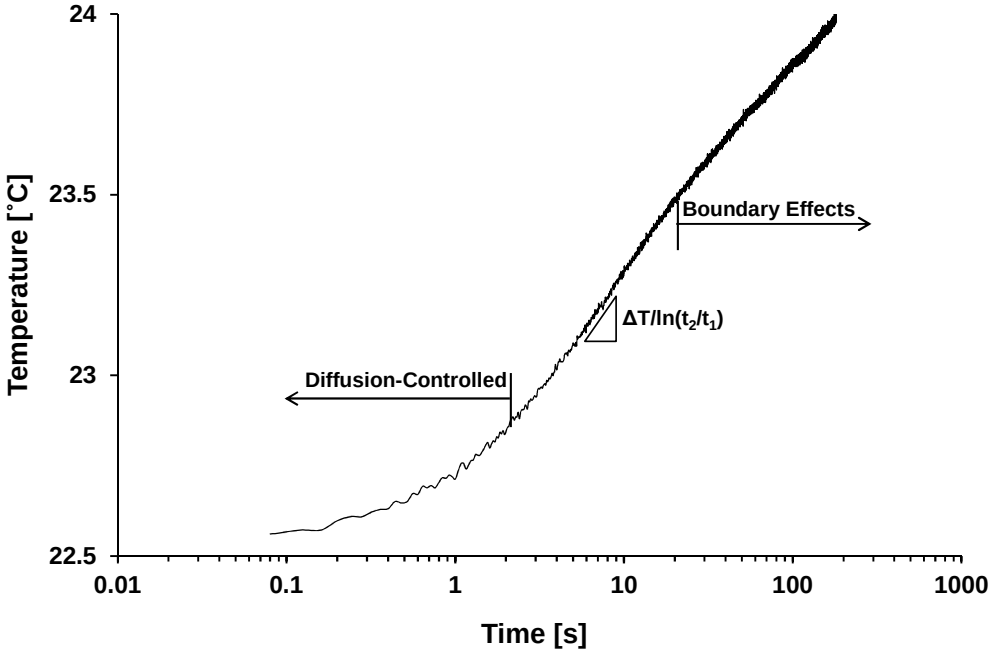

Figure 3.2. Typical dataset in semi-log scale: Temperature evolution during heating (Case: quartzitic sand at σ' = 41 kPa).

3.4. EXPERIMENTAL RESULTS

Figure 3.3 shows the evolution of mass density with applied vertical stress during loading and unloading paths for all specimens. The choice of mass density instead of void ratio facilitates the comparison among specimens made of solid particles (quartzitic sand) and porous grains (fly ash, diatomaceous earth and microspheres).

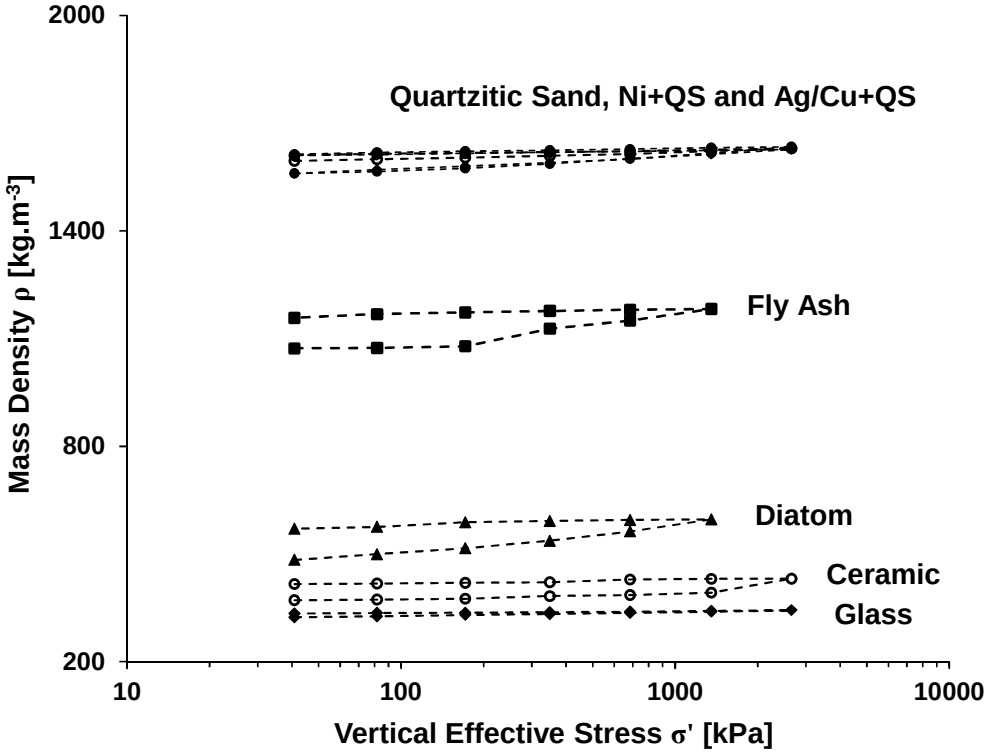

Figure 3.3. Compressibility: Density versus vertical effective stress - All specimens.

Density and thermal conductivity trends can be fitted as:

$$\rho = \rho_1\left[1 + \chi \log\left(\sigma'/1\,\text{kPa}\right)\right] \tag{3.2}$$

$$k = k_1\left[1 + \beta \log\left(\sigma'/1\,\text{kPa}\right)\right] \tag{3.3}$$

where ρ_1 and k_1 are the density and thermal conductivity at σ' = 1 kPa; the dimensionless factors χ and β capture the proportional increase in corresponding properties for a ten-fold increase in stress. Values reported in Table 3.2 apply to the

unloading branch to avoid the effects of grain crushing during first loading (Note: the compressibility of fly ash and diatomaceous earth was very pronounced during first loading). The following observations can be made from these results:

- The thermal conductivity increases with stress level in all cases (Figure 3.4), particularly in quartzitic sand samples with and without coating (β = 0.4-to-1.0, i.e., 40% to 100% for a ten-fold increase in stress).

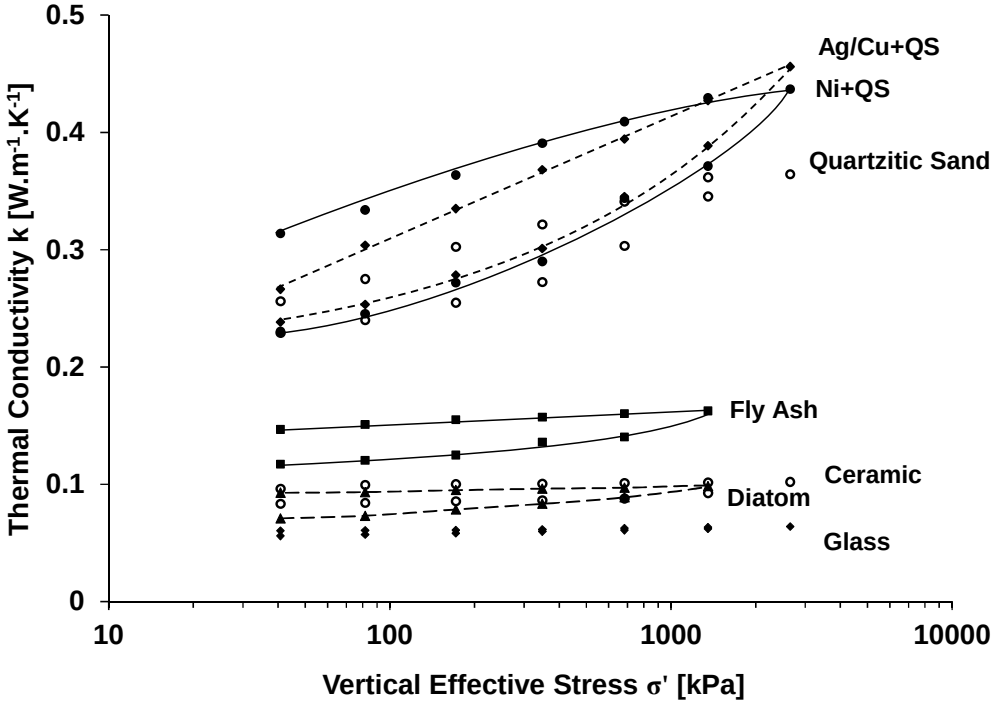

Figure 3.4. Thermal conductivity versus vertical effective stress – All specimens.

- On the other hand, the increase in thermal conductivity with stress in hollow glass microspheres, ceramic microspheres and diatoms is very low (β < 5% for a ten-fold increase in stress) even though these materials are more compressible (χ = 1.5% to 3.3%) than the quartzitic sand specimens ($\chi \approx$ 0.6%). Thus, the increase in interparticle coordination has a lessened effect in granular media made of low thermal conductivity grains (Table 3.2).

- Ceramic microspheres crush when $\sigma' \approx 1$ MPa, grains rearrange and there is a sharp increase in bulk mass density (from $\rho = 392$ kg.m^{-3} to $\rho = 431$ kg.m^{-3}). Particle crushing and rearrangement change the grain size distribution in ceramic microspheres; this is accompanied by increased mass density, inter-particle coordination and a marked increase in thermal conductivity (from $k = 0.093$ W.m^{-1}.K^{-1} to $k = 0.102$ W.m^{-1}.K^{-1}).
- Metal coatings enhance the thermal conductivity of quartzitic sand by ~10%-to-30%, depending on stress levels. Two contact-level observations explain the relatively low gain in thermal conductivity. First, optical images of coated sand grains reveal that about 60% of the grain surfaces were coated with high thermal conductivity paint; therefore, there are low thermal resistant metal-metal contacts, intermediate metal-quartz and high thermal resistant quartz-quartz contacts in these granular packings. Second, phonon-electron coupling at metal-quartz contacts is not a major improvement over quartz-quartz contacts at room temperature.
- Fly ash exhibits an intermediate behavior between solid quartzitic grains and porous diatoms and microspheres. We note that this fly ash specimen contains ~17% ferromagnetic particles, yet the thermal conductivity of iron in these particles is restricted by oxidation (Fe_3O_4 and Fe_2O_3).

Figure 3.5 shows thermal conductivity versus bulk mass density for all specimens and stress levels. There is an overall increase in thermal conductivity with density. However, these results suggest that a single conductivity-density trend is unwarranted for granular materials in general.

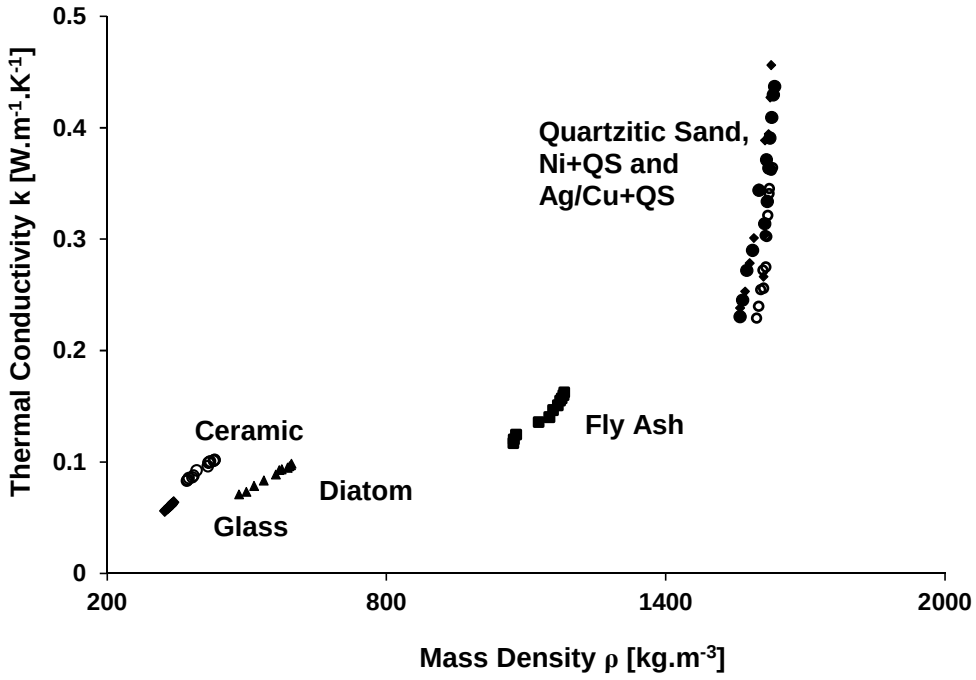

Figure 3.5. Thermal conductivity versus density - All specimens.

3.5. DISCUSSION: LIQUID EFFECTS

The number and the "thermal quality" of contacts between particles determine the thermal conductivity of dry granular materials (Yun and Santamarina, 2008). Liquids coat grains, bridge the inter-particle contacts and fill pores (depending on the degree of saturation); therefore, liquids can affect the thermal conductivity of wet or saturated sediments significantly (Hadley, 1986). Models to estimate the thermal conductivity of liquid-saturated granular materials k_{sat} are a function of porosity n, the saturating liquid thermal conductivity k_ℓ, and the thermal conductivity of the mineral that makes the particles k_s. The geometric mean is a good first-order estimate (Beck, 1976):

$$k_{sat} = (k_s)^{1-n}(k_\ell)^n \tag{3.4}$$

The thermal conductivity k_{wet} at an intermediate liquid saturation S_ℓ can be interpolated between the effective thermal conductivity of the granular medium at saturated k_{sat} and dry k_{dry} states (Johansen, 1975; Ewen and Thomas, 1987):

$$k_{wet} = k_{dry} + \left(1 - e^{-0.89 S_\ell}\right)\left(k_{sat} + k_{dry}\right) \tag{3.5}$$

These equations highlight the role of the pore fluid conductivity k_ℓ; for example, the thermal conductivity of dry quartzitic sand k_{dry} = 0.23 $W.m^{-1}.K^{-1}$ with porosity n = 0.4 would increase to k_{sat} = 2.8 $W.m^{-1}.K^{-1}$ when it is water-saturated (equation 3.4 – data in Table 3.1). For comparison, the improvement in thermal conductivity by metal coating was only from k_{dry} = 0.25 $W.m^{-1}.K^{-1}$ without coating to k_{dry} = 0.32 $W.m^{-1}.K^{-1}$ after coating.

3.6. CONCLUSIONS

Dry and densely packed hollow glass microspheres, ceramic microspheres and naturally occurring diatomaceous earth are more compressible than sands, but exhibit very low thermal conductivity and very low stress-dependent gain in thermal conductivity. Therefore, these materials are advantageous for applications that require heat insulation along with mechanical stability. Ceramic microspheres crush at lower stress levels than hollow glass microspheres. Diatomaceous earth, glass and ceramic microspheres can be mixed with other grains to tune their thermo-mechanical response.

Quartzitic sand exhibits high thermal conductivity due to the conductive nature of quartz, albeit diminished by contact resistance between grains. The number of contacts and contact thermal quality (the inverse of contact resistance) increase with confining stress and thermal conductivity shows pronounced stress-dependency. Variation in dry mass density is not a sufficient indicator of variation in thermal conductivity.

Metal coating grains improves the bulk conductivity of quartz sand by ~10%-to-30%. This limited improvement reflects partial grain coating and the mismatch between phononic and electronic conduction. The liquid that fills the pore network in granular materials has a more pronounced effect on the bulk thermal conductivity of the medium than metal coating grains. Therefore, high thermal conductivity granular materials can be best engineered by controlling the saturating liquid.

3.7. REFERENCES

Allan, M. L. (2000). "Materials Characterization of Superplasticized Cement-Sand Grout." Cement and Concrete Research, 30(6), 937-942.

ASTM Standard D5334 (2008). "Standard Test Method for Determination of Thermal Conductivity of Soil and Soft Rock by Thermal Needle Probe Procedure." ASTM International, West Conshohocken, PA, DOI: 10.1520/ D5334-1508, www.astm.org.

Beck, A. E. (1976). "Improved Method of Computing the Thermal Conductivity of Fluid-Filled Sedimentary Rocks." Log Analyst, 17(6), 30-38.

Borinaga-Trevino, R., Pascual-Munoz, P., Castro-Fresno, D., and Jose Del Coz-Diaz, J. (2013). "Study of Different Grouting Materials Used in Vertical Geothermal Closed-Loop Heat Exchangers." Applied Thermal Engineering, 50(1), 159-167.

Cahill, D. G., Ford, W. K., Goodson, K. E., Mahan, G. D., Majumdar, A., Maris, H. J., Merlin, R., and Phillpot, S. R. (2003). "Nanoscale Thermal Transport." Journal of Applied Physics, 93(2), 793-818.

Chaikin, P. M., and Lubensky, T. C. (2000). Principles of Condensed Matter Physics, Cambridge University Press.

Cortes, D. D., Martin, A. I., Yun, T. S., Francisca, F. M., Santamarina, J. C., and Ruppel, C. (2009). "Thermal Conductivity of Hydrate-Bearing Sediments." Journal of Geophysical Research-Solid Earth, 114(B11103), 1-10.

Ewen, J., and Thomas, H. R. (1987). "The Thermal Probe - A New Method and Its Use on an Unsaturated Sand." Geotechnique, 37(1), 91-105.

Farouki, O. T. (1981). "The Thermal-Properties of Soils in Cold Regions." Cold Regions Science and Technology, 5(1), 67-75.

Fletcher, L. S. (1972). "A Review of Thermal Control Materials for Metallic Junctions." 7th Thermophysics Conference, American Institute of Aeronautics and Astronautics.

Gemant, A. (1950). "The Thermal Conductivity of Soils." Journal of Applied Physics, 21(8), 750-752.

Golosnoy, I. O., Cipitria, A., and Clyne, T. W. (2009). "Heat Transfer Through Plasma-Sprayed Thermal Barrier Coatings in Gas Turbines: A Review of Recent Work." Journal of Thermal Spray Technology, 18(5-6), 809-821.

Gupta, M., Curry, N., Nylen, P., Markocsan, N., and Vassen, R. (2013). "Design of Next Generation Thermal Barrier Coatings - Experiments and Modelling." Surface & Coatings Technology, 220(2013), 20-26.

Hadley, G. R. (1986). "Thermal Conductivity of Packed Metal Powders." International Journal of Heat and Mass Transfer, 29(6), 909-920.

Huetter, E. S., Koemle, N. I., Kargl, G., and Kaufmann, E. (2008). "Determination of the Effective Thermal Conductivity of Granular Materials under Varying Pressure Conditions." Journal of Geophysical Research-Planets, 113(E12004), 1-11.

Jiang, Y., Yang, J., and Chen, Y. (2013). "Environmentally Friendly Cellular Concrete for Wall Insulation." Testing and Evaluation of Advanced Building Materials, W. Yao, ed., 271-275.

Johansen, T. A. (1975). "Thermal Conductivity of Soils." US Army Corps of Engineers, Trondheim, Hanover, New Hampshire.

Luo, T., and Lloyd, J. R. (2010). "Equilibrium Molecular Dynamics Study of Lattice Thermal Conductivity/Conductance of Au-SAM-Au Junctions." Journal of Heat Transfer-Transactions of the Asme, 132(3).

Majumdar, A., and Reddy, P. (2004). "Role of Electron-Phonon Coupling in Thermal Conductance of Metal-Nonmetal Interfaces." Applied Physics Letters, 84(23), 4768-4770.

Mallik, S., Ekere, N., Best, C., and Bhatti, R. (2011). "Investigation of Thermal Management Materials for Automotive Electronic Control Units." Applied Thermal Engineering, 31(2-3), 355-362.

Olmeda, J., Sanchez de Rojas, M. I., Frias, M., Donatello, S., and Cheeseman, C. R. (2013). "Effect of Petroleum (PET) Coke Addition on the Density and Thermal Conductivity of Cement Pastes and Mortars." Fuel, 107(2013), 138-146.

Rognon, P., and Einav, I. (2010). "Thermal Transients and Convective Particle Motion in Dense Granular Materials." Physical Review Letters, 105(21).

Swartz, E. T., and Pohl, R. O. (1989). "Thermal Boundary Resistance." Reviews of Modern Physics, 61(3), 605-668.

Tarnawski, V. R., Momose, T., Leong, W. H., Bovesecchi, G., and Coppa, P. (2009b). "Thermal Conductivity of Standard Sands. Part I. Dry-State Conditions." International Journal of Thermophysics, 30(3), 949-968.

Thalmann, R. E. (1950). "Thermal Conductivity of Dry Soils." M.S., Univ. of Kansas, Lawrence.

Torquato, S. (2001). Random Heterogeneous Materials, Springer-Verlag, New York.

Vafai, K., and Thiyagaraja, R. (1987). "Analysis of Flow and Heat Transfer at the Interface Region of a Porous Medium." International Journal of Heat and Mass Transfer, 30(7), 1391-1405.

Von Herzen, R., and Maxwell, A. E. (1959). "The Measurement of Thermal Conductivity of Deep-Sea Sediments by a Needle Probe Method." Journal of Geophysical Research, 64(10), 1557-1563.

Wachsmuth, R. (1901). "The Internal Heat Conduction in Liquids." Physikalische Zeitschrift, 3(4), 79-80.

Woodside, W. (1958). "Calculation of the Thermal Conductivity of Porous Media." Canadian Journal of Physics, 36(7), 815-823.

Woodside, W., and Messmer, J. H. (1961a). "Thermal Conductivity of Porous Media. 1-Unconsolidated Sands." Journal of Applied Physics, 32(9), 1688-1699.

Yun, T. S., Dumas, B., and Santamarina, J. C. (2011). "Heat Transport in Granular Materials during Cyclic Fluid Flow." Granular Matter, 13(1), 29-37.

Yun, T. S., Jeong, Y. J., Han, T. S., and Youm, K. S. (2013). "Evaluation of Thermal Conductivity for Thermally Insulated Concretes." Energy and Buildings, 61, 125-132.

Yun, T. S., and Santamarina, J. C. (2008). "Fundamental Study of Thermal Conduction in Dry Soils." Granular Matter, 10(3), 197-207.

Zweben, C. (1998). "Advances in Composite Materials for Thermal Management in Electronic Packaging." Jom-Journal of the Minerals Metals & Materials Society, 50(6), 47-51.

CHAPTER 4

ENGINEERED SOILS: SATURATED GRANULAR MIXTURES

4.1. INTRODUCTION

Engineered granular materials with controlled hydraulic, mechanical and thermal properties can be effective solutions for systems subjected to coupled excitations such as thermal energy geo-storage, granular beds for buried high voltage power cables, buffer materials for nuclear waste isolation, and heat extraction or injection through shallow or deep thermal foundations.

The performance of granular media subjected to thermal, mechanical and hydraulic processes depends on their physical properties such as mineralogy, particle size distribution, fabric, pore fluid characteristics, degree of saturation, and the imposed boundary conditions such as the state of stress.

The thermal performance of uniform granular materials has been explored in the literature. However, few attempts have been made to engineer soil properties. Furthermore, available models appear insufficient for the prediction of the thermal conductivity of engineered granular mixtures.

The aim of this study is to investigate the effect of particle size on mono-sized systems (relates to inter-particle contact area), grain size distribution (i.e., the number of inter-particle contacts), saturating fluid (i.e., enhanced heat conduction through pore fluid and inter-particle contacts), and effective stress level (i.e., inter-particle contact area and

reduced contact impedance) on the thermal conductivity and compressibility of granular materials with high quartz content.

4.2. PREVIOUS STUDIES

Thermal conduction and load transfer in dry granular media take place through inter-particle contacts. Discontinuities at inter-particle contacts add thermal resistance to heat transfer even if particles have perfectly smooth surfaces. The effect of salient parameters on the thermal conductivity of granular media is reviewed next.

4.2.1. Contact Thermal Impedance

Particle surface asperities and the presence of a thin air layer between dry particles in contact cause a mismatch between phononic heat conduction. The ensuing local thermal resistance manifests as a temperature jump at contacts (Note: the thermal discontinuity decreases at higher gas pressures – Birch and Clark, 1940a). Small contact areas and contact resistance make the thermal conductivity of a granular medium significantly lower than that of the material that makes the grains.

Contact heat conductance H_c [$W.K^{-1}$] is proportional to the conductivity of the grain material k_s [$W.m^{-1}.K^{-1}$] and the radius of the contact region r_c [m] (Vargas and McCarthy, 2002):

$$H_c = 2 r_c k_s \tag{4.1}$$

Models of contact resistance/conductance may also involve surface curvature, roughness and the mode of particle deformation (Sridhar and Yovanovich, 1994; Lambert and Fletcher, 1997).

4.2.2. Stress Effects

The state of stress plays a critical role on all properties of a granular material. In particular, the thermal conductivity of granular materials increases with increasing normal stress (Knutsson, 1983; Tehranian et al., 1994). The effective stress causes compaction, increases the number of inter-particle contacts, and enlarges the radius r_c [m] of the contact area between particles (Yun and Santamarina, 2008).

The inter-particle contact radius r_c [m] for two same-sized spherical particles is related to grains radius R [m], Poisson's ratio ν_g and shear stiffness G_g [GPa] of the mineral that makes the grains, and the applied boundary effective stress σ' [kPa] as predicted by Hertz's nonlinear elastic contact theory – simple cubic packing (Santamarina et al., 2001):

$$\frac{r_c}{R} = \left[\frac{3(1-\nu_g)}{2}\frac{\sigma'}{G_g}\right]^{\frac{1}{3}} \tag{4.2}$$

Combining Equations 4.1 and 4.2, the heat conductance H_c [$W.K^{-1}$] is:

$$H_c = 2k_s R\left[\frac{3(1-\nu_g)}{2}\frac{\sigma'}{G_g}\right]^{\frac{1}{3}} \tag{4.3}$$

Equation 4.3 predicts that the contact conductance increases when grains are large R [m], are made of a material of high thermal conductivity k_s [$W.m^{-1}.K^{-1}$], and are subjected to high effective stress σ' [kPa] (Weidenfeld et al., 2004).

Measured thermal conductivity values show a residual memory effect: they are higher in unloading than during loading because of irreversible fabric changes, contact deformations, and locked in stresses (Abyzov et al., 2014).

4.2.3. Dry Mass Density and Porosity

Particle shape, grain size distribution and the state of stress determine the porosity and dry mass density of granular materials. An increase in dry mass density ρ_{dry} [kg.m^{-3}] or a decrease in porosity n, $n = 1-\rho_{dry}/(G_S.\rho_w)$, implies an increase in the inter-particle coordination number cn, as can be estimated from cn=12(1-n) (German, 1989), a higher number of heat conduction pathways and an increase in thermal conductivity.

Published results show a linear trend between increasing thermal conductivity versus decreasing porosity for any degree of saturation (Tang et al., 2008; Yun and Santamarina, 2008). Particle angularity and surface roughness hinder dense packing and result in lower thermal conductivity values (Becker et al., 1992; Cho et al., 2006). Suggested correlations between thermal conductivity and dry mass density or porosity are summarized in Table 4.1.

4.2.4. Liquid Saturation

The thermal conductivity of liquid-saturated soils is much higher than that of dry soils. This highlights the critical role liquids play (1) to diminish contact thermal impedance through mineral-liquid-mineral conduction, and (2) to heat conduction along the liquid filled pores.

Three volumetric averages can be used to estimate the thermal conductivity of solid-liquid mixtures. The harmonic mean considers the liquid and solid phases in series and provides a lower bound to measured experimental data. The arithmetic mean considers the liquid and solid phases in parallel with respect to the direction of heat flow, and provides an upper bound to measured data (Woodside and Messmer, 1961a). The geometric mean is a better estimate overall, however, it overestimates the effective

thermal conductivity when the ratio between solid to liquid thermal conductivities $k_s/k_\ell > 20$ (Beck, 1976). Proposed relationships for the thermal conductivity of liquid-saturated soils are listed in Table 4.1.

The thermal conductivity of quartz $k_q \sim 8$ W.m^{-1}.K^{-1} is much higher than that of most minerals (average k_o = 2 or 3 W.m^{-1}.K^{-1} - Horai, 1971) hence, the thermal conductivity of dry soils is proportional to quartz content (Table 4.1).

Table 4.1. Correlations developed for effective thermal conductivity of granular materials with respect to other salient parameters.

Relationship	Materials	Parameters	References
$k_{dry} = \frac{0.135\rho_{dry} + 64.7}{\rho_s - 0.947\rho_{dry}} \pm 20\%$	Dry soils	k_{dry}: effective dry thermal conductivity [$W.m^{-1}.K^{-1}$] ρ_{dry}: bulk dry mass density [$kg.m^{-3}$] ρ_s: mass density of solid particles (ρ_s =2700 $kg.m^{-3}$)	Johansen, 1975
$k_{dry} = 0.034n^{-2.1}$	Compacted bentonite bed	n: porosity	Knutsson, 1983
$k_{dry} = 0.0497 + 0.222(1-n) + 0.968(1-n)^3$	Compacted bentonite bed	Defined before	Sakashita and Kumada, 1998
$k_{sat} = k_\ell^n . k_s^{1-n}$ (geometric mean)	Saturated soils	k_{sat}: effective liquid-saturated thermal conductivity [$W.m^{-1}.K^{-1}$] k_ℓ: thermal conductivity of pore-filling liquid [$W.m^{-1}.K^{-1}$] k_s: thermal conductivity of solid particle [$W.m^{-1}.K^{-1}$]	Beck, 1976
$\frac{1}{k_{sat}} = \frac{n}{k_\ell} + \frac{1-n}{k_s}$ (harmonic mean)	Saturated soils	Defined before	Woodside and Messmer, 1961a
$k_{sat} = nk_\ell + (1-n)k_s$ (arithmetic mean)	Saturated soils	Defined before	Woodside and Messmer, 1961a
$k_{sat} = (n-0.03)k_\ell + (1.03-n) \times [\frac{1}{1.03-n} \times \frac{n}{k_s} + \frac{0.03}{1.03-n} \times \frac{1}{k_\ell}]^{-1}$	Saturated compacted bentonite bed	Defined before	Sakashita and Kumada, 1998
$k_{sat} = k_{dry}[1 + (9.75n - 0.706)^{0.285n+0.731}]$		Defined before	Johansen, 1975

Table 4.1.Continued Correlations developed for effective thermal conductivity of granular materials with respect to other salient parameters.

Relationship	Materials	Parameters	References
$k_s = \prod_j k_{mj}^{x_j}$ where $\sum_j^N x_j = 1$	Soil grains	k_{mj}: thermal conductivity of j-th mineral x_j: volumetric fraction of j-th mineral N: number of minerals	
$k_s = \begin{cases} 2^{1-q} \times 7.7^q & \text{for } q > 0.2 \\ 3^{1-q} \times 7.7^q & \text{for } q \leq 0.2 \end{cases}$	Soil grains	q: volumetric fraction of quartz	Johansen, 1975
$k = \frac{k_1[x + \kappa - x\varphi_2(1-\kappa)]}{x + \kappa - \varphi_2(1-\kappa)}$ $\kappa = \frac{k_2}{k_1}$ and $x = f(\kappa, \frac{a}{b})$	Dry granular mixtures	k_1: thermal conductivity of the continuous medium [$W.m^{-1}.K^{-1}$] k_2: thermal conductivity of the suspended particles [$W.m^{-1}.K^{-1}$] κ: relative thermal conductivity of components φ_2: volumetric fraction of suspended material x: particle shape factor (2 for spheres)	Fricke, 1924; Ould-Lahoucine et al., 2002
$k_{wet} = k_s^{m.\varphi_s} k_b^{n.\varphi_b} (k_w^{\varphi_w} k_a^{\varphi_a})^p$	Wet sand-bentonite mixtures	k_s, k_b, k_w, and k_a: thermal conductivity of sand particles, bentonite particles, water and air [$W.m^{-1}.K^{-1}$] φs, φs, φs, φs: volumetric fraction of sand, bentonite, water and air m = 1.303, n = 2.099, p = 0.564	Cho et al., 2011

4.2.5. Particle Size and Grain Size Distribution

Experimental results show that the thermal conductivity exhibits some increase –albeit minor– with increasing particle size as theoretically predicted for mono-size soils (Equation 4.3 - Paek et al., 2000). Indeed, smaller particles result in a higher number of contacts per unit length, but there is a lower force per particle, hence, the contact resistance increases compared to heat pathways formed by larger particles (Weidenfeld et al., 2004; Chari et al., 2013).

Most studies consider either mixtures of mono-size particles made of different constituents, or mixtures of different size grains made of the same constituent (Ould-Lahoucine et al., 2002). Some mixtures can be treated as suspensions where pastes made of fine-grained soils are assumed to be the continuous phase and coarse grains such as sand particles are suspended within the paste and far from each other. The proposed relationship is shown in Table 4.1. For wet mixtures, an empirical relationship similar to the geometric mean of the thermal conductivity of all components (solids, water and air) is shown in Table 4.1.

4.3. EXPERIMENTAL STUDY: MATERIALS, DEVICES AND PROCEDURES

Eleven binary mixtures of silica sand and silica flour are tested under dry and water-saturated conditions at varying vertical effective stress levels and zero lateral strain boundary conditions. An additional set of tests is conducted on mixtures saturated with a thermally conductive grease. The properties of the chosen aggregates and fluids are summarized in Tables 4.2 and 4.3. Table 4.4 shows the proportions and properties of the tested mixtures.

Table 4.2. Selected properties of tested aggregates.

Aggregate	Size Range [μm]	D_{50} [mm]	Specific Gravity G_s	Mineralogy (fraction by weight)
Silica Sand 40-45	355 < D < 400	0.38	2.65	SiO_2: 0.998 Fe_2O_3: 1.6×10^{-4} Al_2O_3: 3.4×10^{-4} TiO_2: 0.7×10^{-4} CaO: 1.1×10^{-4} MgO: 0.7×10^{-4}
Silica Sand 45-60	250 < D < 355	0.30	2.65	The same as Sand 40-45
Silica Sand 60-70	210 < D < 250	0.23	2.65	The same as Sand 40-45
Silica Flour (Sil-co-Sil 106)	15 < D < 25	0.02	2.65	SiO_2: 0.998 Fe_2O_3: 3.5×10^{-4} Al_2O_3: 5.0×10^{-4} TiO_2: 2.0×10^{-4} CaO: 1.0×10^{-4} K_2O: 2.0×10^{-4} MgO: $< 1.0\times10^{-4}$ Na_2O: $< 1.0\times10^{-4}$

Table 4.3. Selected properties of pore fluids at room temperature and atmospheric pressure.

Fluids	Thermal Conductivity k [$W.m^{-1}.K^{-1}$]	Mass Density ρ [$kg.m^{-3}$]	Viscosity μ [Pa.s]
Air	0.024	1.205	1.82×10^{-5}
Water	0.609	997 – 998.2	1×10^{-3}
Thermal grease	1.102	2428	70**

** Viscosity of toothpaste.

Table 4.4. Selected properties of tested specimens.

Saturating Pore Fluid	Silica Sand	Specimen No.	Gravimetric Fraction of Silica Flour	Initial void ratio e_o	Dry Mass Density ρ^*		Thermal Conductivity k^*		Coefficient of Compressibility C_c
					ρ_{100} [kg.m^{-3}]	χ [%]	k_{100} [W.m^{-1}.K^{-1}]	β [%]	
Air	60-70	1-1	0	0.593	1672.8	0.18	0.26	20.5	0.0080
	40-45	1-2	0	0.556	1714.3	0.16	0.27	19.9	0.0080
	45-60	1-3	0	0.589	1692.7	0.17	0.28	14.6	0.0080
	45-60	2	0.1	0.469	1829.6	0.48	0.31	16.3	0.0184
	45-60	3	0.2	0.360	1980.8	0.66	0.40	14.2	0.0174
	45-60	4	0.3	0.375	2009.3	0.42	0.46	13.9	0.0364
	45-60	5	0.4	0.391	1986.3	0.48	0.50	17.3	0.0360
	45-60	6	0.5	0.463	1915.3	0.49	0.47	22.2	0.0527
	45-60	7	0.6	0.577	1822.9	0.48	0.43	21.8	0.0737
	45-60	8	0.7	0.578	1789.3	0.70	0.40	14.5	0.0694
	45-60	9	0.8	0.648	1696.9	0.75	0.34	20.5	0.0736
	45-60	10	0.9	0.760	1630.0	0.80	0.32	18.3	0.0854
	45-60	11	1	0.768	1574.7	0.75	0.26	15.4	0.0989
Water	45-60	1	0	0.645	1673.7	0.96	2.71	18.9	0.0386
	45-60	2	0.1	0.504	1860.5	1.21	2.90	14.1	0.0536
	45-60	3	0.2	0.305	1927.7	0.82	3.07	16.0	0.0362
	45-60	4	0.3	0.341	2012.9	1.29	3.24	15.9	0.0475
	45-60	5	0.4	0.373	2013.1	0.79	3.41	19.2	0.0421
	45-60	6	0.5	0.401	1989.6	0.87	3.26	13.7	0.0419
	45-60	7	0.6	0.479	1890.9	1.10	3.14	5.9	0.0482
	45-60	8	0.7	0.659	1747.2	0.91	2.91	4.6	0.0484
	45-60	9	0.8	0.676	1653.2	1.01	2.87	4.7	0.0429
	45-60	10	0.9	0.786	1524.5	1.15	2.72	3.6	0.0427
	45-60	11	1	0.805	1590.2	0.96	2.19	14.1	0.0703
Thermal grease	45-60	1	0	0.68	-	-	2.60	5.9	-
	45-60	2	0.5	1.17	-	-	2.49	5.5	-
	45-60	3	1	1.72	-	-	1.77	1.7	-

* Values are reported for the unloading trend.

Tests are conducted inside a k_o oedometer chamber. The inner wall of the chamber is coated using petroleum gel and covered by a polymer wrap to decrease the effect of wall friction and improve stress distribution. Dry mixtures are scooped in 0.5 cm thick layers and then tapped 50 times per layer using a 100 g rod to obtain a relatively dense specimen. Water-saturated mixtures are first mixed dry, then saturated and scooped into the chamber filled with water and allowed to settle for 5 minutes. Then each layer is tapped 50 times using the same rod.

The vertical stress is varied in 6 steps from σ'_o=41 kPa to σ'_u=2.6 MPa by doubling the load in each successive stage. Vertical deformation and effective thermal conductivity are measured at all loading and unloading steps using an LVDT and a thermal needle probe.

The thermal conductivity is measured after a 10 minute equilibration period following each loading or unloading step. The thermal needle probe used in this study consists of a heating wire (electrical resistance R = 66.6 Ω) and a type E thermocouple (methodology described in Bullard et al., 1956). The heating wire is connected to a ΔV = 2 V DC source for 120 seconds and the thermocouple measures the evolution of temperature versus time during heating and cooling stages. A 40 minute cooling time is allowed after each measurement (details in Chapter 3). The thermal needle probe is calibrated using agar-stabilized water (ASTM D5334).

A typical temperature-time signature is shown in Figure 4.1.a for a dry specimen with FC=0.7 fines content.

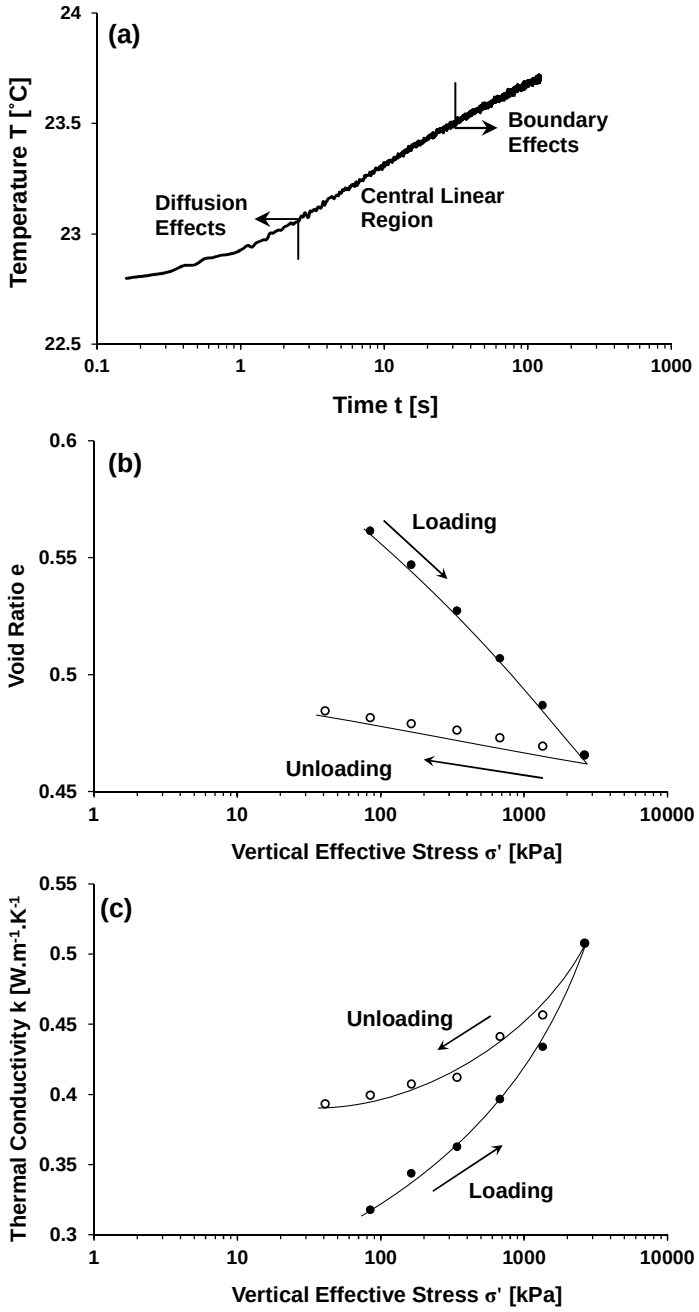

Figure 4.1. Typical dataset. (a) Temperature versus time signature (σ'_z = 341 kPa), (b) Stress-dependent void ratio, and (c) Stress-dependent thermal conductivity during loading and unloading. Case: dry mixture with fines content FC=0.7.

The thermal conductivity k [$W.m^{-1}.K^{-1}$] is calculated from the slope of the temperature versus the logarithm of time curve (taken from the central linear region) and the imposed heat per unit length L [m] of the heating wire $Q = V^2/(R.L)$ [$W.m^{-1}$] (Van Der Held et al., 1953; De Vries and Peck, 1958; Von Herzen and Maxwell, 1959):

$$k = \frac{Q}{4\pi} \frac{\log(t_2/t_1)}{T_2 - T_1} \tag{4.4}$$

The needle probe is placed along the centerline of a cylindrical specimen. The central region of log(t)-T signatures ranges between 120 s and 1 ˚C. Finite difference simulations of radial heat diffusion are conducted to verify boundary conditions. Results confirm that the diameter of the specimen is sufficiently large and the duration of heating is sufficiently short so that the slope in the central region is not affected by boundaries: the heat front reaches the outer boundary 3.5 cm away from the heat source in about 500 s.

Typical results shown in Figure 4.1 indicate that void ratio decreases and thermal conductivity increases with stress and there is a residual response upon unloading (Figure 4.1.b and c) apparently due to permanent fabric and contact changes, and locked-in horizontal stress. The complete dataset is presented next.

4.4. EXPERIMENTAL RESULTS

The evolution of dry mass density, coefficient of compressibility, and thermal conductivity with vertical effective stress and mixture composition is shown in Figures 4.2 through 4.8 for all specimens. Salient observations follow.

- The thermal conductivity of 100% silica sand specimens with different particle mean sizes (D_{50}: 0.23, 0.30 and 0.38 mm) increases slightly with D_{50} and it is

higher than that of silica flour (D_{50}=0.02 mm) as it is shown in Figure 4.2. Note that all four specimens have the same mineralogy (Table 4.2).

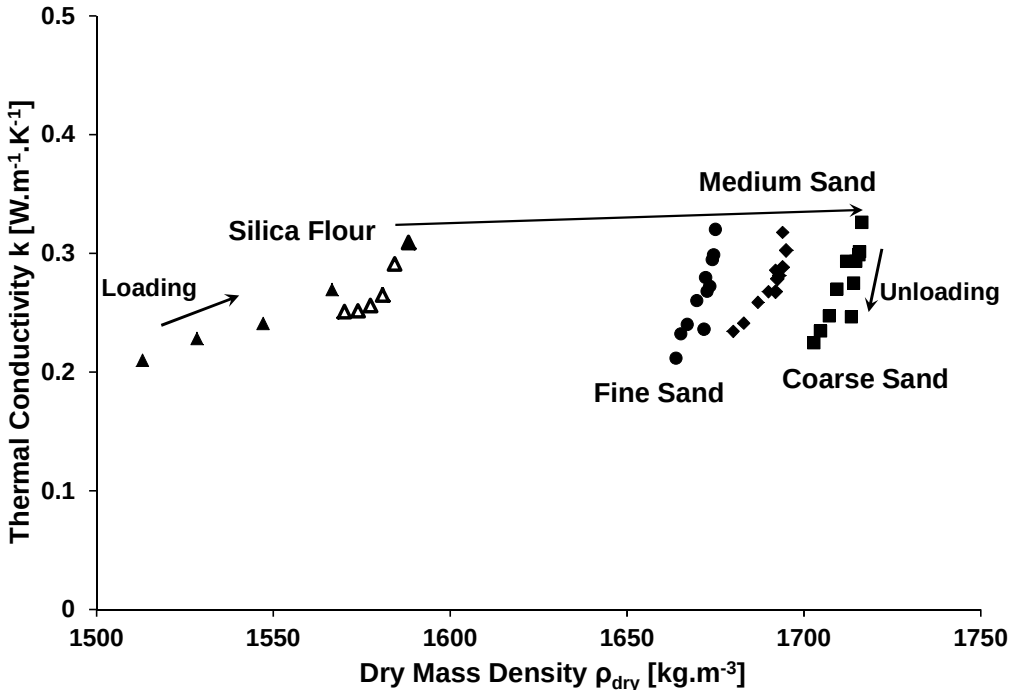

Figure 4.2. Thermal conductivity versus dry mass density for dry mono-sized sand and silt (refer to Tables 4.2 and 4.4).

- The initial dry mass density is very similar for air-dry and water-saturated mixtures with the same fines content (Figure 4.3 – Note: some dry mixtures are initially denser). Density increases with effective stress and exhibits very limited rebound upon unloading. Maximum density is reached by mixture with a fines content FC~30%.

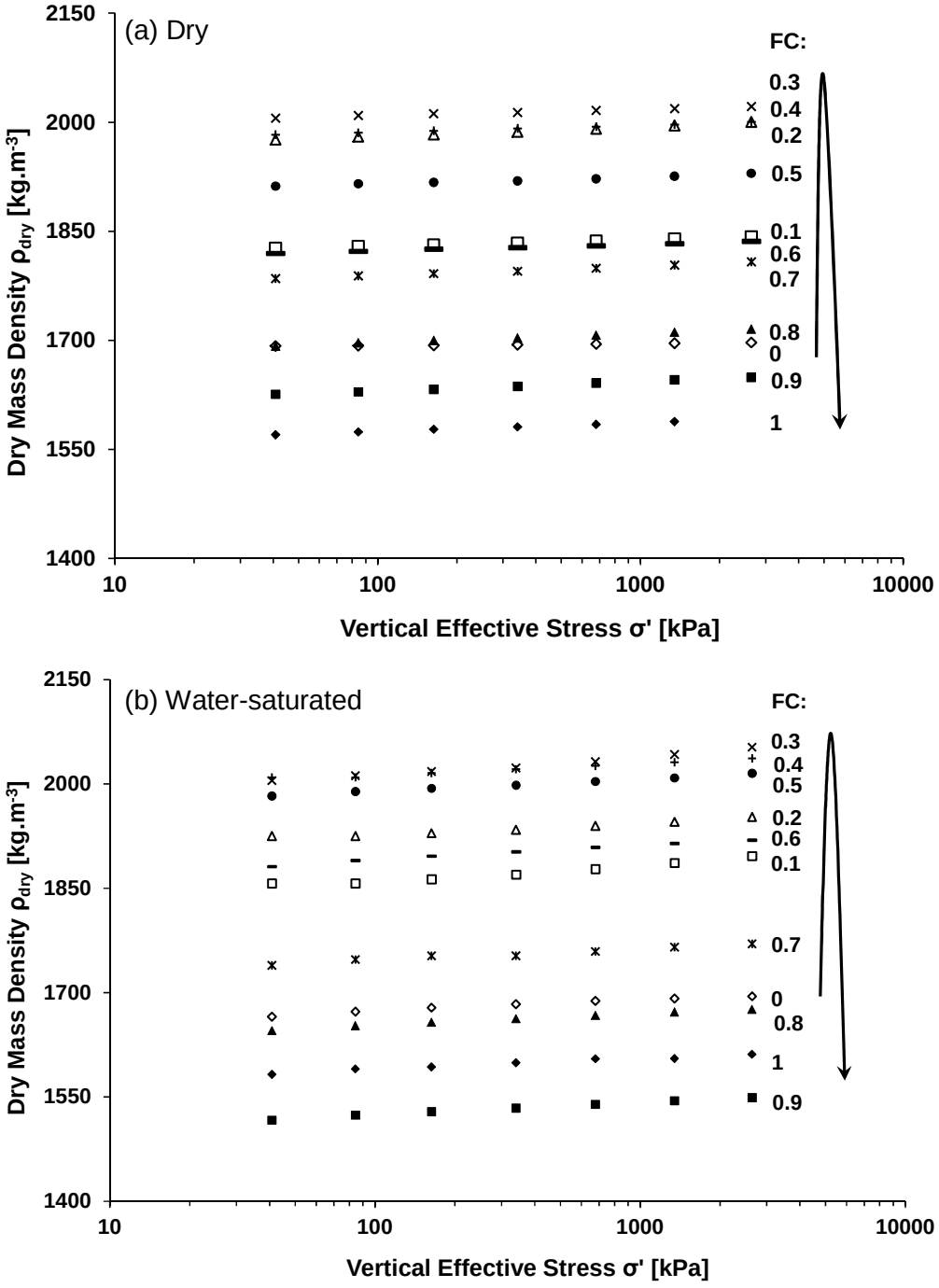

Figure 4.3. Dry mass density versus vertical effective stress – data shown during unloading only for clarity. (a) Dry specimens. (b) Water-saturated specimens.

- The thermal conductivity of water-saturated specimens is about one order of magnitude higher than that of dry specimens with the same fines content (Figure 4.4).

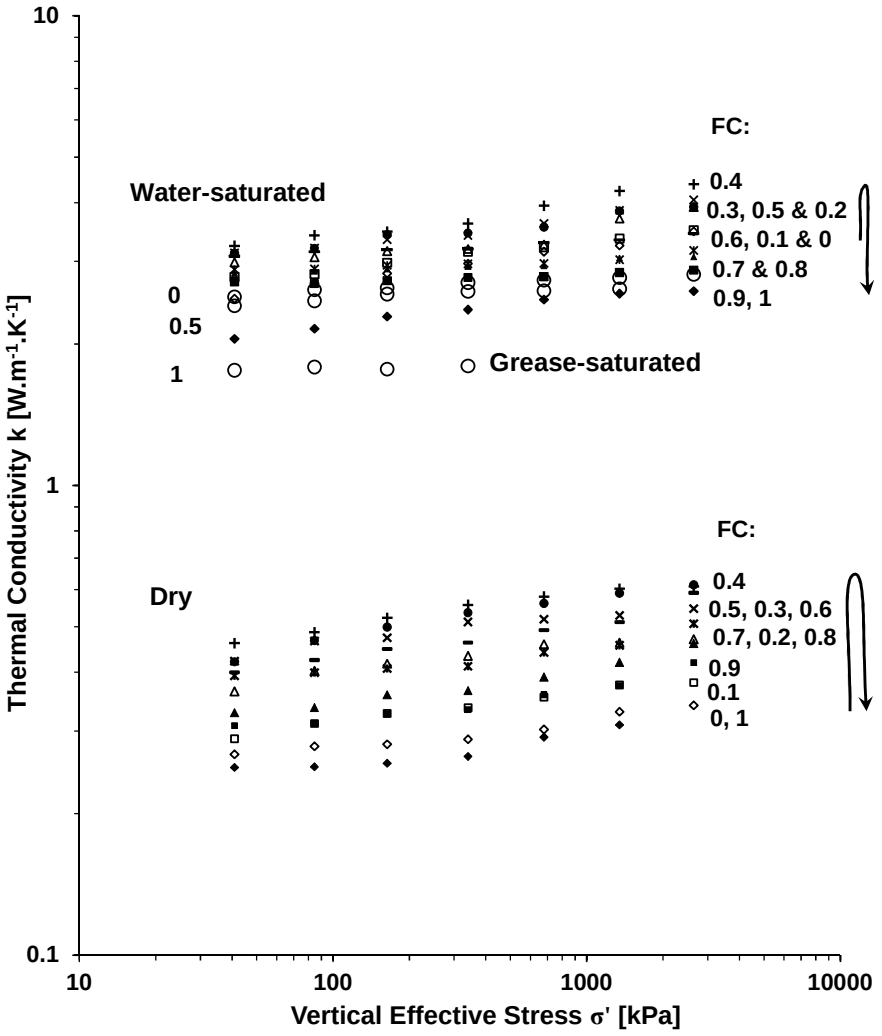

Figure 4.4. Thermal conductivity versus vertical effective stress for all mixtures – data shown during unloading only for clarity (details in Table 4.4).

- The thermal conductivity of thermal grease-saturated mixtures is lower than that of water-saturated specimens although the thermal conductivity of grease is twice that of water (Figure 4.4 and Table 4.3).

- Thermal conductivity versus dry mass density curves for all dry and water-saturated mixtures show that the thermal conductivity increases above all with saturation, some with stress, and non-sequentially with fines content (Figure 4.5 – only unloading data shown for clarity).

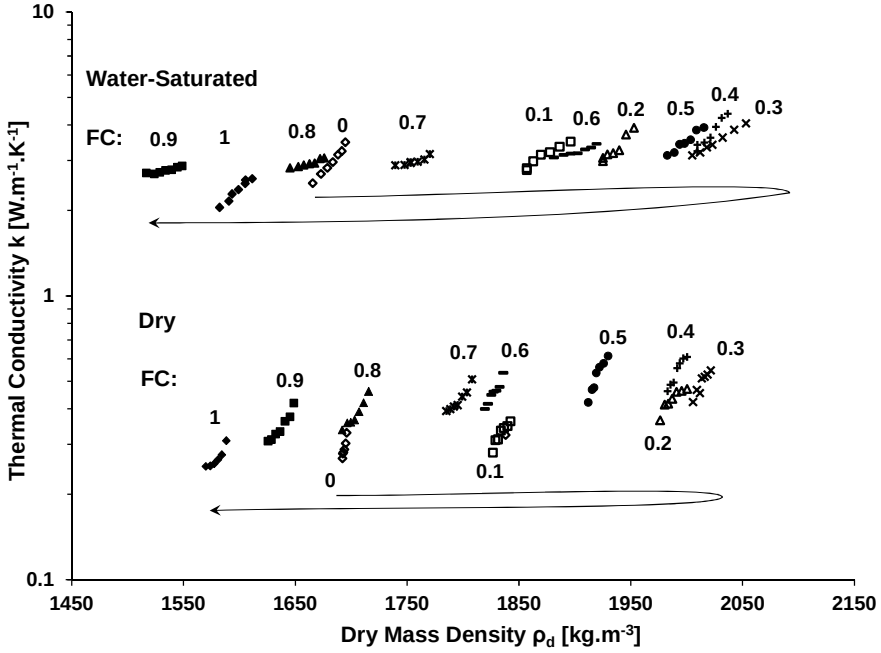

Figure 4.5. Thermal conductivity versus dry mass density for all dry and water-saturated binary mixtures – data shown for unloading only (details in Table 4.4).

- The dry mass density of dry and water-saturated mixtures at the initial load (σ'_o=41 kPa), under the ultimate load (σ'_u=2.6 MPa; for fines content FC=1: σ'_u=1.3 MPa), and under the final load upon unloading (σ'_f=41 kPa) are shown in Figure 4.6. Mixtures made of fines content FC=0.3 to 0.4 exhibit the highest density both when dry and water-saturated (Table 4.4).
- The thermal conductivity of dry and water-saturated mixtures at the initial, ultimate and final loads are shown in Figure 4.7. Dry specimens exhibit the

highest thermal conductivity when the fines content is FC≈0.5; however, a lower values of fines content is apparent for the peak thermal conductivity in water-saturated mixtures.

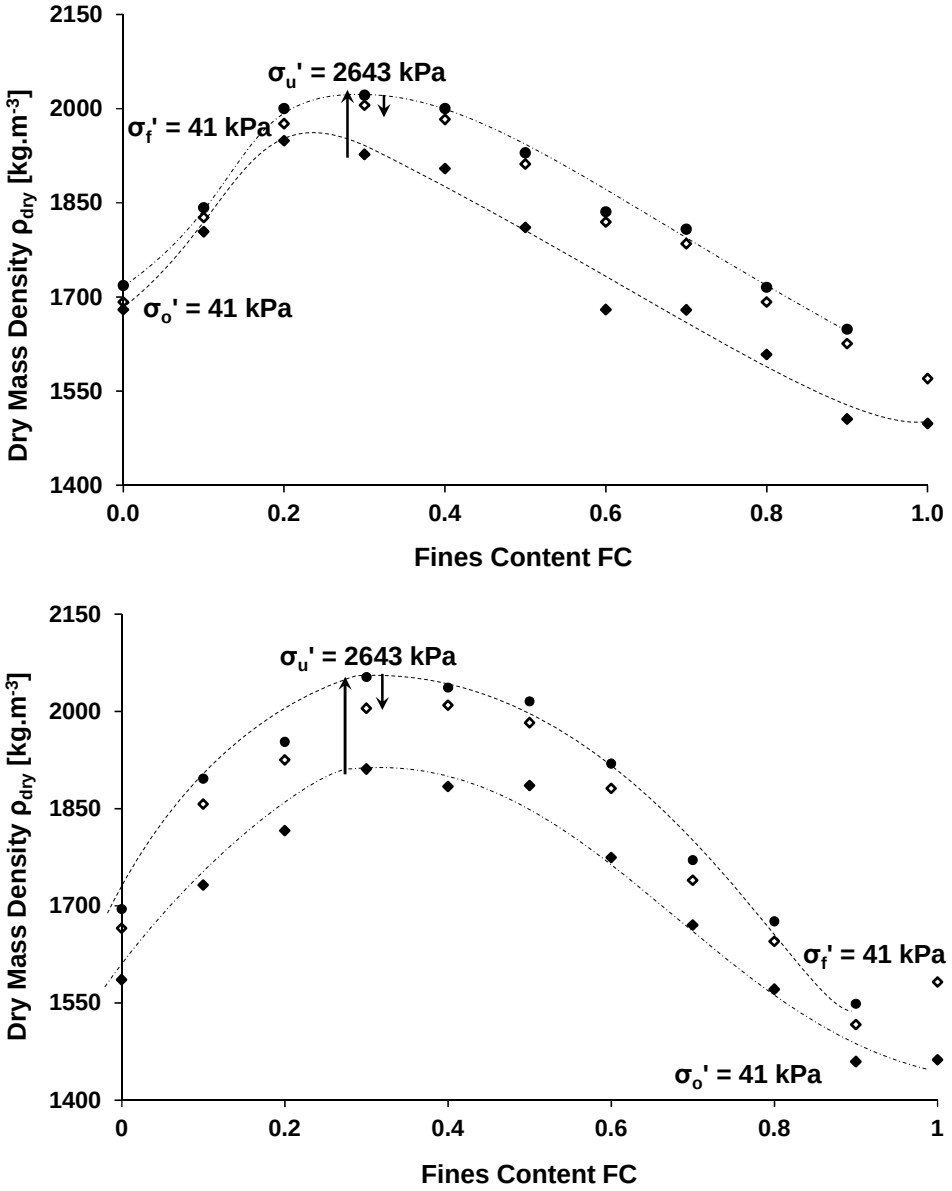

Figure 4.6. Evolution of dry mass density during loading and unloading for different mixtures - initial state (♦ σ'_{zo}=41 kPa), peak load (● σ'_{zu}=2643 kPa), back to the first load (◊ σ'_{zf}=41 kPa). (a) dry specimens. (b) water-saturated specimens.

- The sediment compression index $C_c=\Delta e/\log(\sigma'_H/\sigma'_L)$, i.e., the reduction in void ratio with vertical effective stress, is reported in Figure 4.8 for all wet and dry mixtures (see also Table 4.4). The compressibility of mixtures increases with fines content; however, the effect of fines content is more pronounced on the compressibility of dry mixtures: while coarser mixtures with low fines content are more compressible when wet, mixtures with high fines content FC > 0.4 are more compressible when dry.

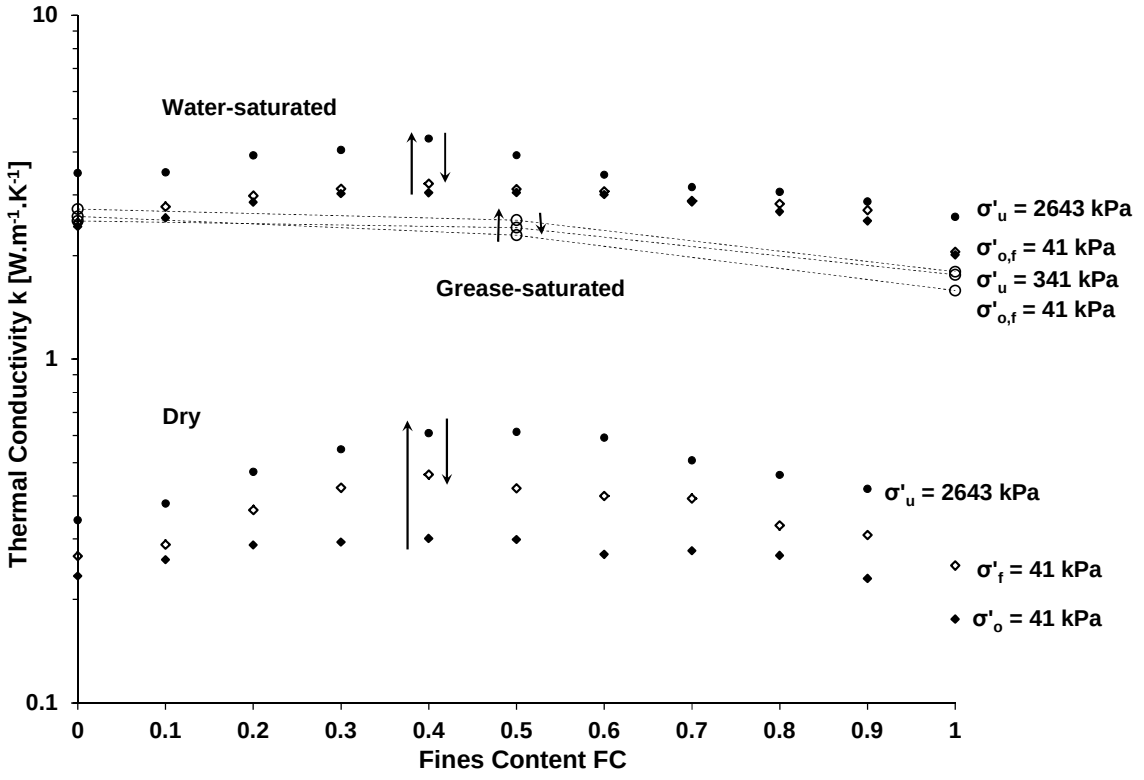

Figure 4.7. Evolution of thermal conductivity during loading and unloading for different mixtures – initial state (♦ σ'_{zo}=41 kPa), peak load (● σ'_{zu}=2643 kPa for dry and water-saturated specimens and σ'_{zu}=341 kPa for grease-saturated specimens), back to the first load (◊ σ'_{zf}=41 kPa).

Dry and water-saturated mixtures with fines content FC≈0.4 show the highest increase in thermal conductivity with a tenfold increase in effective stress (Table 4.4). On the contrary, the thermal conductivity is lowest and least affected by vertical effective stress for the two mono-size specimens (FC=0 and FC=1).

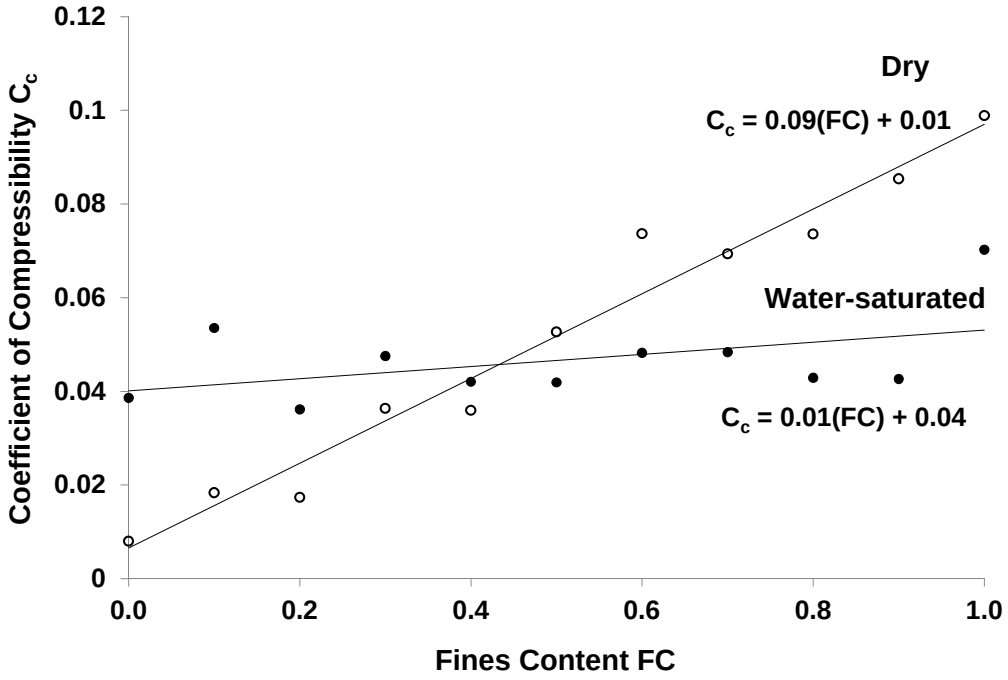

Figure 4.8. Coefficient of compressibility computed between σ'_z = 340 kPa and σ'_z = 2.6 MPa for all dry and water-saturated mixtures.

4.5. ANALYSES AND DISCUSSION

Linear trends of dry mass density and thermal conductivity versus the logarithm of stress can be fitted as follows (unloading data):

$$\rho_{dry} = \rho_{100}\left[1 + \chi \log\left(\sigma'/100\ \text{kPa}\right)\right] \tag{4.5}$$

$$k_{dry/sat} = k_{100}\left[1 + \beta \log\left(\sigma'/100\ \text{kPa}\right)\right] \tag{4.6}$$

where ρ_{100} [kg.m^{-3}] and k_{100} [W.m^{-1}.K^{-1}] are the dry mass density and the thermal conductivity at a vertical stress σ'_z = 100 kPa. The dimensionless factors χ and β capture the increase in dry mass density and thermal conductivity from σ'=2.6 MPa to σ'=41 kPa. Fitted values are summarized in Table 4.4 for all dry and water-saturated mixtures. Data gathered in unloading were selected because they are free from sitting effects and particle rearrangements that prevail during loading. Dry mass density parameters are not reported for grease-saturated specimens because part of the paste-like specimen "leaked out" of the cell during loading.

Equations 4.5 and 4.6 are combined to obtain a single equation for the mixture thermal conductivity k [W.m^{-1}.K^{-1}] as a function of dry mass density ρ_{dry} [kg.m^{-3}] at any effective stress level:

$$k = \frac{\beta k_{100}}{\chi \rho_{100}} (\rho_{dry} - \rho_{100}) + k_{100} \qquad (4.7)$$

Thermal conductivity values predicted using Equation 4.7 are plotted versus measured thermal conductivities in Figure 4.9. This is a highly constrained model – hence its ability to "predict values." Yet, this analysis highlights the link between density, stress and saturation on thermal conductivity.

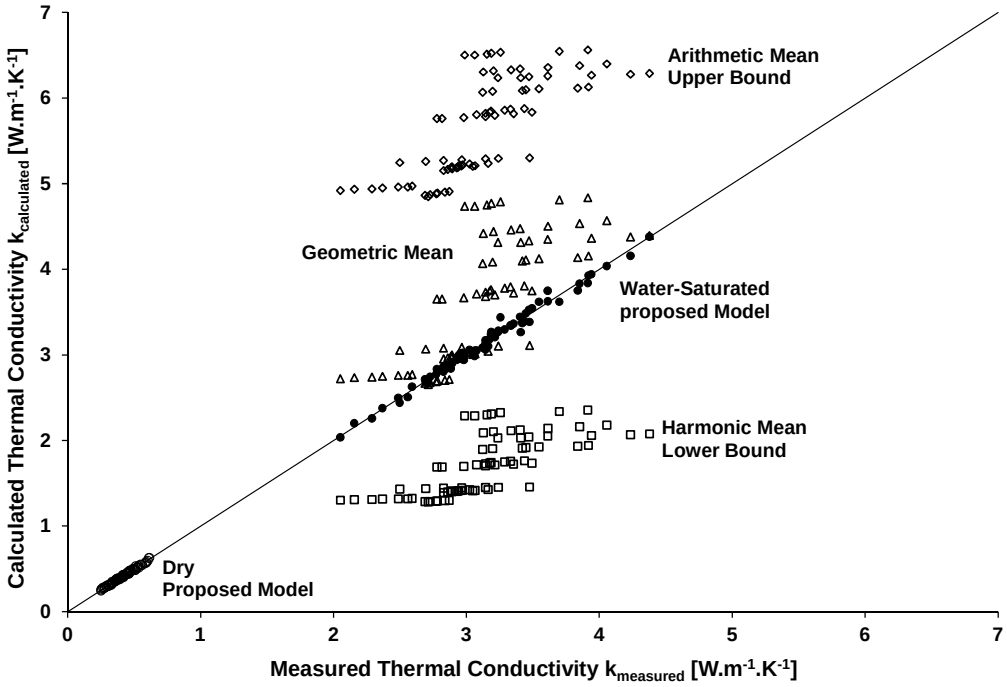

Figure 4.9. Measured versus predicted (Equation 4.7) thermal conductivity values for all dry and water-saturated mixtures.

Residual Effects

The thermal conductivity and dry mass density of all mixtures exhibit residual effects during unloading (Figures 4.6 and 4.7) due to irreversible grain-scale processes upon loading, which include: particle rearrangement, particle plastic deformation at contacts, and locked-in horizontal stress.

Fines Content: Transitional Mixtures

Density. Consider a coarse-grained medium with void ratio e_c and a fine-grained medium with void ratio e_f, both made of a mineral with the same specific gravity. The gravimetric fines content FC when the fine particles fill the pores in a coarse aggregate skeleton can be computed from gravimetric/volumetric relations to obtain (Santamarina, 2014):

$$FC = \frac{m_f}{m_f + m_c} = \frac{e_c}{e_c + e_f + 1} \quad (4.8)$$

The following two transitional extremes can be considered: (1) coarse grains at maximum void ratio $e_c=e^c_{max}$ and the fine at minimum void ratio $e_f=e^f_{min}$, and (2) coarse grains at $e_c=e^c_{min}$ while the fine is at $e_f=e^f_{max}$. For silt and sand mixtures, Equation 4.8 predicts the transitional fines content between FC=0.25 to 0.35. These values agree with trends in Figure 4.5.

Compressibility. The compressibility of mixtures increases significantly with fines content in both dry and water-saturated mixtures. This indicates that while fines may not fill pores, they do coat coarse grains and favor densification. Subcritical crack propagation at the contact between solid grains increases with inter-particle stress and in the presence of water (Oldecop and Alonso, 2001). This explains the left hand side of Figure 4.8 (FC < 0.4), in which the compressibility of water-saturated mixtures is higher than that of dry ones.

Thermal Conductivity. While the fines content to attain the highest density is FC≈0.3, the highest thermal conductivity is exhibited by mixtures with FC=0.4-0.5 (Figure 4.5).

Transitional mixtures. The data show that the fines content during the coarse-dominant to fines-dominant varies for the different properties.

Liquid-Saturation

Water. The presence of water in pores exerts a strong effect on the thermal conductivity of the medium (Figure 4.4). Water fills pores and conducts heat between particles. Water also reduces the thermal contact resistance by filling spaces at inter-particle contacts. Heat conductance in fluids is based on molecular motion and collisions.

The probability of molecular collisions is much lower in gases than liquids; hence, the thermal conductivity of water is about 25 times higher than that of air (Table 4.3). Thermal resistance at interfaces is also due to the different conduction processes in liquids and solids.

Thermal conductivity data for water-saturated specimens is compared against model predictions in Figure 4.10. The geometric mean is a better prediction than the harmonic (series configuration of solid and fluid components with respect to heat flow – lower bound) and arithmetic mean (parallel configuration of solid and fluid components with respect to heat flow – upper bound). Overall, these models fail to capture the role of the stress-dependent granular skeleton.

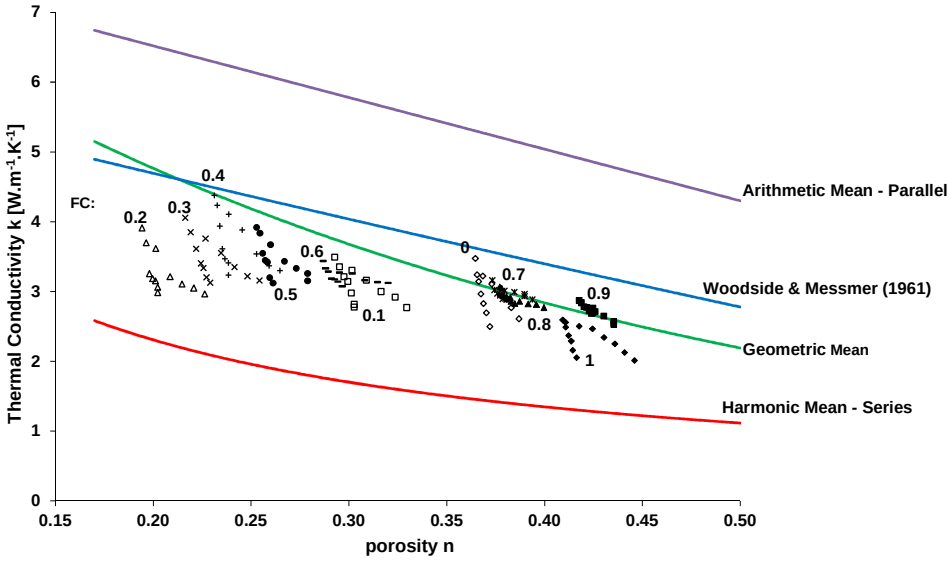

Figure 4.10. Thermal conductivity of binary mixtures gathered during loading and unloading (Table 4.4) compared against common models for water-saturated specimens (Table 4.1).

Thermal Grease. The thermal conductivity of thermal grease-saturated mixtures is lower than that of water-saturated mixtures even though the thermal conductivity of the

grease used in this study is twice the thermal conductivity of water. In part, this is due to the very high viscosity of the grease (about 5 orders of magnitude higher than that of water). Figure 4.11 shows a physical illustration to analyze the efficiency of heat transfer at inter-particle contacts in dry, water- and grease-saturated conditions. The high viscosity of the thermal grease prevents it from filling grain surface imperfections and prevents the initial dense packing of particles (Note: the initial consistency of the mixture was gel-like rather than granular). The very low value of β-factor for grease-saturated mixtures (Equation 4.6; Table 4.4) indicates that increase in stress does not improve the mixture thermal conductivity.

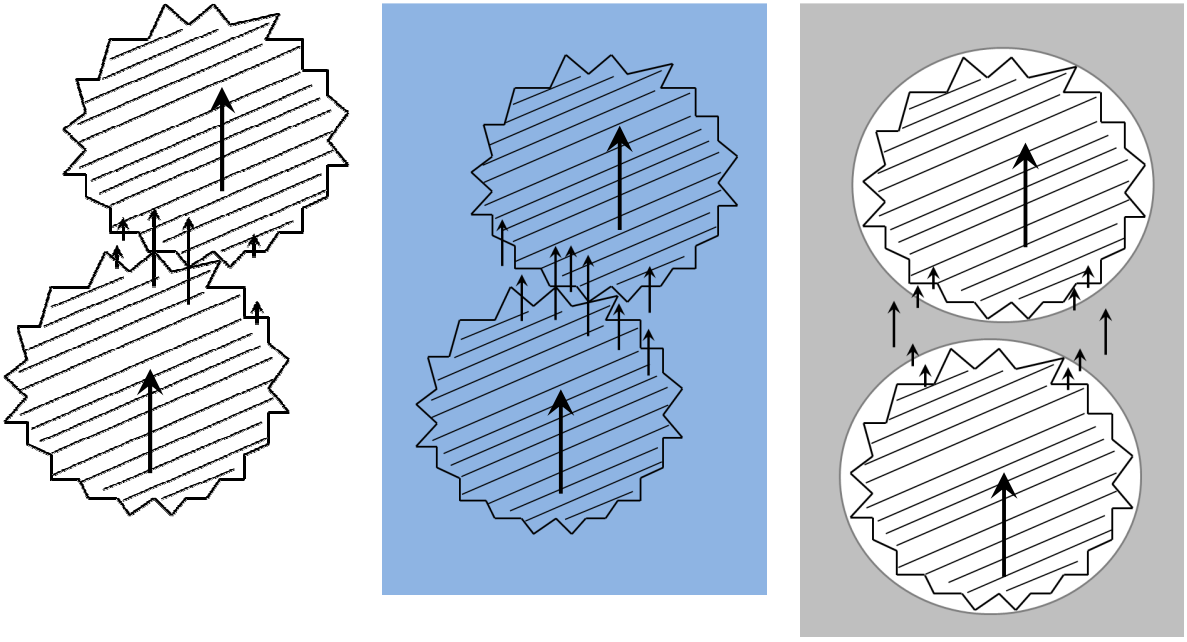

(a) (b) (c)

Figure 4.11. Grain-scale analysis of the effect of selected pore fluids on heat transfer: (a) Dry, (b) Water-saturated, and (c) Grease-saturated granular media – White: air. Hatched: solid grains. Solid: water or grease. Arrows drawn in the direction of heat flow; their relative length suggest efficiency of heat transfer.

4.6. CONCLUSIONS

- The thermal conductivity increases with increasing particle size in mono-sized grain packings because the radius of inter-particle contacts increases with particle size.
- The thermal conductivity of all dry and water-saturated mixtures increases with vertical effective stress as the inter-particle contact area and coordination number increases.
- The thermal conductivity of the saturating fluid strongly affects the effective thermal conductivity of the medium. In particular, the thermal conductivity of water-saturated specimens is about one order of magnitude higher than that of the same mixture in dry conditions.
- Other physical properties of the pore-filling liquid may hinder the beneficial effect of the liquid. In particular, high viscosity may prevent filling the grain surface imperfections and prevent particle rearrangement.
- The presence of fines changes the behavior of mixtures. The maximum density is attained when the fines content is FC=0.25-0.35; this corresponds to compressibility increase monotonically with increasing fines content, and specimen made of 100% fines has the highest compressibility in both dry and water-saturated specimens; this reflects that the ratio of void space to solid grains is higher in fine-grained materials so that they show higher stress-sensitivity upon closure of voids by increasing stress.
- Thermal conductivity is highest in mixtures with FC=0.4; this higher value reflects that inter-particle coordination number continues increasing even after all the pores between coarse grains are filled by the fine, providing higher number of heat pathways and higher thermal conductivity.

- Both thermal conductivity and dry mass density are higher during unloading compared to loading at all vertical stress levels. This is due to irreversible deformations of inter-particle contacts, residual fabric changes and locked-in horizontal stress.
- Water saturation enhances the effective thermal conductivity much more effectively than particle surface treatment (tested in chapter 3). For high temperature applications, alternative liquids must be identified to avoid phase transition.

4.7. REFERENCES

Abyzov, A. M., Goryunov, A. V., and Shakhov, F. M. (2014). "Effective Thermal Conductivity of Disperse Materials. II. Effect of External Load." International Journal of Heat and Mass Transfer, 70, 1121-1136.

Beck, A. E. (1976). "Improved Method of Computing the Thermal Conductivity of Fluid-Filled Sedimentary Rocks." Log Analyst, 17(6), 30-38.

Becker, B. R., Misra, A., and Fricke, B. A. (1992). "Development of Correlations for Soil Thermal Conductivity." International Communications in Heat and Mass Transfer, 19(1), 59-68.

Bullard, E. C., Maxwell, A. E., and Revelle, R. (1956). "Heat Flow through the Deep Sea Floor." Advances in Geophysics, 3, 153-181.

Chari, V. D., Sharma, D. V. S. G. K., Prasad, P. S. R., and Murthy, S. R. (2013). "Dependence of Thermal Conductivity in Micro to Nano Silica." Bulletin of Materials Science, 36(4), 517-520.

Cho, G. C., Dodds, J., and Santamarina, J. C. (2006). "Particle Shape Effects on Packing Density, Stiffness, and Strength: Natural and Crushed Sands." Journal of Geotechnical and Geoenvironmental Engineering, 132(5), 591-602.

Cho, W. J., Lee, J. O., and Kwon, S. (2011). "An Empirical Model for the Thermal Conductivity of Compacted Bentonite and a Bentonite-Sand Mixture." Heat and Mass Transfer, 47(11), 1385-1393.

De Vries, D. A., and Peck, A. J. (1958). "On the Cylindrical Method of Measuring Thermal Conductivity with Special Reference to Soils." CSIRO, Division of Plant Industry, 11, 16.

Fricke, H. (1924). "A Mathematical Treatment of the Electric Conductivity and Capacity of Disperse Systems I. The Electric Conductivity of a Suspension of Homogeneous Spheroids." Physical Review, 24(5), 575-587.

German, R. M. (1989). Particle Packing Characteristics, Princeton, N.J. : Metal Powder Industries Federation, c1989.

Horai, K. (1971). "Thermal Conductivity of Rock-Forming Minerals." Journal of Geophysical Research, 76(5), 1278-1308.

Johansen, T. A. (1975). "Thermal Conductivity of Soils." US Army Corps of Engineers, Trondheim, Hanover, New Hampshire.

Knutsson, S. (1983). "On the Thermal Conductivity and Thermal Diffusivity of Highly Compacted Bentonite." Swedish Nuclear Fuel Supply Co/Division KBS, Lulea, Sweden, 55.

Lambert, M. A., and Fletcher, L. S. (1997). "Review of Models for Thermal Contact Conductance of Metals." Journal of Thermophysics and Heat Transfer, 11(2), 129-140.

Oldecop, L. A., and Alonso, E. E. (2001). "A Model for Rockfill Compressibility." Geotechnique, 51(2), 127-139.

Ould-Lahoucine, C., Sakashita, H., and Kumada, T. (2002). "Measurement of Thermal Conductivity of Buffer Materials and Evaluation of Existing Correlations Predicting It." Nuclear Engineering and Design, 216(1-3), 1-11.

Paek, J. W., Kang, B. H., Kim, S. Y., and Hyun, J. M. (2000). "Effective Thermal Conductivity and Permeability of Aluminum Foam Materials." International Journal of Thermophysics, 21(2), 453-464.

Sakashita, H., and Kumada, T. (1998). "Heat Transfer Model for Predicting Thermal Conductivity of Highly Compacted Bentonite." Journal of the Atomic Energy Society of Japan, 40(3), 235-240.

Santamarina, J. C., Klein, K. A., and Fam, M. A. (2001). Soils and Waves - Particulate Materials Behavior, Characterization and Process Monitoring, John Whiley and Sons, LTD.

Sridhar, M. R., and Yovanovich, M. M. (1994). "Review of Elastic and Plastic Contact Conductance Models - Comparison with Experiment." Journal of Thermophysics and Heat Transfer, 8(4), 633-640.

Tang, A.-M., Cui, Y.-J., and Le, T.-T. (2008). "A Study on the Thermal Conductivity of Compacted Bentonites." Applied Clay Science, 41(3–4), 181-189.

Tehranian, F., Abdou, M. A., and Tillack, M. S. (1994). "Effect of External-Pressure on Particle Bed Effective Thermal-Conductivity." Journal of Nuclear Materials, 212, 885-890.

Van Der Held, E. F. M., Hardebol, J., and Kalshoven, J. (1953). "On the Measurement of the Thermal Conductivity of Liquids by a Non-Stationary Method." Physica, 19, 203-216.

Vargas, W. L., and McCarthy, J. J. (2002). "Stress Effects on the Conductivity of Particulate Beds." Chemical Engineering Science, 57(15), 3119-3131.

Von Herzen, R., and Maxwell, A. E. (1959). "The Measurement of Thermal Conductivity of Deep-Sea Sediments by a Needle Probe Method." Journal of Geophysical Research, 64(10), 1557-1563.

Weidenfeld, G., Weiss, Y., and Kalman, H. (2004). "A Theoretical Model for Effective Thermal Conductivity (ETC) of Particulate Beds under Compression." Granular Matter, 6(2-3), 121-129.

Woodside, W., and Messmer, J. H. (1961a). "Thermal Conductivity of Porous Media. 1-Unconsolidated Sands." Journal of Applied Physics, 32(9), 1688-1699.

Yun, T. S., and Santamarina, J. C. (2008). "Fundamental Study of Thermal Conduction in Dry Soils." Granular Matter, 10(3), 197-207.

CHAPTER 5

THE EVOLUTION OF COMPRESSIBILITY, STIFFNESS, AND THERMAL CONDUCTIVITY OF OIL SANDS

5.1. INTRODUCTION

The term “viscous oil” refers to hydrocarbons with very high viscosity and high specific gravity such as heavy oil, extra heavy oil and bitumen. The viscosity and specific gravity for viscous oil is compared to that of selected fluids in Table 5.1. The very high viscosity of viscous oil at in-situ temperatures is 1 to 7 orders of magnitude higher than that of water. The world’s largest viscous oil reservoirs are located in Alberta, Canada and the Orinoco belt in Venezuela. Together, these two accumulations equal the world’s largest oil reserves in Saudi Arabia. Over 70% of viscous oil reserves exist in soft sandstone and unconsolidated sand deposits with high porosity, $n > 0.25$ (Shafiei and Dusseault, 2013). On average, viscous oil sands contain 82% natural granular materials, 12% oil, and 4% water (Takamura, 1982; Dusseault, 2001; Meyer and Attanasi, 2003).

The in-situ average intrinsic permeability of oil sands is in the range of 10^{-12} m^2, which is compared to that of silts. The fluid conductivity k_{fl} [$m.s^{-1}$] is proportional to the intrinsic permeability of the formation K [m^2], the fluid unit weight γ [$kN.m^{-3}$] of that fluid and the fluid viscosity η [Pa.s] (Bear, 1979):

$$k_{fl} = \frac{K.\gamma}{\eta} \tag{5.1}$$

The resulting Darcian conductivity for oil sands is very low ($k_{fl} \approx 10^{-9}$ to 10^{-12} $m.s^{-1}$, assuming: γ=1024 $N.m^{-3}$, $K=10^{-12}$ m^2 and η=1-1000 Pa.s – Table 5.2) and conventional advection-driven methods do not work for viscous oil production.

Table 5.1. Properties of selected fluids at room temperature and atmospheric pressure.

Fluid	°API Gravity*	Mass Density ρ [kg.m^{-3}]	Viscosity η [Pa.s]
Air	1.1×10^{6}	1.204	2×10^{-5}
Steam	1.7×10^{6}	0.804	9.9×10^{-4}
Water	10	9810	1×10^{-3}
Light crude oil	> 31.1	< 870	6×10^{-3}
Medium oil	22.3 – 31.1	870 – 920	8×10^{-3}
Heavy oil	10 – 22.3	920 – 1000	0.01 – 0.1
Extra heavy oil (Venezuela)	< 10	> 1000	0.1 – 10
Oil sand (Canada)	< 10	> 1000	$10 – 10^{4}$

Sources: Meyer and deWitt, 1990; Head et al., 2003.

* The specific gravity of liquid petroleum is measured in API degrees (American Petroleum Ins.): $API^{\circ} = \frac{141.5}{G_S} - 131.5$, $G_S = \frac{\gamma}{\gamma_w}$

Various enhanced recovery techniques have been developed to increase the production efficiency, with emphasis on heating, to decrease the viscosity of the oil. Figure 5.1 shows the marked variation of viscosity of several viscous oils with temperature (η decreases about two orders of magnitude for the Hamaca's extra heavy oil with only 40 degrees temperature rise and 5 orders of magnitude for Athabasca's oil sand with 200 degrees temperature rise).

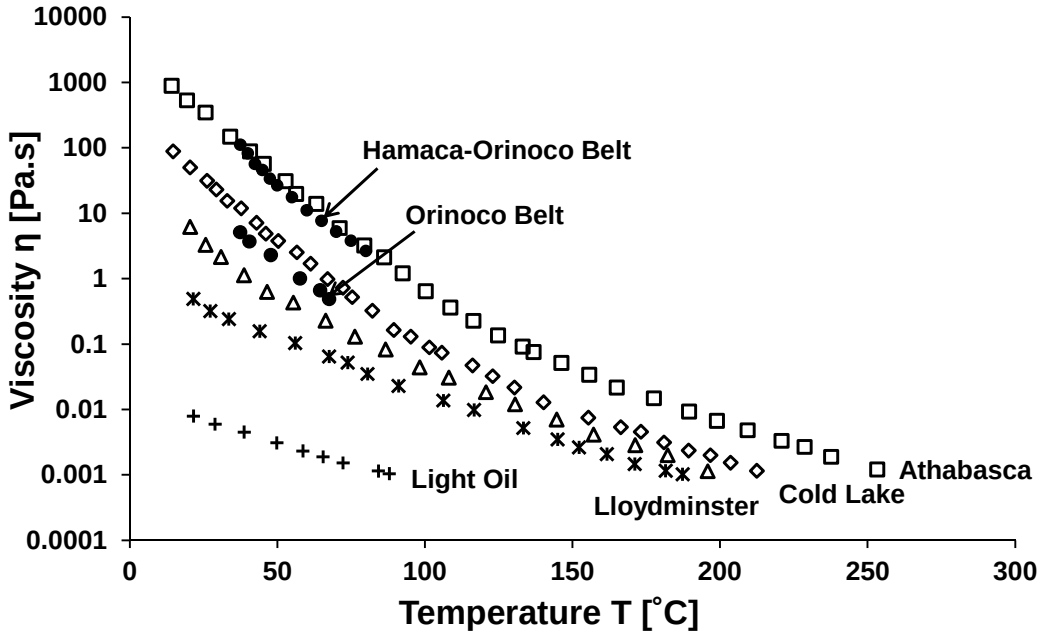

Figure 5.1. Variation of viscosity with temperature – Light to viscous oil. Data from: Raicar and Procter, 1984; Zhao et al., 2013.

The viscosity of heavy oils increases with pressure as shown in Figure 5.2.

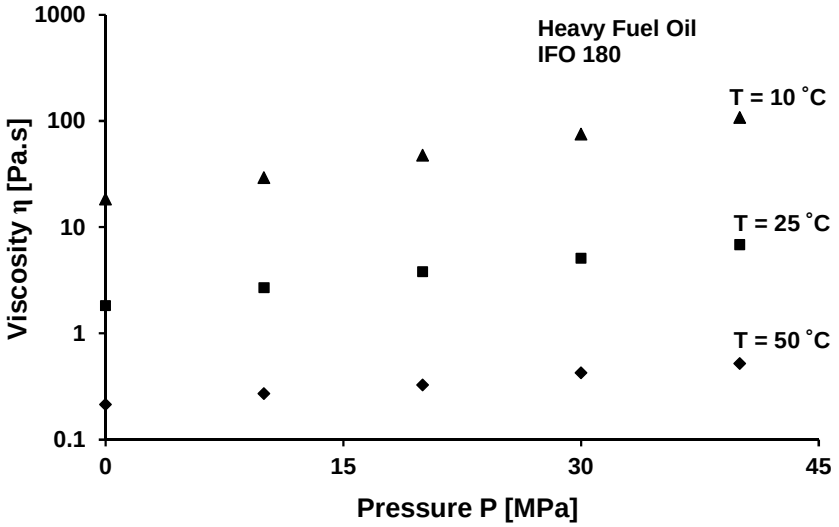

Figure 5.2. Viscosity versus pressure at different temperatures – heavy fuel oil. Data from: Martin-Alfonso et al., 2006.

The oil density also decreases with increasing temperature (Figure 5.3), but its change is limited to only ~50 percent with 100 degrees increase in temperature.

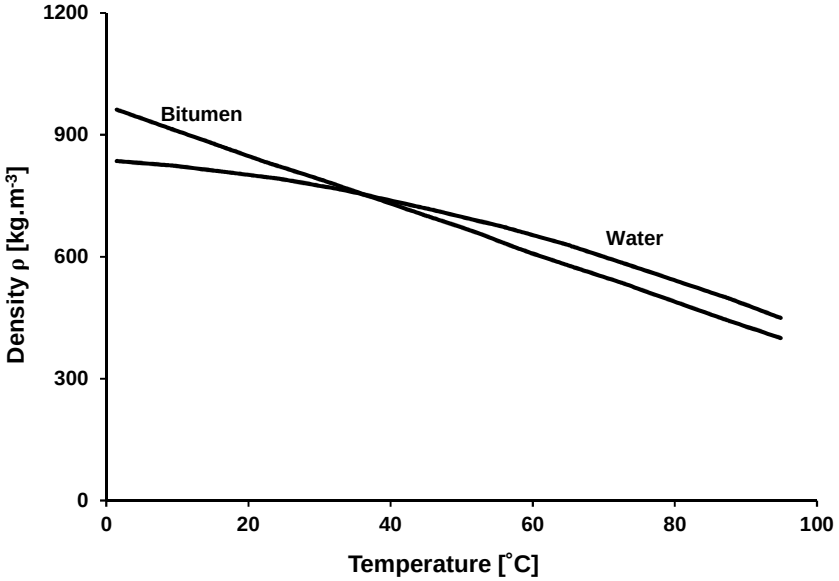

Figure 5.3. Mass density versus temperature – Water and bitumen. Data from: Long et al., 2007.

The thermal conductivity of viscous oil-bearing sands determines the evolution of the heat front, the design of steam injection and the optimum location of production wells in thermally enhanced oil recovery methods (Somerton, 1974; Zimmerman, 1989).

Deposits that contain viscous oil have taken the overburden load for a long geologic time without creep or significant settlement even though the in-situ temperatures (4-50 ˚C) can be higher than both the glass transition and the melting point of the pore-filling oil. Therefore, physical models similar to that of grease-saturated sand specimens (postulated in Chapter 4 – Figure 4.11) cannot be correct. The glass transition point of viscous oils is between -80 and -40 ˚C (Abivin et al., 2012).

This study aims to investigate the effect of oil viscosity on compression index and small-strain stiffness G_{max} [MPa] of viscous oil-bearing sediments and the stress- and temperature-dependency of their thermal conductivity. Underlying processes are postulated and discussed.

5.2. PREVIOUS STUDIES

Formation history. Heavy oils started as lighter oils deeper in the formations (z > 3 km) such as precretaceous shales where the trapped organic matter matured. Light oils migrated to shallower depths (up-dip migration) where they were subjected to weathering processes, such as:

1- Biodegradation (dominant in Canadian oil sands): anaerobes found at lower temperature (T < 80 ˚C) consume the light hydrocarbon molecules, decrease the gas to oil ratio (GOR) and reduce the hydrogen to carbon ratio (Head et al., 2003; Larter et al., 2006). Both processes increase the viscosity and specific gravity of the oil. The relative volume of water-to-oil and the water salinity add second-

order controls on these processes. Conditions vary in the formation so that two orders of magnitude different oil viscosity in vertical (40 m thick) and 2-to-4 times different viscosity in horizontal (1000 m long) directions can be found within the formation (Athabasca's oil sand reservoirs – Larter et al., 2006).

2- Leaching: the lighter hydrocarbon molecules dissolve in the groundwater and migrate to the top of the heavier and more viscous oil reservoir.

3- Source rock immaturity (dominant in Venezuela): immature formations contain heavier oil than thermally mature rocks.

Index, hydraulic, mechanical, and thermal properties of the largest viscous oil formations in the world are summarized in Table 5.2.

Mineralogy. Alberta's oil sand are a mixture of estuarine and marine sedimentary formations (Osacky et al., 2013) and are composed of: quartz, 52-95 %wt.; clay minerals, 0.17-41 %wt.; carbonates, 0.2-7 %wt.; K-feldspar, 2.7-3.9 %wt.; Rulite, TiO_2 - 0-0.7 %wt., and Pyrite, 0-0.2 %wt. (Mercier et al., 2008).

Effects of liquid-saturation. The mid-strain stiffness of a granular medium is required for subsidence estimation and engineering design. The small-strain stiffness of a particulate medium is a constant-fabric parameter that depends on inter-particle contact deformation; it can be readily measured using elastic wave propagation. The elastic P- and S-wave velocities depend on the medium bulk modulus B [Pa], shear modulus G [Pa], and mass density ρ [$kg.m^{-3}$] (Santamarina et al., 2001). Liquid saturation affects the bulk stiffness of a granular medium, but the shear stiffness is independent of liquid saturation and its properties. Equations of the theoretical basis in this field of literature are summarized in Table 5.3.

Table 5.2. Properties of selected viscous oil-bearing formations.

Parameter/Country	**Alberta, Canada**	**Venezuela**
Mass Density ρ [kg/m^3]	1786 – 2550	
Porosity n [ ]	0.23 – 0.42	0.12 – 0.38
Permeability k [m^2]	$(0.01 – 10)\times10^{-12}$	$(2 – 15)\times10^{-12}$
Hydraulic Conductivity K [m/s]	$3.1\times10^{-8} – 5.3\times10^{-10}$	
Oil Content ω_o [ ] (V_{oil}/V_{solid})	0.08 – 0.15 (wt.)	
Degree of Oil Saturation S_o [ ] V_{oil}/V_{void}	0.75 – 0.9	0.76 – 0.9
Water Content ω_w [ ] (V_{water}/V_{solid})	0.014 – 0.032	
Degree of Water Saturation S_w [ ] V_{water}/V_{void}	0.1 – 0.15	0.1-0.29
Dissolved gas	95% CH_4 and 5% CO_2	95% CH_4 and 5% CO_2
Geology: soil/rock type	Uncemented coarse to fine-grained sand deposits, very dense and interlocked structure with concave-convex surfaces and dilative behavior, water-wet, underlined by carbonate and evaporate formations.	Marine and tidal sandstone, Hydrocarbon-wet, underlined by an igneous shield, fine to coarse-grained unconsolidated Miocene Oficina sands. The geologic history of the Orinoco Oil Belt is highly affected by its proximity to the cost.
Fabric	Very dense, interlocked sand, Interlocked contacts with convex-concave curvature. Grains have few tangential contacts Mild diagenetic fabric (pressure dissolution)	Milder diagenetic fabric (subjected to higher temp.), shorter contact lengths and the growth of crystal on the free surfaces towards the pores

Table 5.2.Continued Properties of selected viscous oil-bearing formations.

Parameter/Country	**Alberta, Canada**	**Venezuela**
Presence of water bearing deposit	Some reservoirs have an active water bed, but many do not	Presence of one or two water bearing sand deposits underlying the oil bearing formations is common
Pore water ionic concentration	20,000-60,000 ppm (20-60 g of salt per liter of water)	20,000-60,000 ppm
Mineralogy	Quartz: 90-98%, Feldespar: 1-5%, Muscovite: 0-3%, Clay minerals: 0-4% Illite, Kaolinite, Vermiculite	More quartzitic and less clayey than Canadian oil sands (more similar to Athabasca)
Mean Grain size D_{50} [mm]	0.1 – 0.4	0.25
Effective Grain Size D_{10} [mm]	0.075 – 0.2	
Fine content [%]	3 – 5%	
Particle Shape	Oblong grains (0.15mm/0.23mm, aspect ratio of 0.65)	Rounded to sub-rounded
Thermal Conductivity k_T [$W.m^{-1}.K^{-1}$]	0.8 – 2.1 (depends on oil saturation and temperature)	
Heat Capacity C_p [$kJ.kg^{-1}.K^{-1}$]	0.718 – 1.23	

Table 5.2.Continued Properties of selected viscous oil-bearing formations.

Parameter/Country	**Alberta, Canada**	**Venezuela**
Thermal volumetric expansion β [K^{-1}]	8×10^{-5}	
Friction angle φ [ ]	29-40 (decreases with temperature rise and increasing degree of saturation of oil!)	
Shear Wave Velocity V_S [km/s]	1.4 (T=10˚C)	
P-wave velocity V_P [km/s]	2.75 (T=10˚C)	2.65
Pressure Diffusion Coefficient C_v [m^2/s]	$(0.38 – 3.6)\times10^{-5}$	
Poisson's Ratio ν [ ]	0.25 – 0.315	

Sources: Glassett and Gould, 1976; Dusseault and Morgenstern, 1978; Dusseault and Scafe, 1979; Linberg, 1980; Mossop, 1980; Cervenan et al., 1981; Karim and Hanafi, 1981; Raisbeck and Currie, 1981; Takamura, 1982; Chapman et al., 1984; Hanafi and Karim, 1986; Agar et al., 1987; Kiser, 1987; Martinez, 1987; Drelich et al., 1996; Samieh and Wong, 1997; Wong, 1999; James, 2000; Puri, 2000; Wong, 2000; Dusseault, 2001; Wong, 2001; Wong and Yeung, 2002; Canada, 2004; Obermajer et al., 2004; Han et al., 2007; Gates et al., 2008; Anochie-Boateng and Tutumluer, 2009.

Table 5.3. Relationships for stiffness of geomaterials with respect to liquid-saturation.

Equation	Parameters	Notes	References
$(B_s)_{upper} = B_m(1-n) + B_\ell.n$	B_s [Pa]: Bulk modulus of the liquid-saturated granular skeleton B_m [Pa]: Mineral bulk modulus B_ℓ [Pa]: Liquid bulk modulus n: Porosity	Reuss' upper bound Series configuration of pore liquid and solid grain with respect to passing P-wave	
$(B_s)_{lower} = (\frac{1-n}{B_m} + \frac{n}{B_\ell})^{-1}$		Voigt's lower bound Parallel configuration of pore liquid and solid grain with respect to passing P-wave	
$B_s = B_d + \frac{B_\ell}{n}(\frac{B_m - B_d}{B_m})^2$ $G_s = G_d$	B_d [Pa]: Bulk modulus of a dry granular skeleton G_s [Pa]: Shear modulus of a liquid-saturated granular skeleton G_d [Pa]: Shear modulus of a dry granular skeleton	Simplified Gassmann's Eqn.	De-hua and Batzle, 2004

Table 5.3.Continued Relationships for stiffness of geomaterials with respect to liquid-saturation.

Equation	Parameters	Notes	References
$\tau = G\gamma + \eta\dot{\gamma}$	τ [Pa]: Shear stress G [Pa]: Shear modulus of solid grain γ: Shear strain imposed on both solid and liquid η [Pa.s]: Viscosity of pore liquid $\dot{\gamma}$ [s^{-1}]: Shear strain rate	Voigt material contains an elastic spring and a viscous damper in parallel	www.wikipedia.org/wiki/ Kelvin_Voigt_material
$B_s = B_d + B_{sus} = B_d + \frac{1}{\frac{n}{B_\ell} + \frac{1-n}{B_m}}$	B_{sus} [Pa]: Bulk modulus of a suspension (non-contacting solid grains in a liquid)		
$\rho_s = (1-n)\rho_m + n\rho_f = (1-n)\rho_m + nS\rho_w + n(1-S)\rho_a = (1-n)\rho_m + nS\rho_w$	ρ_s [$kg.m^{-3}$]: Mass density of unsaturated granular material ρ_m [$kg.m^{-3}$]: Mass density of solid mineral ρ_f [$kg.m^{-3}$]: Mass density of pore-fluid ρ_w [$kg.m^{-3}$]: Mass density of water ρ_a [$kg.m^{-3}$]: Mass density of air S: Degree of water saturation		

Experimental studies show that the bulk modulus of a sandstone specimen increases about 50 percent upon water-saturation (De-hua and Batzle, 2004). The compressional wave velocity is higher in water-saturated sandstones compared to that for oil-saturated and dry sandstones (Gregory, 1976; Wang and Nur, 1990).

Effects of temperature. Elastic P- and S-wave velocities decrease linearly with increasing temperature in hydrocarbon-saturated sediments (constant frequency). This behavior has been associated with the melting point of solid or solid-like heavy oil in the pores. Higher oil carbon number (number of carbon atoms in a molecule of hydrocarbon) correlates with higher wave velocity because of higher molecular weight (Wang and Nur, 1990). Linearly decreasing trend of V_P and V_S with temperature is also observed for brine-saturated and dry sandstones (Wang and Nur, 1988b). Figure 5.4 shows the P-wave velocity for hydrocarbons only: once again, the velocity decreases linearly with temperature and it is higher for hydrocarbons with higher carbon number.

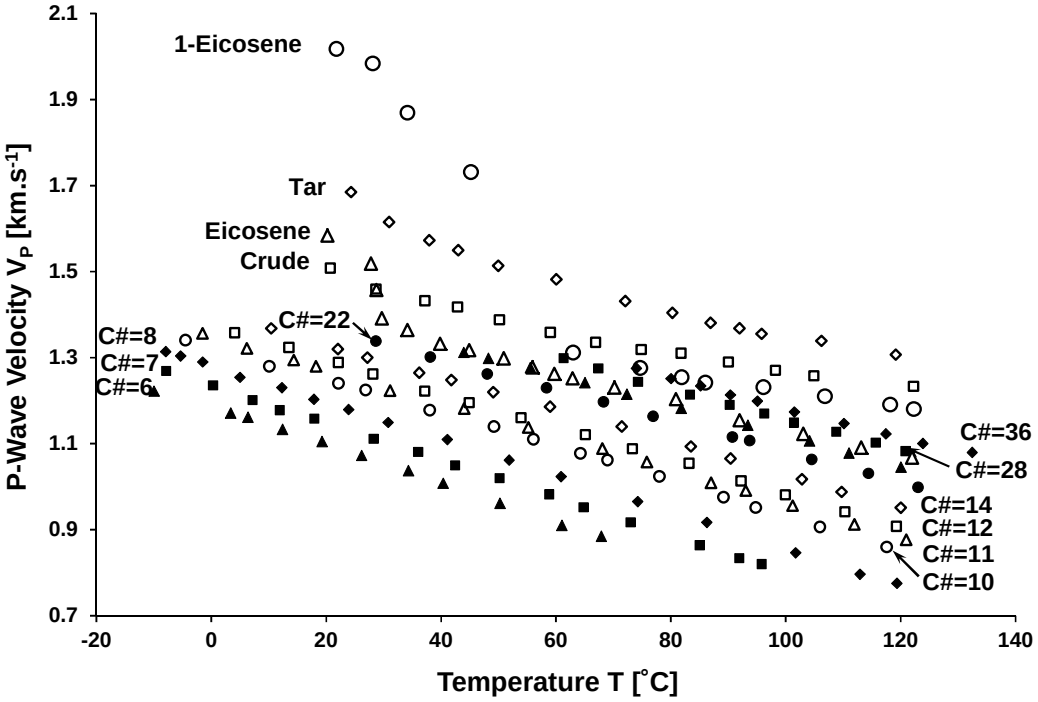

Figure 5.4. P-wave velocity versus temperature. Hydrocarbons of different carbon numbers (no mineral frame). Data from: Wang and Nur, 1990 and Wang and Nur, 1988b. C#: the number of carbon atoms in a molecule of hydrocarbon.

Figure 5.5 and 5.6 show the variation of P- and S-wave velocities with temperature in various liquid-saturated sands and sandstones. The frequency is constant in above-mentioned studies f=800 Hz.

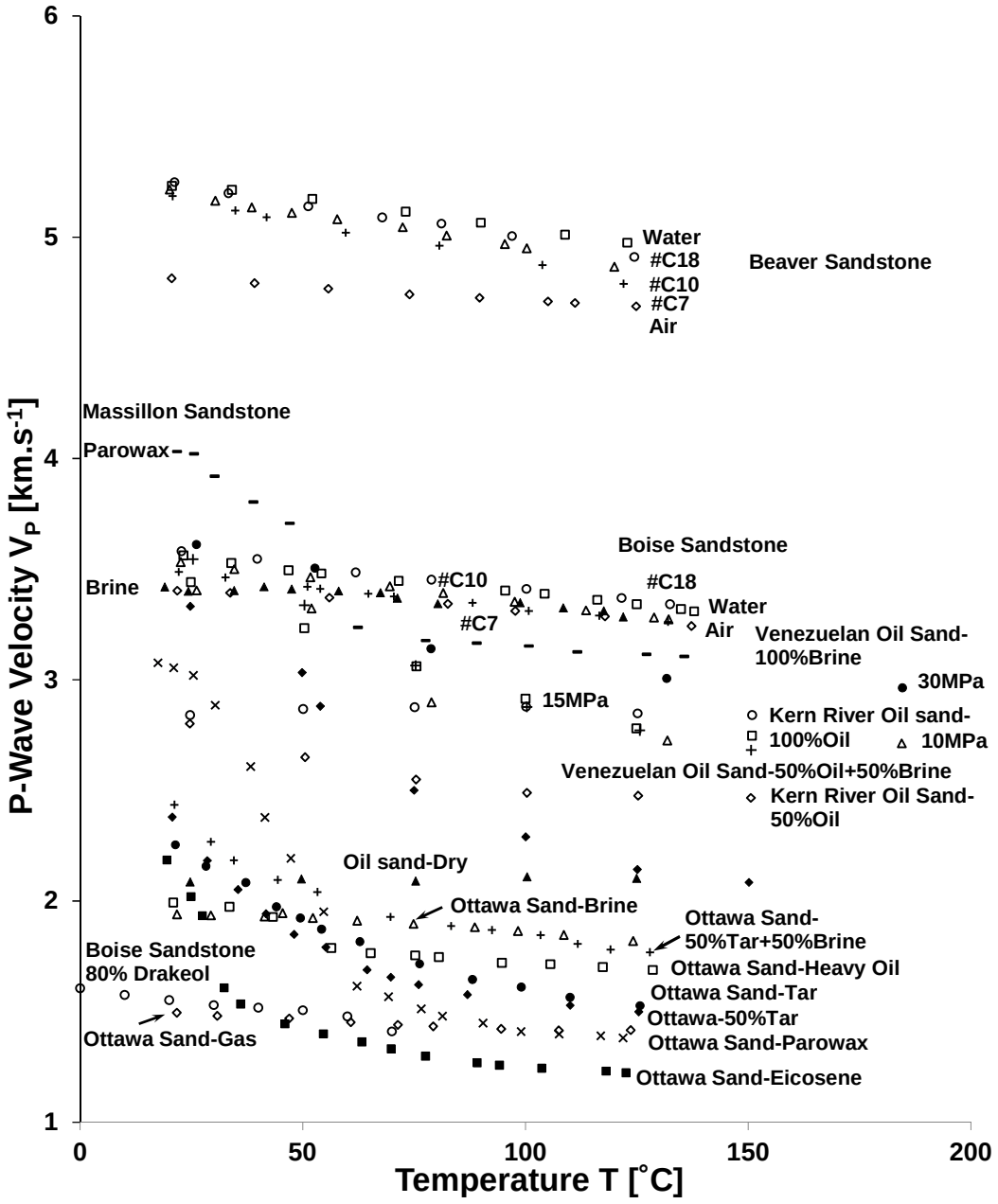

Figure 5.5. Compressional wave velocity versus temperature for sands, sandstones and oil sands (Effective confining stress = 15 MPa). Data from: Tosaya et al., 1984; Tosaya et al., 1987; Wang and Nur, 1988b; Wang and Nur, 1990.

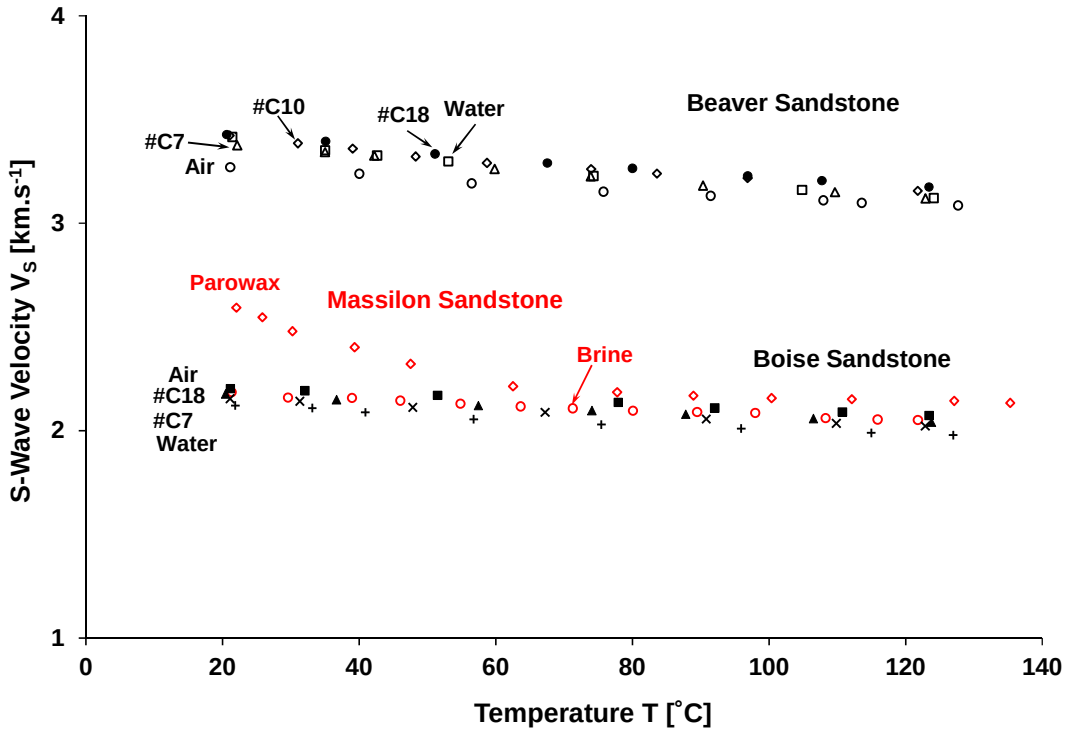

Figure 5.6. Shear wave velocity versus temperature for sands, sandstones and oil sands (Effective confining stress = 15 MPa). Data from: Tosaya et al., 1984; Tosaya et al., 1987; Wang and Nur, 1988b; Wang and Nur, 1990.

Coupled processes involved in thermally enhanced oil recovery are complex. Differential thermal expansion of solid particles and pore-filling oil can increase pore pressure, alter the state of stress, change the ratio between dissolved gas and oil, affect the sand and change all its thermo-hydro-mechanical properties. Large property changes are associated to the thermal expansion upon the temperature rise to 60-80 ˚C in dense oil-bearing formations at shallow depths. In particular, these formations may experience shear dilation and increases in compressibility, porosity and permeability (Shafiei and Dusseault, 2013). Very porous formations such as diatomite in California with porosity n

> 0.5 may experience internal collapse upon heating and consequent decrease in porosity and permeability (Hoffman and Kovscek, 2005).

The in-situ temperature in reservoirs found in Canada, Venezuela and the U.S. can reach 50 ˚C at the depth of 1000 m. During heat treatment, such as steam injection, the temperature can reach 200 ˚C (Barson et al., 2001). For comparison, the glass transition temperature of viscous oil is between -80 and -40 ˚C (Abivin et al., 2012).

Thermal conductivity of oil sands increases with increasing bitumen content and decreases with increasing temperature (Karim and Hanafi, 1981). Thermal conductivity of bitumen alone and sand alone decreases with increasing temperature (Hanafi and Karim, 1986).

Effects of effective stress. The differential thermal expansion that solid grains and mineral skeleton experience relative to that of pore-filling fluid during heating may increase the pore pressure that decreases effective stress. On the other hand, oil viscosity decreases and facilitates its drainage. The coupling between the thermal front, fluid pressure and drainage defines the effective stress.

The effective stress σ' [MPa] defines the stiffness, compressibility and the thermal conductivity of granular media. In terms of shear stiffness G [MPa]:

$$G = a\left[\frac{\sigma'}{1\,\mathrm{kPa}}\right]^{b} \tag{5.2}$$

where the exponent b reflects the type of inter-particle contact that is responsible for small-strain deformation at constant-fabric, and the role of fabric change on compressibility (Cascante and Santamarina, 1996). Similarly, the thermal conductivity k_T [$W.m^{-1}.K^{-1}$] is linearly related to effective stress in a log-normal scale as (Chapter 3 & 4):

$$k = k_1[1 + \beta \log(\sigma'/1\mathrm{kPa})] \tag{5.3}$$

Where k_1 [$W.m^{-1}.K^{-1}$] is the thermal conductivity at 1 kPa at a given temperature and β is the indicator parameter for stress-sensitivity of thermal conductivity. The small-strain stiffness and thermal conductivity are affected by diagenesis, such as pressure dissolution-precipitation in wet or saturated soils and cementation (Acar and Eltahir, 1986). Pressure dissolution-precipitation has been reported in oil sands. By measuring the shear wave velocity at different levels of stress, both small and large strain stiffnesses can be captured that are a measure of the compressibility of the medium (Cha et al., 2014).

Effect of Frequency. In-situ seismic methods operate at frequencies that range from 0.1 Hz to 10 Hz. This range is much lower than the frequencies commonly imposed in laboratory tests: 10 Hz to 100 (typical piezocrystals) (Eastwood, 1993; Santamarina et al., 2001).

Hydrocarbons are viscous, i.e., the shear resistance is proportional to the shear rate $\tau = \eta.\dot{\gamma}$. In addition, they have a shear-thinning behavior Martin-Alfonso et al., 2006 so that the viscosity η [Pa.s] decreases with shear rate $\dot{\gamma}$ [s^{-1}]. Consequently, the shear wave velocity is frequency-dependent and laboratory values will be different to field values measured at lower frequencies.

5.3. EXPERIMENTAL PROCEDURE

Specimen. A disturbed sample of extra heavy oil-bearing sand from the Orinoco Belt in Venezuela is tested in this study. The oil content is 16.4%. A washed specimen (washed with Kerosene and oven-dried; then, washed with alcohol and boiled in deionized water and oven-dried) is also tested as part of this study.

Device. A series of one-dimensional consolidation tests are conducted in a stainless steel cylindrical cell (inner diameter 71.6 mm, wall thickness 24.5 mm and height 76.2 mm). The cell and the two caps are mounted within a stainless steel reaction frame designed to be housed within a convection oven (design sheets are provided in Appendix C). Both upper and lower caps are "floating type" to slide into the cell; furthermore, the cylinder is covered with a double layer of grease-and-polymer wrap to minimize side-friction. A schematic view of experimental device is shown in Figure 5.7.a. Both upper and lower caps have drainage paths connected to exit ports, and the caps surface is covered by a thin textile layer to avoid sand from draining out.

A hydraulic cylinder is mounted in series with the soil chamber (10 tons, ENERPAC RCS101). It is connected to a pressure booster that converts a pneumatic pressure into a hydraulic pressure and magnifies it up to 140 times. All fittings and hose are rated for a pressure of 69 MPa. The pressure circuit is sketched in Figure 5.7.c.

Instrumentation. The upper cap houses a thermal needle probe to measure the thermal conductivity of the medium. An LVDT is used for settlement measurements. Both sensors were calibrated at room temperature and an elevated temperature of T = 70 ˚C. Bender elements are installed in the center of both caps to monitor the evolution of shear wave velocity in specimen with varying stress and temperature. Parallel-type bender elements (12.7×8.0×0.6 mm) are used for both source and receiver; they are mounted in nylon screws using epoxy. Elements protrude ~5 mm into the specimen. The tip-to-tip distance is calculated for each shear wave measurement based on the specimen initial height, settlement and protruded length. the instrumentation is shown in Figure 5.7.b.

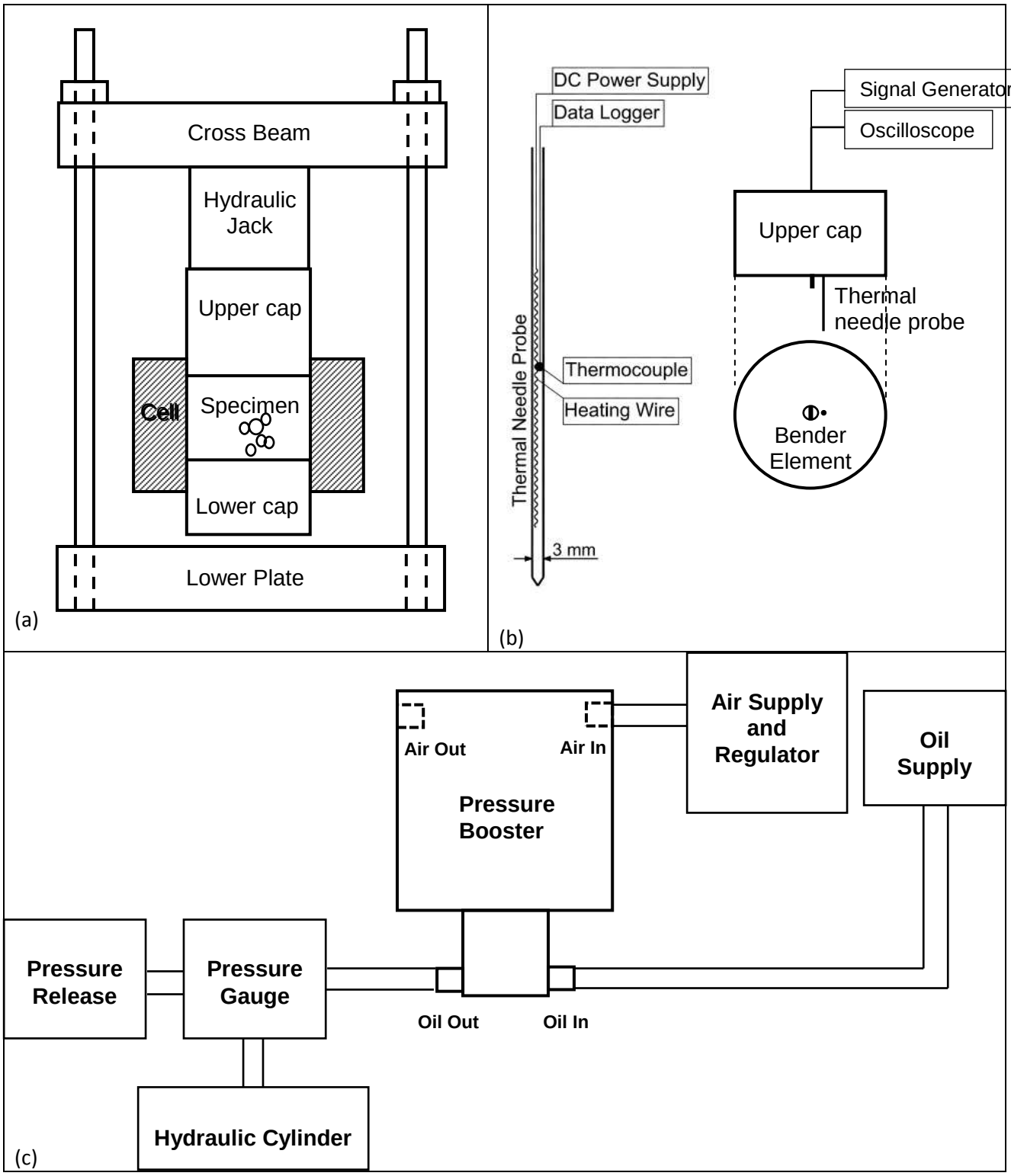

Figure 5.7. Experimental device. (a) Assembled self-reacting stainless steel frame, thick-wall consolidation cell with floating caps, and hydraulic cylinder, (b) Instrumentation embedded into upper and lower caps, and (c) Pressure control system.

Procedure. Thin layers (5 mm thick) of the weighed material are compacted inside the cell using a cylindrical rod (50 blows per layer, W=100 g, dropping distance=50 mm). The specimen height is measured after assembling all parts.

Specimens are incrementally loaded to reach a maximum vertical stress of ~18 MPa. The high temperature is provided using an oven. In high temperature experiments, the specimen is loaded up to 1.25 MPa at room temperature first. Then, the specimen, the hydraulic cylinder and frame system (excluding the pump) is heated inside an oven until the temperature inside the specimen reaches to the specified temperature (Figure 5.8).

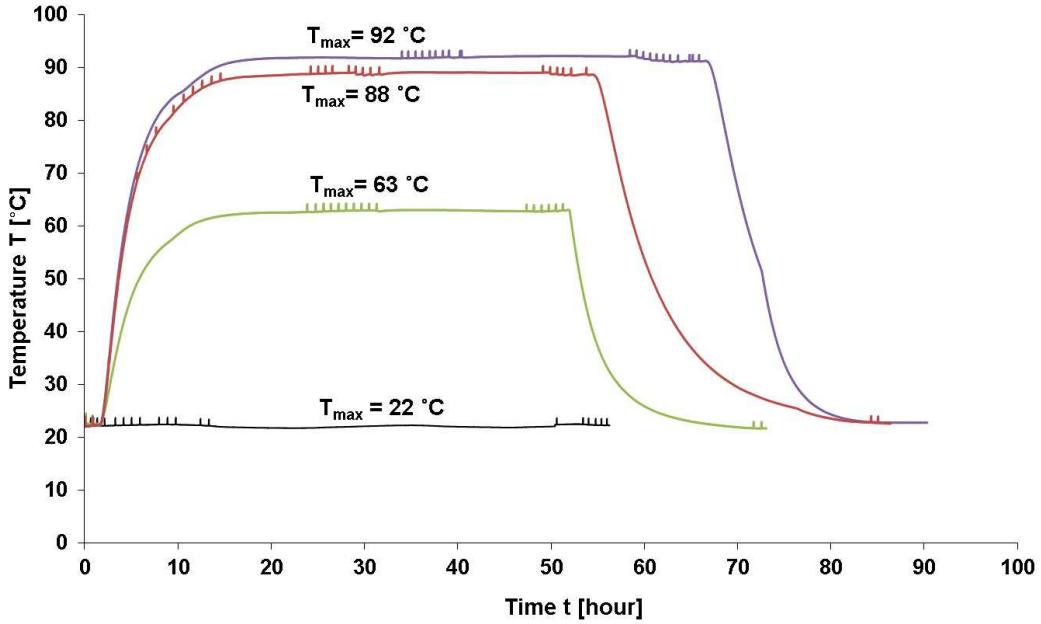

Figure 5.8. Temperature history for all tests. Small temperature pikes correspond to thermal conductivity measurements.

Successive increments in vertical stress are imposed at ~1 hour intervals, until reaching to the maximum stress (18 MPa), when the specimen is allowed to creep under the constant stress for ~20 hours. Unloading is conducted in stages until the vertical stress reaches to σ'=1.25 MPa. The oven is turned off, and the temperature inside the specimen

gradually decreases to the room temperature. Finally, the specimen is completely unloaded at room temperature. The specimen height, thermal conductivity and shear wave velocity are measured throughout the complete test sequence.

A 400 g sample of the original "as received" sediment and 400 g sample of a tested specimen (loaded up to 18 MPa and heated up to 89 ˚C) are washed separately with Kerosene, boiled in water for 2 hours, washed with isopropyl alcohol, boiled in deionized water for 15 minutes, and finally oven-dried for 24 hours. The original liquid (oil and brine) content and specific gravity are measured using the "as received" specimen. SEM images are taken from both specimens to explore particle shape (Cho et al., 2006) and surface features (Figure 5.9). Additional tests are performed to determine the grain size distribution, ferromagnetic content, and extreme void ratios e_{max} and e_{min} of these two clean sediments (Figure 5.10).

(a) Washed as received sand (b) Washed tested sand

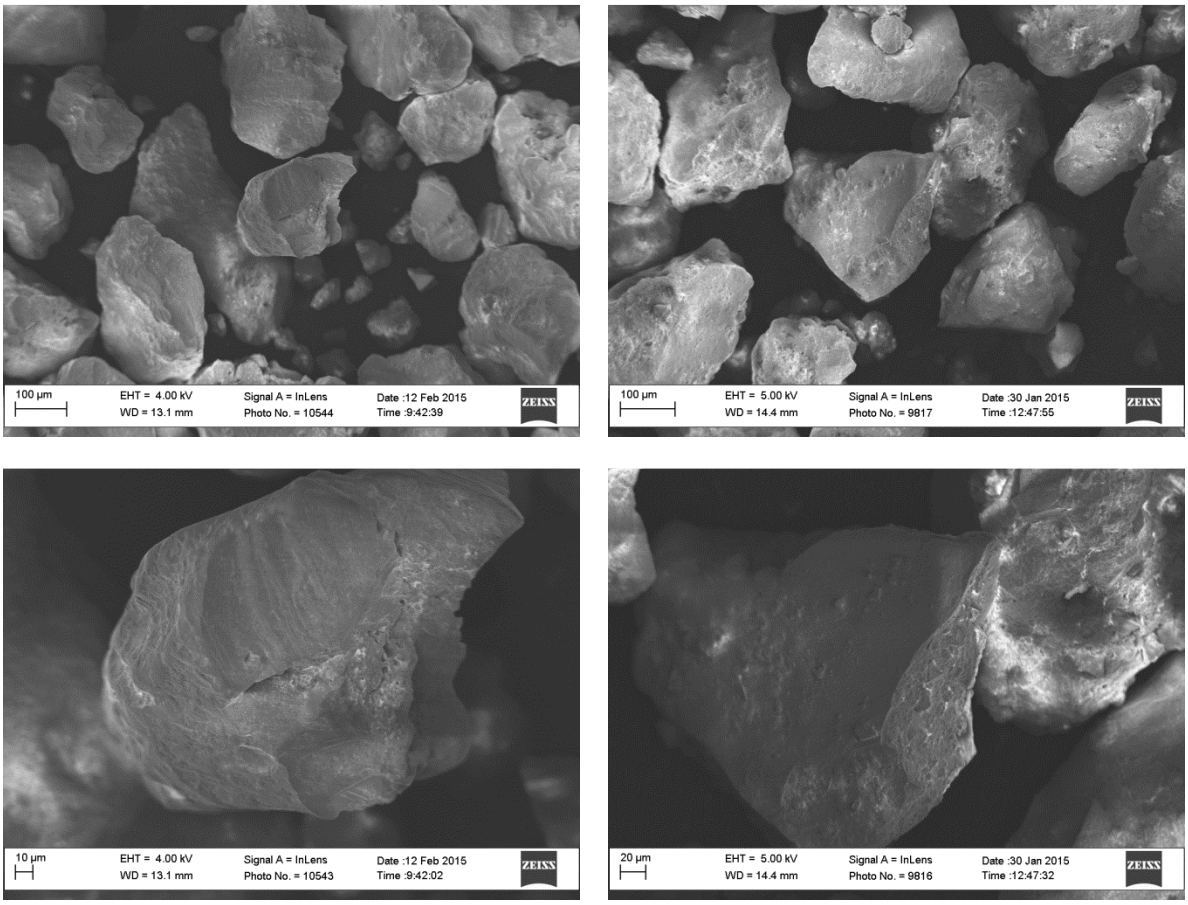

Figure 5.9. Scanning electron microscope images of: (a) As-received sand. (b) Tested sand (loaded up to 18 MPa and heated up to 89 ˚C). Samples were Kerosene- and isopropyl alcohol-washed, boiled in deionized water and oven-dried.

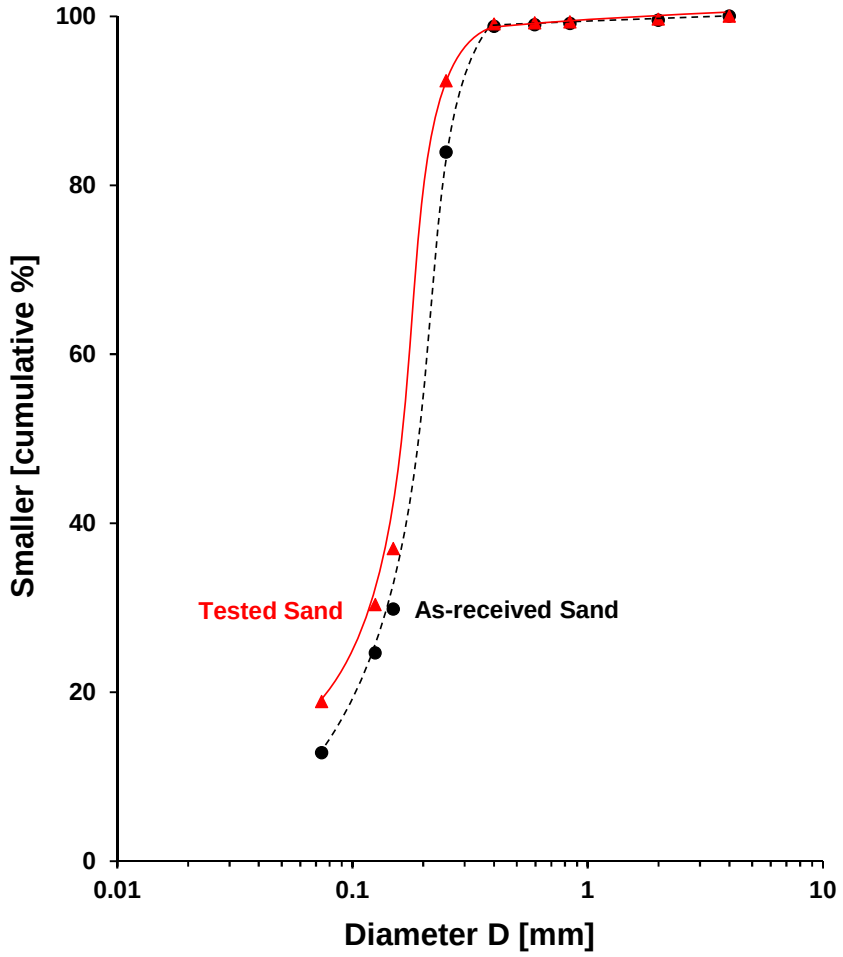

Figure 5.10. Grain size distribution and extreme void ratios for as received and tested (σ'_{max}=18 MPa and T_{max}=89 ˚C) oil-bearing sand.

5.4. EXPERIMENTAL RESULTS

The data reduction procedure and salient observations follow:

- There are evidences of particle crushing under high stress and high temperature.
- There is a high quartz content (98%) in these sediments and there are evidences of crystal overgrowth and pressure dissolution and precipitation and conchoidal fractures on sand particles.

- Particles are mostly angular with fresh edges and crushed surfaces that are more readily recognizable in loaded specimens.
- The sediment has no ferromagnetic content.
- Specimen void ratio values, calculated from the settlement, specific gravity (G_S=2.68) and pore-liquid content (w=0.164) measurements ($\rho_d=\rho_t/(1+w)$, $e=\rho_s/\rho_d-1$), are plotted versus vertical effective stress in Figure 5.11 for all specimens tested at different temperatures. Although the initial state of the specimens is slightly different, they converge to almost the same void ratio at the highest stress level with a similar slope indicated by compression index C_c = 0.2.

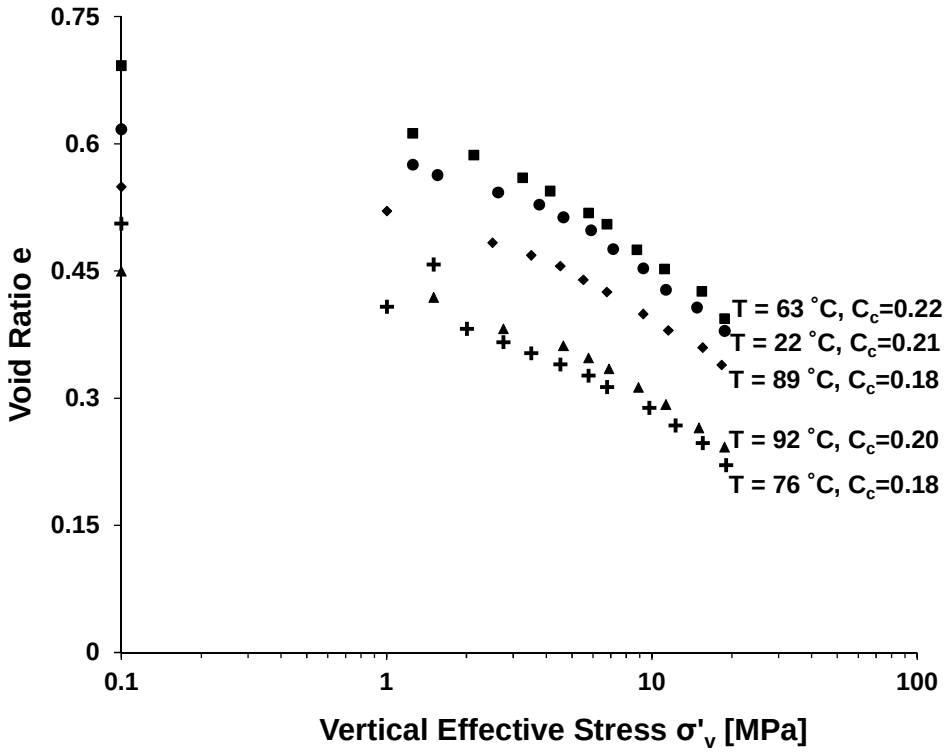

Figure 5.11. Void ratio versus vertical effective stress. The compression index, computed between σ'=3.7 MPa and σ'=18.7 MPa, is shown for all specimens.

- Specimens creep under the highest vertical stress, but it is higher at high temperatures. Deformation is the same for both specimens tested at 63 and 89 ˚C under 18 MPa vertical effective stress (Figure 5.12).

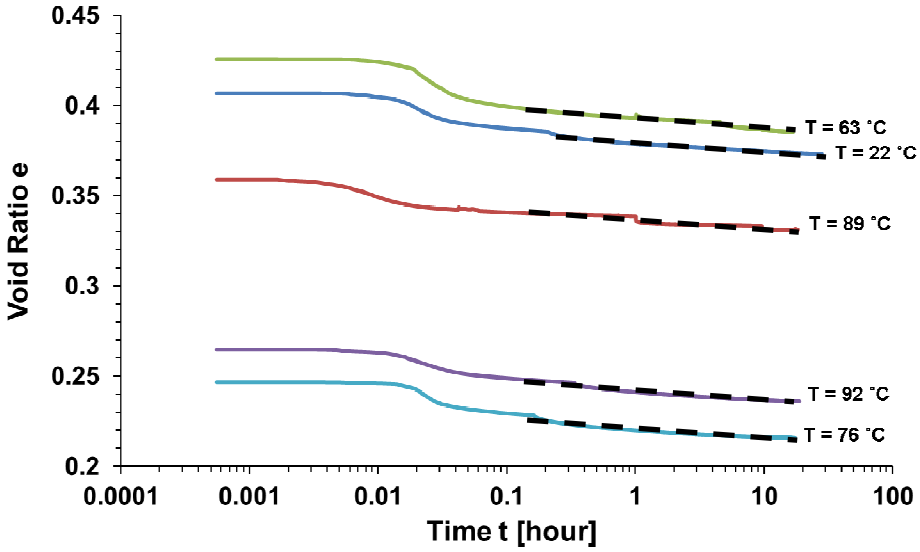

Figure 5.12. Effect of temperature and initial void ration on creep rate under a vertical effective stress σ'=18.7 MPa.

- Figure 5.13 shows the output wave signature.

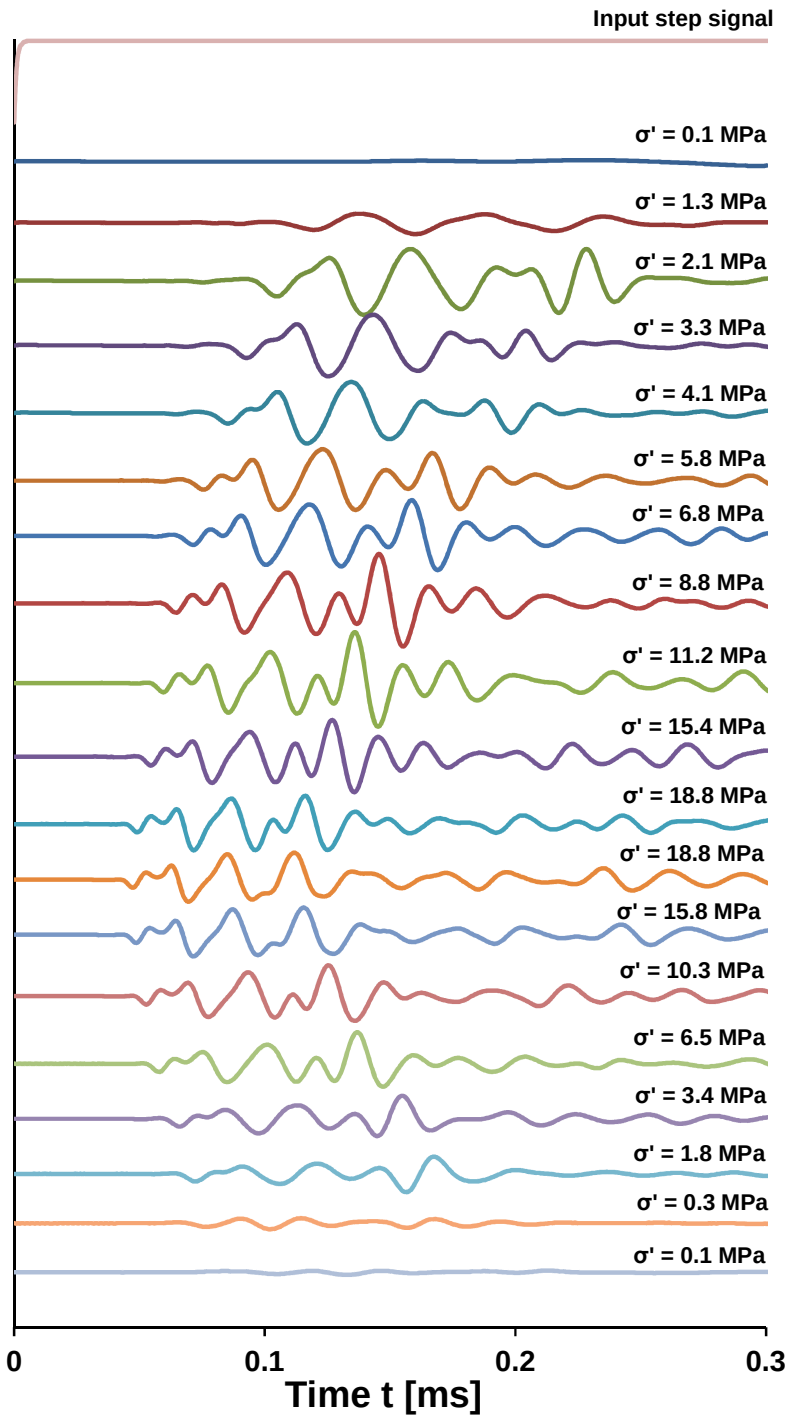

Figure 5.13. Wave signatures during loading and unloading for the test conducted at T = 63 ˚C on oil bearing sand.

- Figure 5.14 shows the effects of oil-saturation and the temperature on small strain stiffness of oil sand. The first arrival time is selected on an output signal (Voltage V [V] vs. time t [ms]) and the shear wave velocity V_S [$m.s^{-1}$] is computed by dividing the tip-to-tip distance L [mm] by the first arrival time t_{fa} [ms].

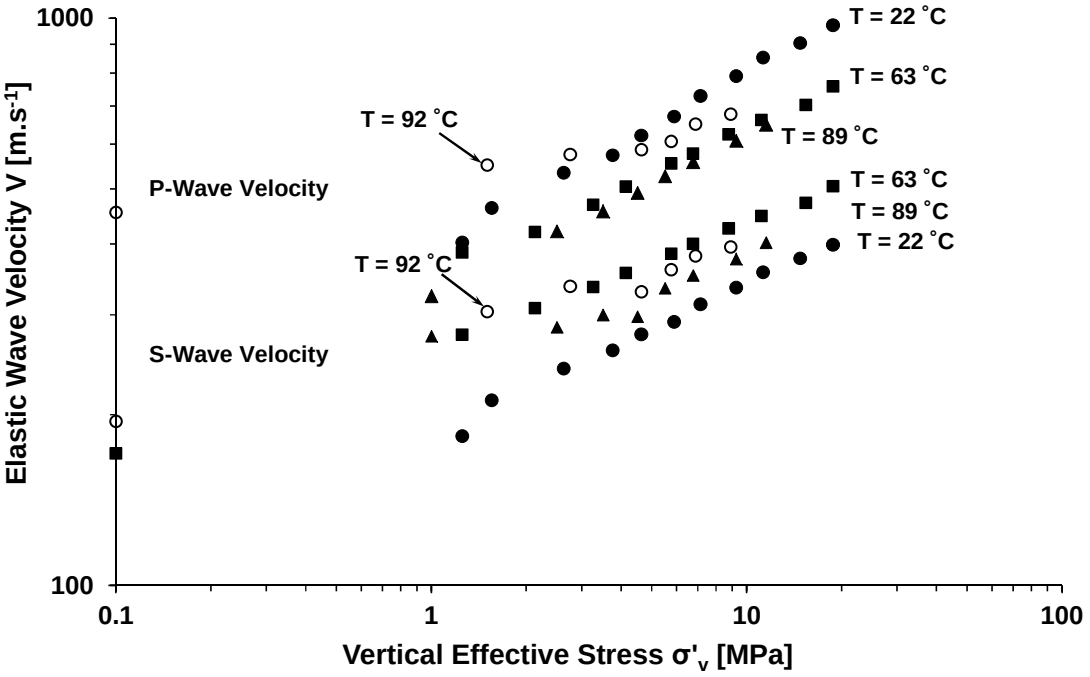

Figure 5.14. Compressional and shear wave velocity data during loading for oil-bearing sand (data shown for loading only).

- Compressional and shear wave velocities increase with effective stress for all dry and oil-bearing sediments tested at different temperatures (Figure 5.14).
- Overall, the compressional wave velocity decreases with temperature for oil-bearing sediments, but the effect vanishes at high stresses so that V_P of all oil-bearing specimens tested at different temperatures converges to a single value beyond 9 MPa vertical stress (Figure 5.14.a).

- The shear wave velocity for oil-bearing specimens increases with temperature (Figure 5.14.b).
- Figure 5.10 shows that extensive crushing occurs during the test (loading up to 18 MPa and heating up to 89 ˚C). This process changes the grain size distribution, e_{max}, and e_{min} of the sediment after the test.
- Figure 5.15 shows that the frequency of P- and S-wave velocities increase with stress.
- Figure 5.16.a shows a typical dataset of temperature evolution with time for measurement of thermal conductivity. The slope of the linear part of the temperature versus the logarithm of time is used for thermal conductivity calculation.
- The thermal conductivity of all specimens increase with stress (Figure 5.16-b).
- The thermal conductivity of tested oil sand sample decreases with temperature (Figure 5.16-b).

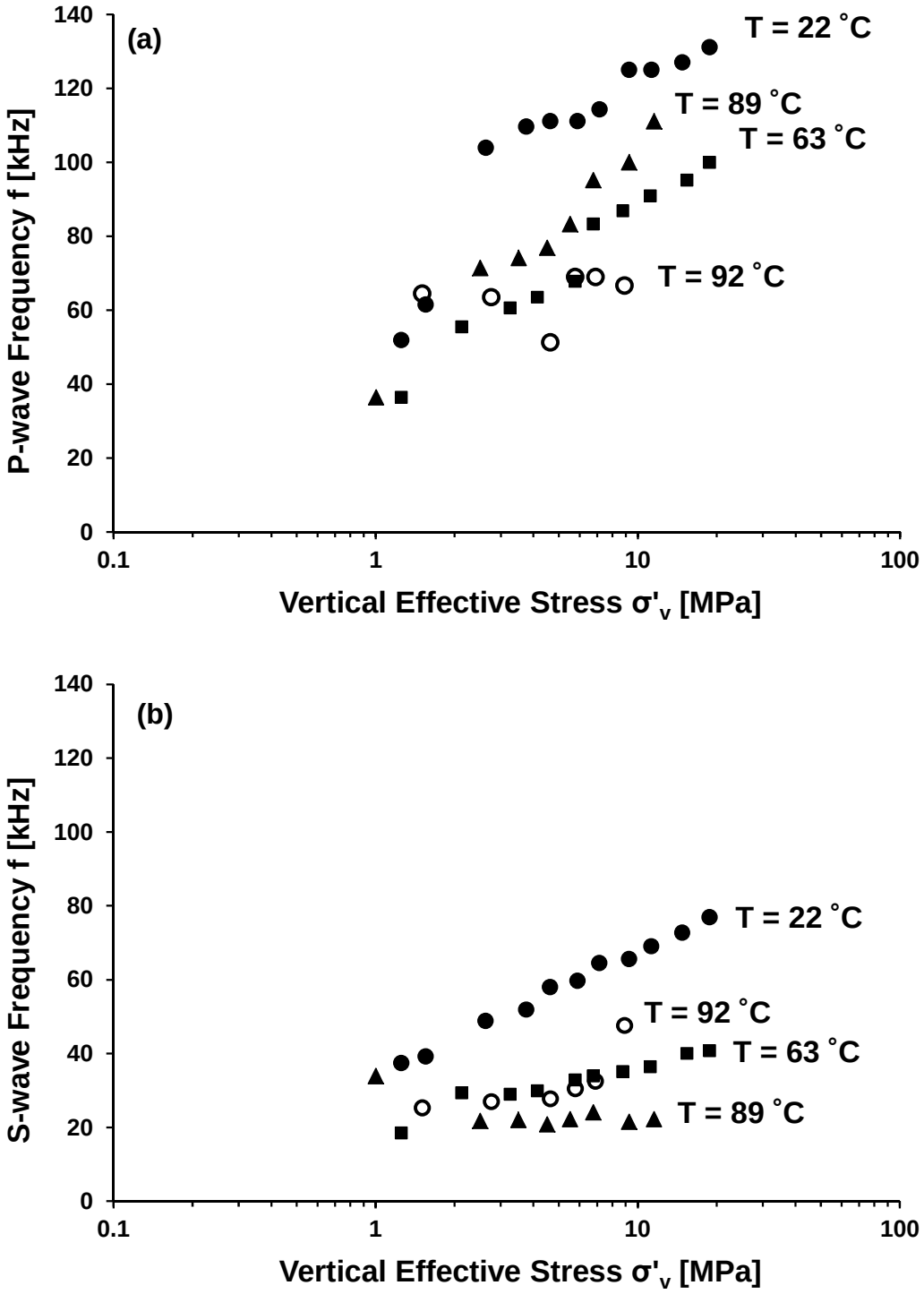

Figure 5.15. The frequency of: (a) compressional, and (b) shear wave velocities versus vertical effective stress during loading for oil-bearing sand.

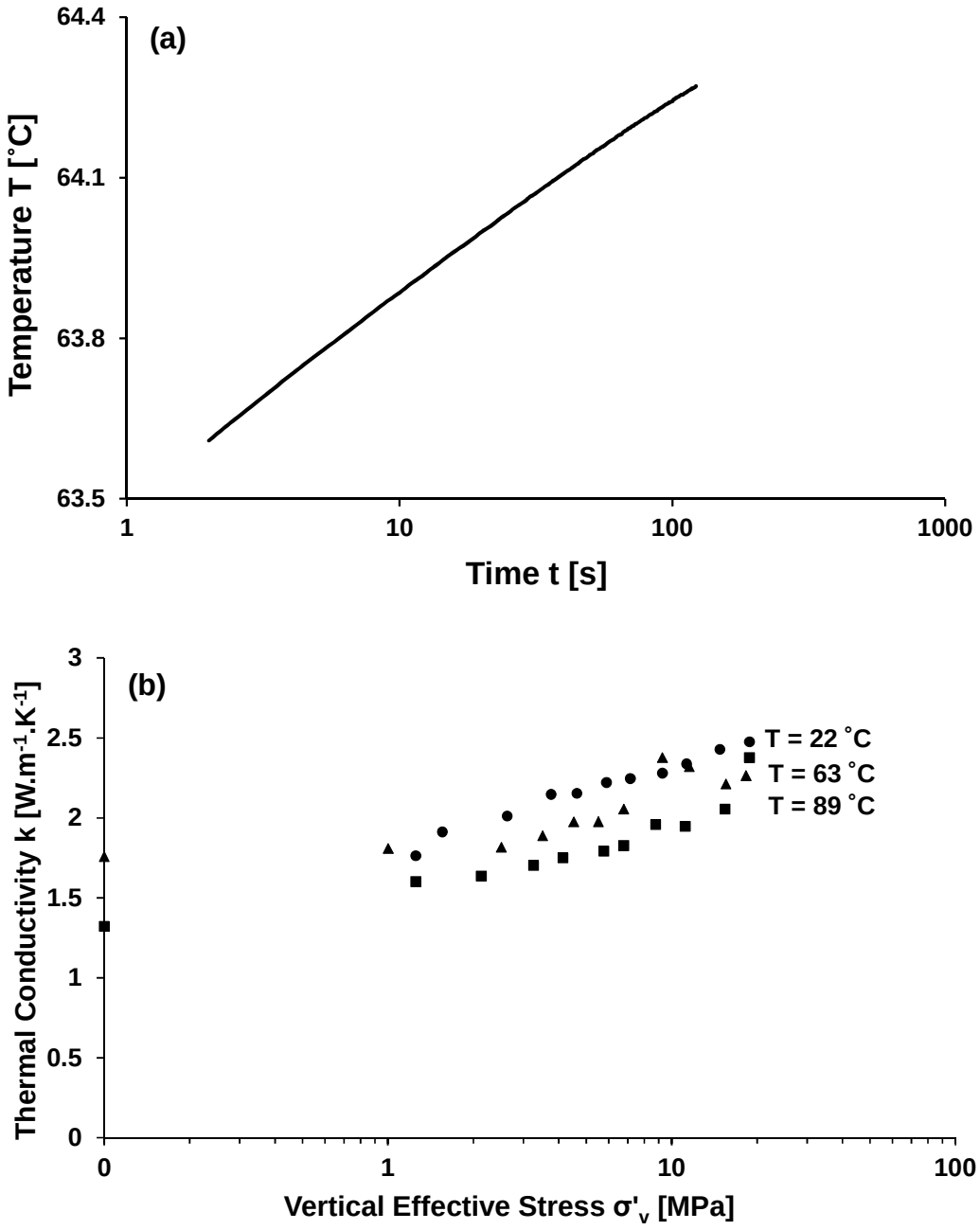

Figure 5.16. (a) Typical dataset for temperature versus time from thermal conductivity measurement - Case: T = 63 ˚C and σ’ = 8.8 MPa during loading. (b) Thermal conductivity versus effective stress for loading.

5.5. ANALYSES AND DISCUSSION

Results from this study have implications to the stability of shallow open-pit mining slopes, subsidence prediction, deep wellbore integrity, design of thermal stimulation and production wells, and production analyses.

Given the fact that these formations have taken the overburden stress for thousands of years without getting drained to surrounding media suggests that they had been completely consolidated for a long geologic time before the light oil migrated into them and then weathered; thus, extraction of oil should not cause significant settlement or instability. Experimental results in this study show that the presence of viscous oil has no effect on mechanical properties of oil-bearing sediments.

Material type and inter-particle contact condition can be estimated by the variation of elastic wave velocity with respect to effective stress. If solid coarse particles (sand) are not in close contact, as some researchers (Mossop, 1980) suggest, the bulk modulus of the solid-fluid mixture can be defined by that of a suspension. This is not readily possible because oil sand reservoirs have taken the overburden load for thousands of years and this is only possible through contacting particle chains and mobilization of effective stress. Second alternative of microstructure of oil sands is that sand particles are in plane-to-plane Dusseault and Morgenstern, 1978 contact with water-saturated clay minerals coating their surface and precipitated around the contact points (cementation at menisci). b exponent in power relation between the stiffness and stress is 0.5 for such contacts. Data in this study indicates b=0.4, 0.5 and 0.6 for specimens tested at 89, 63 and 22 ˚C which are indicator of the contact behavior. Last alternative is a convex-to-concave

inter-particle contact or interlocked structure because of the presence of crystal overgrowth.

5.6. CONCLUSIONS

- The shear wave velocity, which is an indicator of small strain and constant fabric stiffness, increases with both stress and temperature because the mineral-to-mineral contact gets improved.
- The compression index, which is an indicator of mid-strain stiffness and particle rearrangement, is independent of temperature.
- Time-dependent behavior of viscous oil-bearing sediment at high stress shows no clear dependency on the temperature; hence, it is mineral-controlled.
- The thermal conductivity decreases with temperature, which is an indicator of high quartz content.
- The thermal conductivity increases with effective stress, which is due to improved inter-particle contacts and decreased contact thermal resistance.

5.7. REFERENCES

Abivin, P., Taylor, S. D., and Freed, D. (2012). "Thermal Behavior and Viscoelasticity of Heavy Oils." Energy & Fuels, 26(6), 3448-3461.

Acar, Y. B., and Eltahir, E. A. (1986). "Low Strain Dynamic Properties of Artificially Cemented Sand." Journal of Geotechnical Engineering-Asce, 112(11), 1001-1015.

Agar, J. G., Morgenstern, N. R., and Scott, J. D. (1987). "Shear-Strength and Stress-Strain Behavior of Athabasca Oil Sand at Elevated-Temperatures and Pressures." Canadian Geotechnical Journal, 24(1), 1-10.

Anochie-Boateng, J., and Tutumluer, E. (2009). Shear Strength Properties of Naturally Occurring Bituminous Sands.

Barson, D., Esslinger, P., and Bachu, S. (2001). "Flow Systems in the Mannville Group in the East-Central Athabasca Area and Implications for Steam-Assisted Gravity Drainage (SAGD) Operations for in Situ Bitumen Production." Bulletin of Canadian Petroleum Geology, 49(3), 376-392.

Bear, J. (1979). Hydraulics of Groundwater, McGraw-Hill International Book Co.

Canada, N. E. B. o. (2004). Canada's Oil Sands : Opportunities and Challenges to 2015, Calgary, Alberta.

Cascante, G., and Santamarina, J. C. (1996). "Interparticle Contact Behavior and Wave Propagation." Journal of Geotechnical Engineering-Asce, 122(10), 831-839.

Cervenan, M. R., Vermeulen, F. E., and Chute, F. S. (1981). "Thermal Conductivity and Specific Heat of Oil Sand Samples." Canadian Journal of Earth Sciences, 18(5), 926-931.

Chapman, D. S., Keho, T. H., Bauer, M. S., and Picard, M. D. (1984). "Heat-Flow in the Uinta Basin Determined from Bottom Hole Temperature (BHT) Data." Geophysics, 49(4), 453-466.

Cho, G. C., Dodds, J., and Santamarina, J. C. (2006). "Particle Shape Effects on Packing Density, Stiffness, and Strength: Natural and Crushed Sands." Journal of Geotechnical and Geoenvironmental Engineering, 132(5), 591-602.

De-hua, H., and Batzle, M. L. (2004). "Gassmann's Equation and Fluid-Saturation Effects on Seismic Velocities." Geophysics, 69(2), 398-405.

Drelich, J., Lelinski, D., and Miller, J. D. (1996). "Bitumen Spreading and Formation of Thin Bitumen Films at a Water Surface." Colloids and Surfaces a-Physicochemical and Engineering Aspects, 116(1-2), 211-223.

Dusseault, M. B. (2001). "Comparing Venezuelan and Canadian Heavy Oil and Tar Sands." Canadian International Petroleum Conference, Petroleum Society, Canadian Institute of Mining, Metallurgy and Petroleum, Calgary, Alberta, Canada.

Dusseault, M. B., and Morgenstern, N. R. (1978). "Shear-Strength of Athabasca-Oil-Sands." Canadian Geotechnical Journal, 15(2), 216-238.

Dusseault, M. B., and Scafe, D. (1979). "Mineralogical and Engineering Index Properties of the Basal Mcmurray Formation Clay Shales." Canadian Geotechnical Journal, 16(2), 285-294.

Eastwood, J. (1993). "Temperature Dependent Propagation of P-Waves and S-Waves in Cold Lake Oil Sands - Comparison of Theory and Experiment." Geophysics, 58(6), 863-872.

Gates, I. D., Adams, J., and Larter, S. (2008). "The Impact of Oil Viscosity Heterogeneity on the Production Characteristics of Tar Sand and Heavy Oil Reservoirs. Part II: Intelligent, Geotailored Recovery Processes in Compositionally Graded Reservoirs." Journal of Canadian Petroleum Technology, 47(9), 40-49.

Glassett, J. M., and Gould, W. R. (1976). "Evaluation of the Utah Oil Sand Resource." United States Department of the Interior Bureau of Mines, Utah.

Gregory, A. R. (1976). "Fluid Saturation Effects on Dynamic Elastic Properties of Sedimentary Rocks." Geophysics, 41(5), 895-921.

Han, G., Bruno, M., and Dusseault, M. B. (2007). "How Much Oil You Can Get from CHOPS." Journal of Canadian Petroleum Technology, 46(4), 24-32.

Hanafi, A., and Karim, G. A. (1986). "The Thermal Conductivity of Oil Sands Using a Transient Method." Journal of Energy Resources Technology-Transactions of the Asme, 108(4), 315-320.

Head, I. M., Jones, D. M., and Larter, S. R. (2003). "Biological Activity in the Deep Subsurface and the Origin of Heavy Oil." Nature, 426(6964), 344-352.

Hoffman, B. T., and Kovscek, A. R. (2005). "Displacement Front Stability of Steam Injection into High Porosity Diatomite Rock." Journal of Petroleum Science and Engineering, 46, 253-266.

James, K. H. (2000). "The Venezuelan Hydrocarbon Habitat, Part 1: Tectonics, Structure, Palaeogeography and Source Rocks." Journal of Petroleum Geology, 23(1), 5-53.

Karim, G. A., and Hanafi, A. (1981). "The Thermal Conductivity of Oils Sands." Canadian Journal of Chemical Engineering, 59(4), 461-464.

Kiser, G. D. (1987). "Exploration Results, Machete Area, Orinoco Oil Belt, Venezuela." Journal of Petroleum Geology, 10(2), 149-162.

Larter, S., Huan, H., Adams, J., Bennett, B., Jokanola, O., Oldenburg, T., Jones, M., Head, I., Riediger, C., and Fowler, M. (2006). "The Controls on the Composition of Biodegraded Oils in the Deep Subsurface: Part II - Geological Controls on Subsurface Biodegradation Fluxes and Constraints on Reservoir-Fluid Property Prediction." Aapg Bulletin, 90(6), 921-938.

Linberg, W. R. (1980). "Tar Sand Extraction by Steam Stimulation and Steam Drive: Measurement of Physical Properties."

Long, J., Drelich, J., Xu, Z. H., and Masliyah, J. H. (2007). "Effect of Operating Temperature on Water-Based Oil Sands Processing." Canadian Journal of Chemical Engineering, 85(5), 726-738.

Martin-Alfonso, M. J., Martinez-Boza, F., Partal, P., and Gallegos, C. (2006). "Influence of Pressure and Temperature on the Flow Behaviour of Heavy Fuel Oils." Rheologica Acta, 45(4), 357-365.

Martinez, A. R. (1987). "The Orinoco Oil Belt, Venezuela." Journal of Petroleum Geology, 10(2), 125-134.

Mercier, P. H. J., Patarachao, B., Kung, J., Kingston, D. M., Woods, J. R., Sparks, B. D., Kotlyar, L. S., Ng, S., Moran, K., and McCracken, T. (2008). "X-ray Diffraction (XRD)-Derived Processability Markers for Oil Sands Based on Clay Mineralogy and Crystallite Thickness Distributions." Energy & Fuels, 22(5), 3174-3193.

Meyer, F., and deWitt, W., Jr. (1990). Definition and World Resources of Natural Bitumens, Denver, CO (USA); US Geological Survey.

Meyer, R. F., and Attanasi, E. D. (2003). Heavy Oil and Natural Bitumen: Strategic Petroleum Resources, [Reston, Va.] : U.S. Dept. of the Interior, U.S. Geological Survey, [2003].

Mossop, G. D. (1980). "Geology of the Athabasca Oil Sands." Science, 207(4427), 145-152.

Obermajer, M., Osadetz, K. G., Fowler, M. G., Li, M. W., and Snowdon, L. R. (2004). "Variable Alteration in Heavy Crude Oils of West-Central Saskatchewan, Canada." Organic Geochemistry, 35(4), 469-491.

Osacky, M., Geramian, M., Ivey, D. G., Liu, Q., and Etsell, T. H. (2013). "Mineralogical and Chemical Composition of Petrologic End Members of Alberta Oil Sands." Fuel, 113, 148-157.

Puri, V. K. (2000). "Geotechnical Aspects of Oil-Contaminated Sands." Soil & Sediment Contamination, 9(4), 359-374.

Raicar, M., and Procter, R. M. "Economic Considerations and Potential of Heavy Oil Supply from Lloydminster, Alberta, Canada." Unitar by McGraw-Hill Inc, Coal Age Mining Information Services, 212-219.

Raisbeck, J. M., and Currie, J. B. (1981). "A Laboratory Investigation of Hydraulic Fracturing in Oil Sands." In Situ, 5(1), 1-24.

Samieh, A. M., and Wong, R. C. K. (1997). "Deformation of Athabasca Oil Sand at Low Effective Stresses under Varying Boundary Conditions." Canadian Geotechnical Journal, 34(6), 985-990.

Santamarina, J. C., Klein, K. A., and Fam, M. A. (2001). Soils and Waves - Particulate Materials Behavior, Characterization and Process Monitoring, John Whiley and Sons, LTD.

Shafiei, A., and Dusseault, M. B. (2013). "Geomechanics of Thermal Viscous Oil Production in Sandstones." Journal of Petroleum Science and Engineering, 103, 121-139.

Somerton, W. H. (1974). "Thermal Behavior of Unconsolidated Oil Sands." Society of Petroleum Engineers Journal, 14, 513-521.

Takamura, K. (1982). "Microscopic Structure of Athabasca Oil Sand." Canadian Journal of Chemical Engineering, 60(4), 538-545.

Tosaya, C., Nur, A., and Vo-Thanh, D. (1987). "Laboratory Seismic Methods for Remote Monitoring of Thermal EOR." SPE Reservoir Engineering, 2, 235-242.

Tosaya, C. A., DaPrat, G., and Nur, A. M. (1984). "Monitoring of Thermal EOR Fronts by Seismic Methods." 179.

Wang, Z., and Nur, A. (1988b). "Effect of Temperature on Wave Velocities in Sands and Sandstones with Heavy Hydrocarbons." SEG Technical Program Expanded Abstracts 1986, 3-5.

Wang, Z., and Nur, A. (1990). "Wave Velocities in Hydrocarbon-Saturated Rocks - Experimental Results." Geophysics, 55(6), 723-733.

Wong, R. C. K. (1999). "Mobilized Strength Components of Athabasca Oil Sand in Triaxial Compression." Canadian Geotechnical Journal, 36(4), 718-735.

Wong, R. C. K. (2000). "Shear Deformation of Locked Sand in Triaxial Compression." Geotechnical Testing Journal, 23(2), 158-170.

Wong, R. C. K. (2001). "Strength of Two Structured Soils in Triaxial Compression." International Journal for Numerical and Analytical Methods in Geomechanics, 25(2), 131-153.

Wong, R. C. K., and Yeung, K. C. (2002). "Borehole Stability in Oil Sands under Drilling." Journal of Canadian Petroleum Technology, 41(1), 55-60.

Zhao, R. B., Tang, G. Q., and Kovscek, A. R. (2013). "Modification of Heavy-Oil Rheology Via Alkaline Solutions." Journal of Petroleum Science and Engineering, 103, 41-50.

Zimmerman, R. W. (1989). "Thermal Conductivity of Fluid-Saturated Rocks." Journal of Petroleum Science and Engineering, 3, 219-227.

CHAPTER 6

ENHANCED RESOURCE RECOVERY: HYDRAULIC FRACTURE IN PRE-STRUCTURED MEDIA

6.1. INTRODUCTION

Hydraulic fracturing is commonly used to enhance resource recovery in oil, gas, water, and geothermal reservoirs (Yuster and Calhoun, 1945; Clark, 1949; Solberg et al., 1980; Holditch et al., 1990; Jeffrey et al., 1998; Palmer et al., 2007), for deep waste injection (Delaguna, 1966; Dusseault, 1995), and to assess in-situ state of stress (Kehle, 1964; Haimson and Fairhurst, 1969).

Extensive experimental, analytical and numerical studies have been conducted to understand the evolution of hydraulic fractures in various geomaterials. Previous studies can be categorized into four main groups. Hydraulic fractures in homogeneous, continuous media are planar discontinuities that propagate normal to the least principal stress direction (Table 6.1 - Category #1); the fluid pressure required to create these fractures is determined by the medium's tensile strength. In uncemented sediments with no tensile strength, hydraulic fractures are controlled by the effective stress-dependent frictional strength (Table 6.1 - Category #2); these opening-mode discontinuities result from the balance between skeletal forces induced by the far field effective stress, viscous drag and capillary forces. Propagating fluid-driven fractures, in the third group, interact with pre-existing fractures. Most studies have focused on homogenous media with a single pre-existing fracture, which is subjected to hydraulic fracturing.

Table 6.1. Previous studies on hydraulic fracture – Conditions and assumptions

	(1) Cohesive, intact rocks	(2) Uncemented sediments (d << L)	(3) Sporadically fractured rocks	(4) Pre-structured rocks (S ≈ L)
Schematic	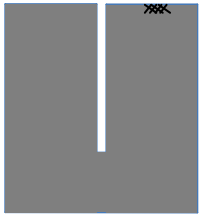	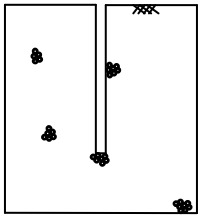	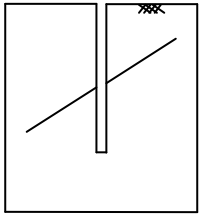	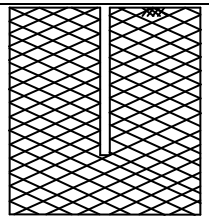
Dominant Behavior	Tensile failure (LEFM)	Particle-scale interactions (effective stress-dependent)	HF and natural fracture interact (arrest, jog, cross, diversion)	Kinematically-controlled dilational distortion
References	Griffith, 1921 Sneddon, 1946 Harrison et al., 1954 Irwin, 1957 Hubbert and Willis, 1957 Perkins and Kern, 1961 Haimson and Fairhurst, 1969 Settari and Cleary, 1984 De Pater et al., 1994 Wang et al., 1994 Yew, 1997 Economides, 2000 Zhang et al., 2005 Economides et al., 2007 Wu et al., 2007	Bjerrum et al., 1972 Dusseault, 1988 Atkinson et al., 1994 Soga et al., 2006 Shin and Santamarina, 2010 Holtzman et al., 2012	Lamont and Jessen, 1963 Daneshy, 1974 Zoback et al., 1977 Warpinski et al., 1982 Lam and Cleary, 1984 Teufel and Clark, 1984 Blanton, 1986 Blair et al., 1990 Heuze et al., 1990 Renshaw and Pollard, 1995 Potluri et al., 2005 Adachi et al., 2007 Zhou et al., 2008 Akulich and Zvyagin, 2008 Zhang et al., 2009 Rahman et al., 2010 Chuprakov et al., 2011	Batchelor and Pine, 1984 Warpinski and Teufel, 1987 Dusseault, 1988 Harper and Last, 1990 Last and Harper, 1990 Britt et al., 1994 Kohl and Hopkirk, 1995 Bhasin and Hoeg, 1998 Beugelsdijk et al., 2000 Chen et al., 2000 Kulatilake et al., 2001 Rutqvist and Stephansson, 2003 De Pater and Beugelsdijk, 2005 Jeffrey et al., 2010 Dusseault, 2011

Notation. d: grain size. S: preexisting fracture separation. L: hydraulic fracture length

Results show that the interaction depends on factors such as the fractures' approach angle, in-situ state of stress, rock toughness, joint friction and aperture, injection rate/pressure and fluid viscosity (Table 6.1 - Category #3).

Hydraulic fracture formation and growth in pre-structured (blocky) media remains less understood (Table 6.1 - category #4). Fracture mapping techniques reveal that in most cases of fully-fractured subsurface rock masses, there are three sets of mutually perpendicular joints to the extent that a fully, blocky medium is formed (Figure 6.1).

Figure 6.1. Black Canyon of the Gunnison National Park, Colorado (www.terragalleria.com). Also refer to NRC, 1996.

Microseismicity reveals the strong influence of pre-existing fractures on the complex propagation of hydraulic fractures and the development of multiple branches in subsurface pre-structured media. Multistage fracturing has been developed as an attempt to optimize the stimulation processes in such complex media (Warpinski et al., 2009;

Maxwell et al., 2011; Mayerhofer et al., 2011). Clearly, the generation and propagation of hydraulic fractures in a pre-structured medium must reflect the coupling between the mechanical and hydraulic characteristics of the medium (e.g., joint pattern; opening-dependent fluid conductivity; block rotation/slippage/interlocking, and shear dilation), the in-situ state of stresses and stress anisotropy.

The purpose of this study is to investigate the response of pre-structured blocky media subjected to the generation of an open-mode discontinuity and the implications on the surrounding medium. The study combines experiments and analytical solutions.

6.2. EXPERIMENTAL STUDY AND RESULTS

An experimental study was designed to explore the response of a tightly packed (low-porosity), blocky medium to an imposed disturbance. The pre-structured medium is modeled experimentally as an assemblage of impermeable, equal-size Acrylic blocks (size of 25.4×13×13 mm – Figure 6.2.b). Assemblages are formed with two different internal structures specified by overlap ratios of 50% and 90%, which is defined as the percentage by which a block in the layer above covers a block vertically below (Figure 6.2.a).

6.2.1. Boundary Conditions

The blocky medium is packed between two rigid plates to simulate plane-strain conditions $\varepsilon_y=0$. A parallel series of tests are conducted with either stress-free $\sigma_x=0$ to simulate shallow and less constrained formations or fixed $\varepsilon_x=0$ lateral boundary conditions to simulate deep and tight formations. The top boundary is free in all cases $\varepsilon_z>0$.

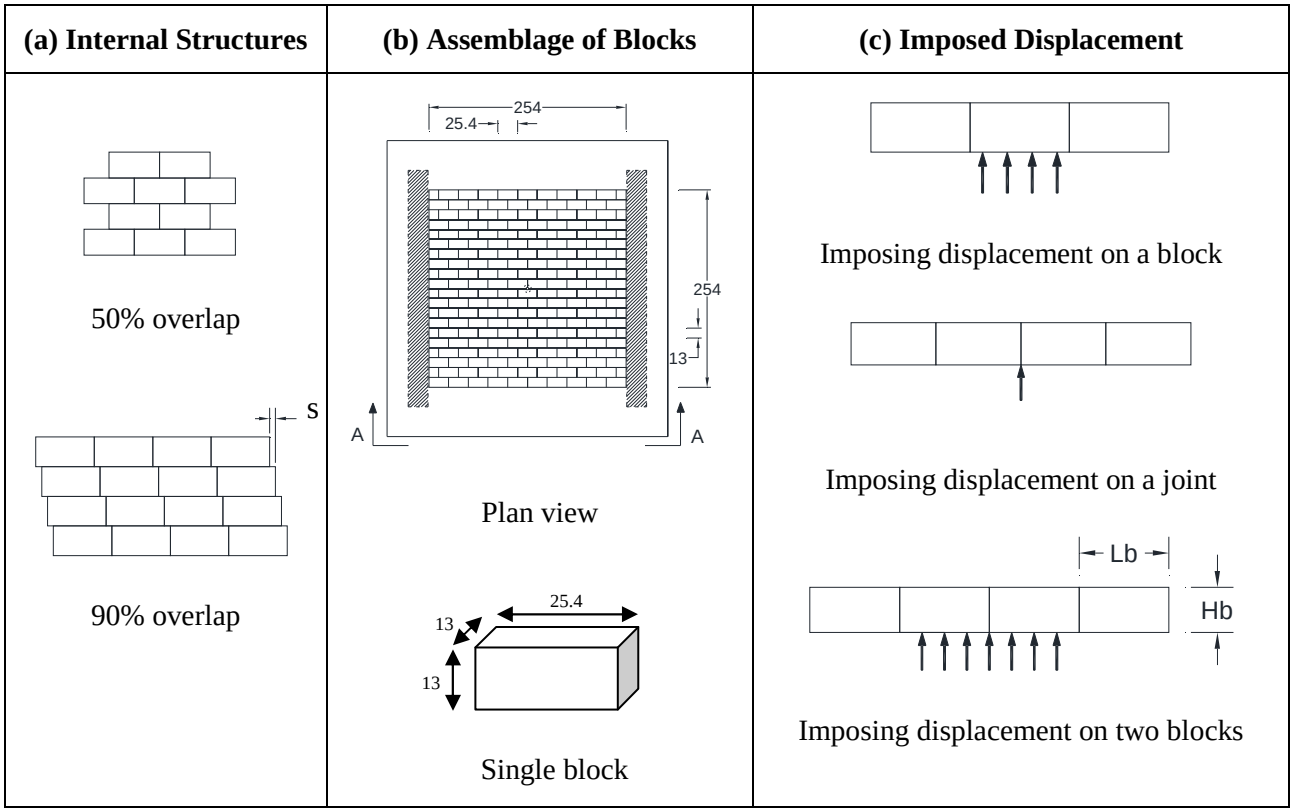

Figure 6.2. Experimental study. (a) Tested internal structures. (b) Assemblage of blocks. (c) Imposed displacement. Note: all dimensions are in millimeters.

6.2.2. Monitoring

High-resolution time-lapse photography is used to record the displacement field as observed through the transparent front plate (Plexiglas). In addition, we record the exerted force with respect to each level of imposed displacement on two blocks at the lower boundary (Figure 6.2.c). An open-mode discontinuity is generated by displacing two blocks at the very bottom row upwards. Images are made during loading and unloading of blocky media with two different internal structures (50% and 90% inter-block overlap), and fixed and free lateral boundary conditions are shown in Figure 6.3.

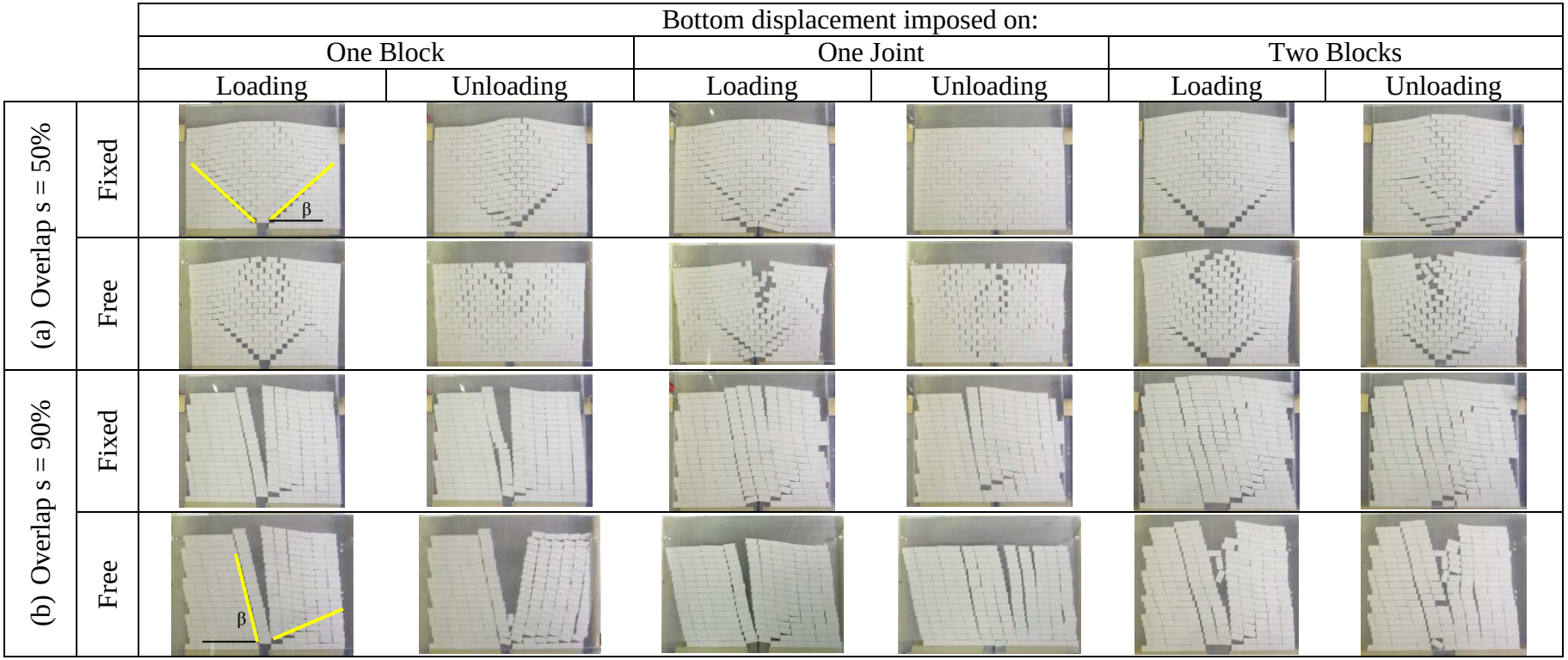

Figure 6.3. Experimental study – Imposed displacement tests (set #2). Observed dilational distortion during loading and unloading for various cases of imposed displacement: on a block, on a joint, or on two blocks. Results are shown for two internal structures, with either 50% or 90% overlap, under fixed and free lateral boundary conditions.

The blocky mass experiences dilational distortion away from the imposed displacement at the lower boundary. The propagation of the perturbation is intimately related to the pattern of the internal structure, resulting in marked “wing” openings that propagate upwards at angles that reflect the structure of the blocky medium and boundary conditions; in particular, columnar structures form when there is a large overlap between blocks. Far-field distortion occurs mostly within the area enclosed by the wing openings (Figure 6.3).

Irreversible residual deformations remain locked-in upon unloading (documented in Figure 6.3 – images in unloading column). This form of “self-propping” is caused by blocks that slip under neighboring blocks i.e., *kinematic propping*, or frictionally trapped block misalignment, i.e., *static propping*. The efficiency of proppant-free or waterfrac field treatments confirms self-propping effects following dilation being recognized as mobilization of Coloumbian shear resistance in the past (Mayerhofer et al., 1997; Chen et al., 2000; Hossain et al., 2002). Results obtained in this study show that even without mobilization of Coloumbian shear resistance, the blocky medium dilates by kinematic or static self-propping.

The block displacement δ_i in successive i-th layers away from the “main fracture,” is normalized by the first layer displacement δ_o, “the imposed displacement,” and plotted versus the layer number $i = z_i/H_b$ in Figure 6.4. The increase in vertical displacement reflects the cumulative effects of kinematic dilation. The dilational distortion is diminished at high stress due to block and joint deformations. Block splitting and corner crushing will hinder dilation as well. Figure 6.5 shows the results of numerical

simulations (conducted by Hosung Shin) for dilational distortion at different stress levels and stress field inside the blocks.

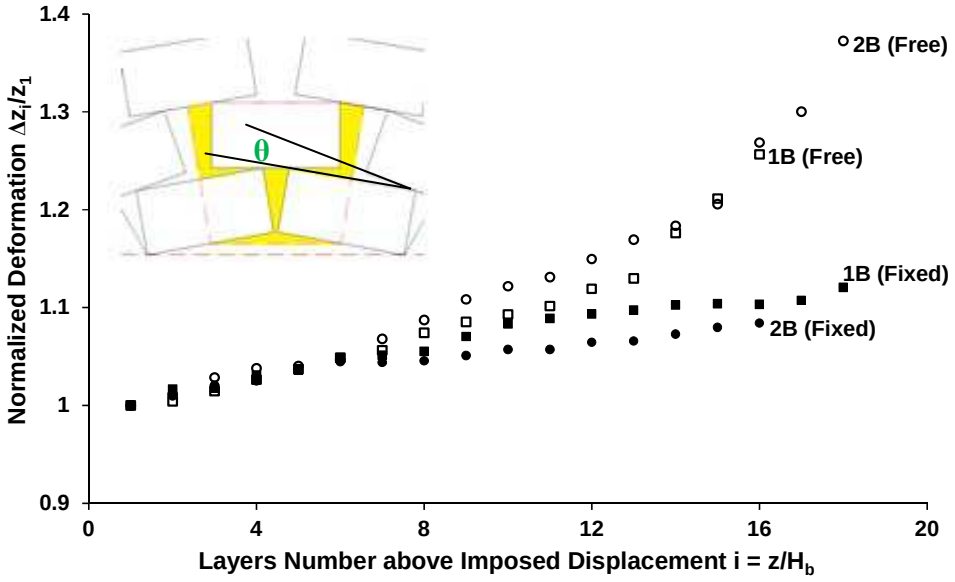

Figure 6.4. Experimental results. Layer displacement normalized by the displacement of the main fracture opening versus layer number above imposed displacement – conditions: displacement imposed on one block "b" or two blocks "2b" under either free or fixed lateral boundaries.

Force-displacement data collected during these tests show a hysteretic, elasto-plastic response (Figure 6.6). The force required to displace a single block is 5-to-10 times the overburden weight above the element depending on the pattern of internal structure of the blocky medium. Higher values apply to 50% overlap and zero lateral strain boundary conditions due to higher potential of interlocking.

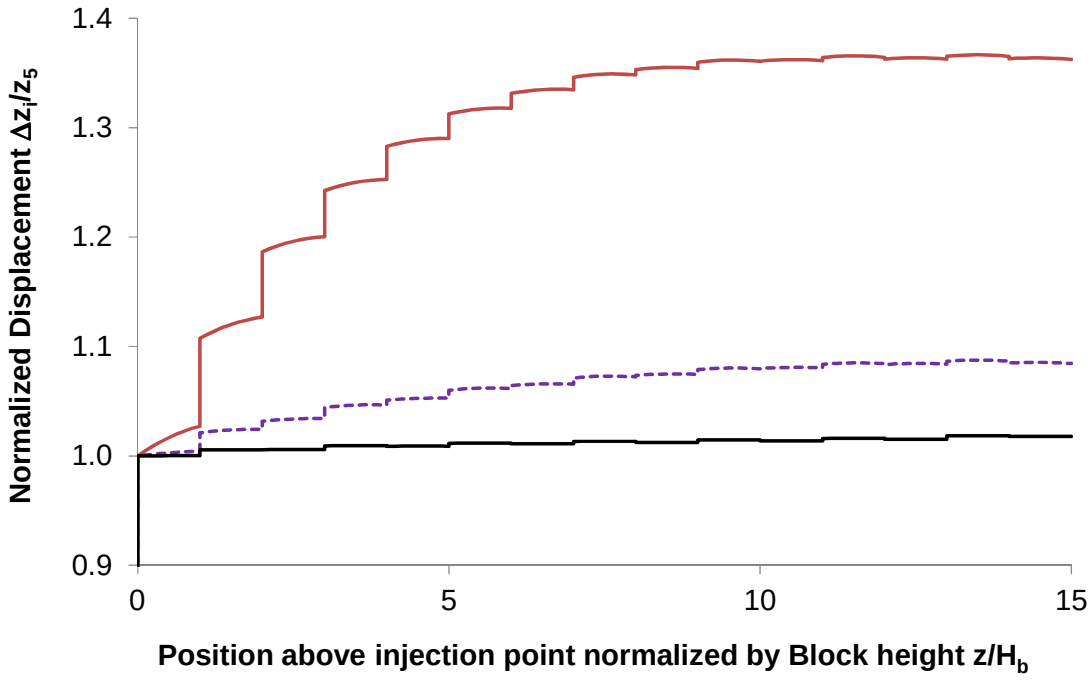

(a)

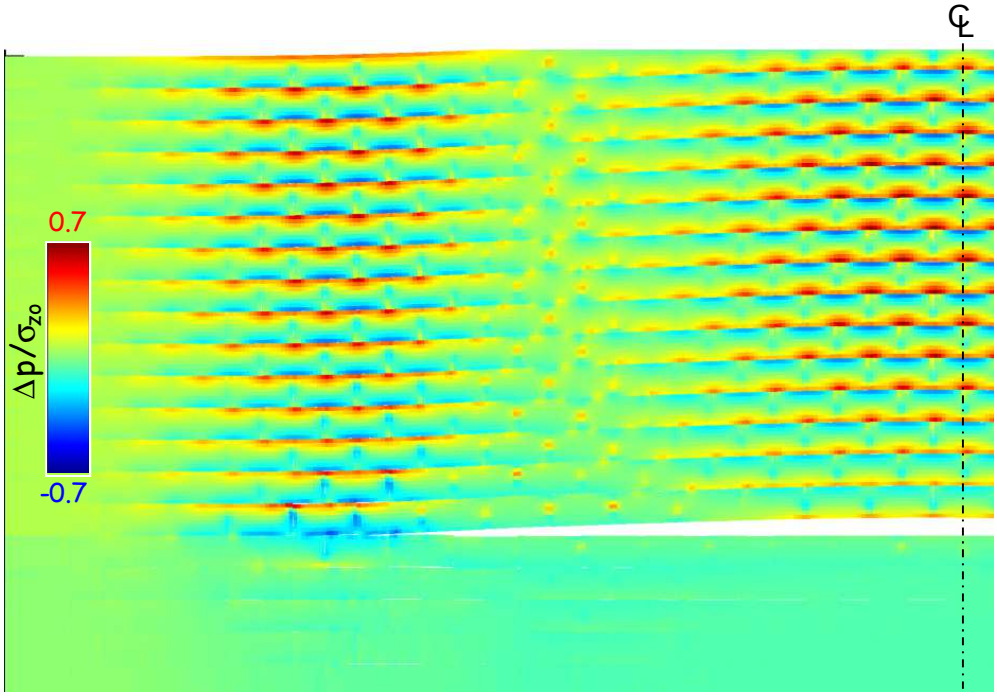

(b)

Figure 6.5. Dilational distortion at different stress levels and stress field. (a) Layer displacement normalized by the displacement at the fracture wall versus layer number above injection point. (b) Change in induced mean stress inside blocks-red: compression. blue: tension. Simulation by: Hosung Shin

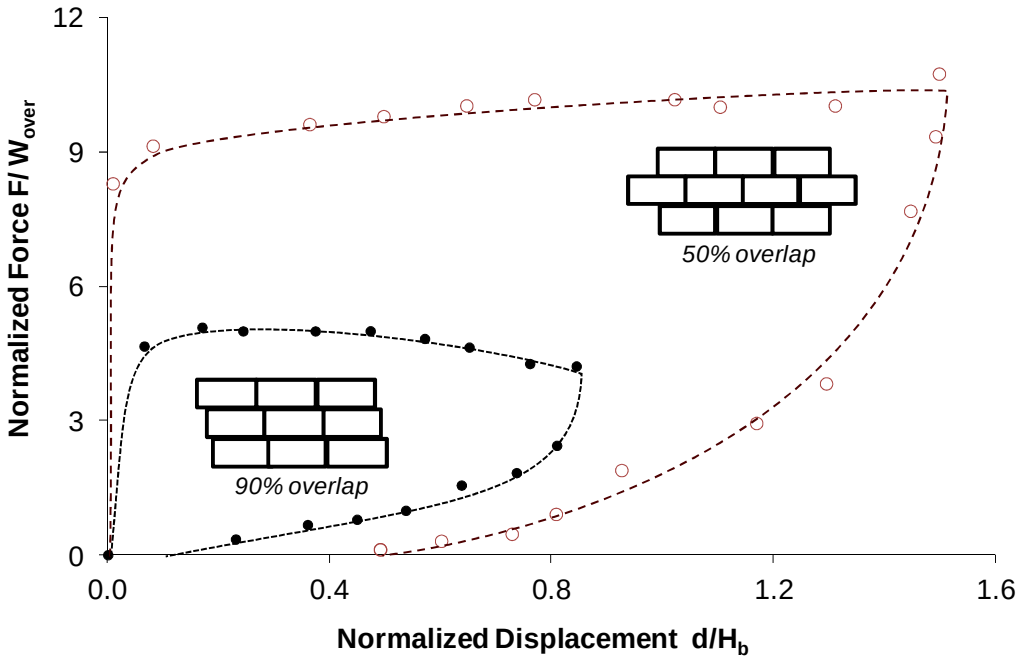

Figure 6.6. Experimental results. Force imposed to displace one block about one block height normalized by the weight of the overburden above that block versus imposed displacement normalized by the block height H_b.

6.3. ANALYSES AND DISCUSSION

The regular fabric of pre-structured media lends itself to simple geometrical analyses that provide unique insight into the evolution of the formation during the generation of opening-mode discontinuities. The inclinations of wing openings β with respect to the horizontal orientation in the counterclockwise direction can be expressed as a function of block slenderness $\lambda=L_b/H_b$ and overlap ratio s/L_b (Figure 6.3),

$$\beta = \arctan\left[\lambda\left(1-\frac{s}{L_b}\right)\right]^{-1} \tag{6.1}$$

The wing angle is β=45° for the internal structure with overlap ratio s/L_b=0.5, and β=79° for overlap ratio s/L_b=0.9. Wing openings can be major conduits for fluid transport into the main fracture and then to the production well.

As layers bend around the main fracture, changes in local porosity Δn are related to the relative rotation angle θ [rad] between contiguous blocks (Inset in Figure 6.4). A Taylor expansion of the geometric solution predicts that $\Delta n \approx 2\theta/\text{rad}$; hence, a relative rotation of $\theta \cong 1°$ corresponds to an increase in local porosity of Δn=3.5% in a blocky structure with overlap ratio s/L_b=0.5 and block slenderness $\lambda = L_b/H_b = 2$.

Fractures in situ involve a large number of blocks, $L_F/L_b >> 1$. The average joint aperture e for joints normal to the main fracture is a function of the main fracture opening O_F and the fracture length L_F; assuming a Pythagorean geometry (Figure 6.7):

$$e = \frac{\Delta L}{N} = \frac{\sqrt{L_F^2 + O_F^2} - L_F}{\frac{L_F}{L_b}} = L_b\left(\sqrt{1+\left(\frac{O_F}{L_F}\right)^2} - 1\right) \approx \frac{L_b}{2}\left(\frac{O_F}{L_F}\right)^2 \qquad (6.2)$$

The height and width of these discrete openings between the blocks in contiguous rows are at least equal to the height and the width of the blocks (H_b).

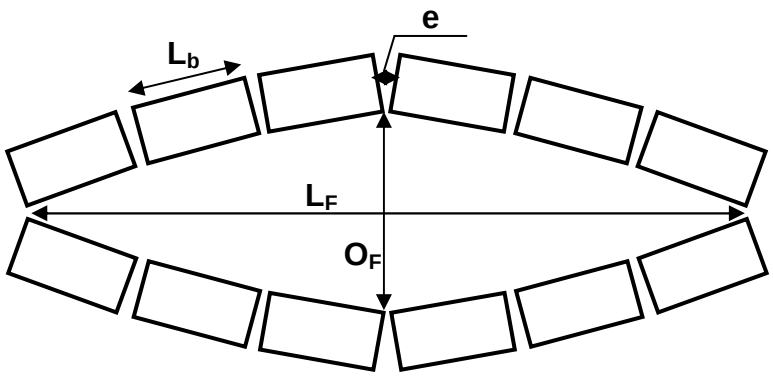

Figure 6.7. Main and discrete opening between blocks.

Consider a long fracture length L_F = 20 m that has opened O_F = 0.2 m: on average, transverse joints will open 0.1 mm when blocks are L_b = 1 m long.

The opening of joints associated to block rotation or fracture-induced extensions have a pronounced effect on fluid conductivity. The fluid conductivity K [m/s] of a jointed rock mass with joint aperture e [m] and spacing L_b [m] traversed by a fluid with unit weight γ [kN/m^3] and viscosity η [Pa.s] can be estimated as (Snow, 1965):

$$K = \frac{\gamma e^3}{6\eta L_b} \tag{6.3}$$

Combining Equations 6.2 and 6.3, the conductivity of transverse joints is strongly affected by the geometry of the main fracture O_F/L_F:

$$K = \frac{\gamma L_b^2}{48\eta}\left(\frac{O_F}{L_F}\right)^6 \tag{6.4}$$

6.4. CONCLUSIONS

High-pressure fluid injection in pre-structured media can cause opening-mode discontinuities that are distinct from hydraulic fractures in homogeneous cohesive or granular media. In particular:

- The distortion of the surrounding medium creates extensive dilation around the discontinuity; the dilation decreases at high stress due to block deformation, splitting, or edge crushing.
- The response of the pre-structured medium to the opening-mode discontinuity is strongly affected by its internal structure characterized by geometric parameters such as block size, slenderness and overlap length.

- Kinematically-controlled dilational distortion has a significant effect on the fluid conductivity in the pre-structured medium. A six-power relationship is anticipated between the enhanced conductivity and the inverse of the main fracture slenderness.
- Frictional self-propping locks in dilational distortion and maintains high conductivity after depressurization. Self-propping develops more readily when the main fracture has low slenderness.
- The injection pressure to create an opening-mode discontinuity in a pre-structured medium is internal structure dependent, and it can be much higher than the overburden stress due to the mobilization of high shear resistance and dilation.

6.5. REFERENCES

Adachi, J., Siebrits, E., Peirce, A., and Desroches, J. (2007). "Computer Simulation of Hydraulic Fractures." International Journal of Rock Mechanics and Mining Sciences, 44, 739-757.

Akulich, A. V., and Zvyagin, A. V. (2008). "Interaction between Hydraulic and Natural Fractures." Fluid Dynamics, 43(3), 428-435.

Atkinson, J. H., Charles, J. A., Mhach, H. K., and Icsmfe (1994). Undrained Hydraulic Fracture in Cavity Expansion Tests.

Batchelor, A. S., and Pine, R. J. (1984). "Downward Migration of Shearing in Jointed Rock during Hydraulic Injections." International Journal of Rock Mechanics and Mining Sciences and, 21(5), 249-263.

Beugelsdijk, L. J. L., De Pater, C. J., and Sato, K. "Experimental Hydraulic Fracture Propagation in a Multi-Fractured Medium." 177-184.

Bhasin, R., and Hoeg, K. (1998). "Numerical Modelling of Block Size Effects and Influence of Joint Properties in Multiply Jointed Rock (Reprinted from Tunnelling and Underground Space Technology, Vol 12, 1997)." Tunnelling and Underground Space Technology, 13(2), 181-188.

Bjerrum, L., Kennard, R. M., Gibson, R. E., and Nash, J. (1972). "Hydraulic Fracturing in Field Permeability Testing." Geotechnique, 22(2), 319-&.

Blair, S. C., Thorpe, R. K., and Heuze, F. E. (1990). "Propagation of Fluid-Driven Fractures in Jointed Rock - Part 2. Physical Tests on Blocks with an Interface or Lens." International Journal of Rock Mechanics and Mining Sciences & Geomechanics Abstracts, 27(4), 255-268.

Blanton, T. L. (1986). "Propagation of Hydraulically and Dynamically Induced Fractures in Naturally Fractured Reservoirs." International Society of Petroleum Engineers, SPE15261, 613-627.

Britt, L. K., Thompson, J. W., and Hager, C. J. (1994). "Hydraulic Fracturing in a Naturally Fractured Reservoir." Proceedings of the Annual Southwestern Petroleum Short Course(42), 278.

Chen, Z., Narayan, S. P., Yang, Z., and Rahman, S. S. (2000). "An Experimental Investigation of Hydraulic Behaviour of Fractures and Joints in Granitic Rock." International Journal of Rock Mechanics and Mining Sciences, 37(7), 1061-1071.

Chuprakov, D. A., Akulich, A. V., Siebrits, E., and Thiercelin, M. (2011). "Hydraulic-Fracture Propagation in a Naturally Fractured Reservoir." Spe Production & Operations, 26(1), 88-97.

Clark, J. B. (1949). "A Hydraulic Process for Increasing the Productivity of Wells." Transactions of the American Institute of Mining and Metallurgical Engineers, 186(1), 1-8.

Daneshy, A. (1974). "Hydraulic Fracture Propagation in Presence of Planes of Weakness." Journal of Petroleum Technology, 26(MAR), 304-304.

De Pater, C. J., and Beugelsdijk, L. J. L. "Experiments and Numerical Simulation of Hydraulic Fracturing in Naturally Fractured Rock." ARMA, ARMA/NARMS05-780.

De Pater, C. J., Cleary, M. P., Quinn, T. S., Barr, D. T., Johnson, D. E., and Weijers, L. (1994). "Experimental Verification of Dimensional Analysis for Hydraulic Fracturing." Spe Production & Facilities, 9(4), 230-238.

Delaguna, W. (1966). "Disposal of Radioactive Wastes by Hydraulic Fracturing. 2-Mechanics of Fracture Formation and Design of Observation and Monitoring Wells." Nuclear Engineering and Design, 3(3), 432-&.

Dusseault, M. B. (1995). "Radioactive Waste Disposal." Nature, 375(6533), 625-625.

Dusseault, M. B. (2011). "Geomechanical Challenges in Petroleum Reservoir Exploitation." Ksce Journal of Civil Engineering, 15(4), 669-678.

Economides, M. J. (2000). "Reservoir Stimulation." 3rd ed., Chichester, England.

Economides, M. J., Mikhailov, D., and Nikolaevskiy, V. (2007). "On the Problem of Fluid Leakoff during Hydraulic Fracturing." Transport in Porous Media, 67(3), 487.

Griffith, A. A. (1921). "The Phenomena of Rupture and Flow in Solids." Philosophical Transactions of the Royal Society of London. Series A, Containing Papers of a Mathematical or Physical Character, 221, 163-198.

Haimson, B., and Fairhurst, C. (1969). "Hydraulic Fracturing in Porous Permeable Materials." Journal of Petroleum Technology, 21(JUL), 811-&.

Haimson, B., and Fairhurst, C. (1969). "In-Situ Stress Determination at Great Depth by Means of Hydraulic Fracturing." 559.

Harper, T. R., and Last, N. C. (1990). "Response of Fractured Rock Subject to Fluid Injection. 2. Characteristic Behavior." Tectonophysics, 172(1-2), 33-51.

Harrison, E., Kieschnick, W. F., and McGuire, W. J. (1954). "The Mechanics of Fracture Induction and Extension." Transactions of the American Institute of Mining and Metallurgical Engineers, 201, 252-263.

Heuze, F. E., Shaffer, R. J., Ingraffea, A. R., and Nilson, R. H. (1990). "Propagation of Fluid-Driven Fractures in Jointed Rock.1. Development and Validation of Methods of Analysis." International Journal of Rock Mechanics and Mining Sciences & Geomechanics Abstracts, 27(4), 243-245.

Holditch, S. A., Ely, J. W., Semmelbeck, M. E., Carter, R. H., Hinkel, J. J., and Jeffrey, R. G. (1990). "Hydraulic Fracturing Accelerates Coalbed Methane Recovery." World Oil, 211(5), 41-45.

Holtzman, R., Szulczewski, M. L., and Juanes, R. (2012). "Capillary Fracturing in Granular Media." Physical Review Letters, 108(26), 264504.

Hossain, M. M., Rahman, M. K., and Rahman, S. S. (2002). "A Shear Dilation Stimulation Model for Production Enhancement From Naturally Fractured Reservoirs." SPE Journal, 7(2), 183-195.

Hubbert, M. K., and Willis, D. G. (1957). "Mechanics of Hydraulic Fracturing." Transactions of the American Institute of Mining and Metallurgical Engineers, 210(6), 153-163.

Irwin, G. R. (1957). "Analysis of Stresses and Strains Near the End of a Crack Traversing a Plate." R. J. Sanford, and B. J. Thompson, eds., United States, SPIE- The International Society for Optical Engineering, 167-170.

Jeffrey, R. G., Wold, M. B., Choi, S. K., and Settari, A. (1998). "Stimulation for Methane-Gas Recovery from Coal." SPE Production and Facilities, 13(3), 200-207.

Jeffrey, R. G., Zhang, X., and Bunger, A. P. (2010). "Hydraulic Fracturing of Naturally Fractured Reservoirs." Stanford CA, Stanford Geothermal Program, 289-297.

Kehle, R. O. (1964). "Determination of Tectonic Stresses through Analysis of Hydraulic Well Fracturing." Journal of Geophysical Research, 69(2), 259-&.

Kohl, T., and Hopkirk, R. J. (1995). ""“FRACture” - A Simulation Code for Forced Fluid Flow and Transport in Fractured, Porous Rock." Geothermics, 24(3), 333-343.

Kulatilake, P. H. S. W., Malama, B., and Wang, J. (2001). "Physical and Particle Flow Modeling of Jointed Rock Block Behavior under Uniaxial Loading." International Journal of Rock Mechanics and Mining Sciences, 38(5), 641-657.

Lam, K. Y., and Cleary, M. P. (1984). "Slippage and Re-Initiation of (Hydraulic) Fractures at Frictional Interfaces." International Journal for Numerical and Analytical Methods in Geomechanics, 8(6), 589-604.

Lamont, N., and Jessen, F. W. (1963). "The Effects of Existing Fractures in Rocks on the Extension of Hydraulic Fractures." Transactions of the Society of Petroleum Engineers of Aime, 228(2), 203-209.

Last, N. C., and Harper, T. R. (1990). "Response of Fractured Rock Subject to Fluid Injection. 1. Development of a Numerical Model." Tectonophysics, 172(1-2), 1-31.

Maxwell, S. C., Cho, D., Pope, T., Jones, M., Cipolla, C., Mack, M., Henery, F., Norton, M., and Leonard, J. (2011). "Enhanced Reservoir Characterization Using Hydraulic Fracture Microseismicity." SPE Hydraulic Fracturing Technology Conference and Exhibition,Woodlands, Texas, USA, 457-467.

Mayerhofer, M. J., Richardson, M. F., Walker Jr, R. N., Meehan, D. N., Oehler, M. W., and Browning Jr, R. R. "Proppants? We Don't Need No Proppants." 457-464.

Mayerhofer, M. J., Stegent, N. A., Barth, J. O., and Ryan, K. M. (2011). "Integrating Fracture Diagnostics and Engineering Data in the Marcellus Shale." SPE Annual Technical Conference and Exhibition,Denver, Colorado, USA, 518-532.

NRC (1996). Rock Fractures and Fluid Flow:Contemporary Understanding and Applications, The National Academies Press.

Palmer, I., Moschovidis, Z., and Cameron, J. (2007). "Modeling Shear Failure and Stimulation of the Barnett Shale after Hydraulic Fracturing." SPE Annual Technical Conference and Exhibition,College Station, Texas, USA, 279-287.

Perkins, T. K., and Kern, L. R. (1961). "Widths of Hydraulic Fractures." Transactions of the Society of Petroleum Engineers of Aime, 222(9), 937-949.

Potluri, N., Zhu, D., and Hill, A. D. "Effect of Natural Fractures on Hydraulic Fracture Propagation." Richardson Tex, SPE International, 94568.

Rahman, M. M., Aghighi, M. A., Seikh, A. R., and Syed, A. H. (2010). "Effect of Natural Fracture on Hydraulic Fracture Propagation in Naturally Fractured Geothermal Reservoirs." The World Geothermal CongressBali, Indonesia.

Renshaw, C. E., and Pollard, D. D. (1995). "An Experimentally Verified Criterion for Propagation across Unbounded Frictional Interfaces in Brittle, Linear Elastic Materials." International Journal of Rock Mechanics and Mining Sciences and Geomechanics Abstracts, 32, 237-249.

Rutqvist, J., and Stephansson, O. (2003). "The Role of Hydromechanical Coupling in Fractured Rock Engineering." Hydrogeology Journal, 11(1), 7-40.

Settari, A., and Cleary, M. P. (1984). "3-Dimensional Simulation of Hydraulic Fracturing." Journal of Petroleum Technology, 36(8), 1177-1190.

Shin, H., and Santamarina, J. C. (2010). "Fluid-Driven Fractures in Uncemented Sediments: Underlying Particle-Level Processes." Earth and Planetary Science Letters, 299(1-2), 180-189.

Sneddon, I. N. (1946). "The Distribution of Stress in the Neighbourhood of a Crack in an Elastic Solid." Proceedings of the Royal Society of London Series a-Mathematical and Physical Sciences, 187(1009), 229-260.

Snow, D. T. (1965). "A Parallel Plate Model of Fractured Permeable Media." Ph.D., University of California, Berkeley, California, U.S.A.

Soga, K., Gafar, K. O., Ng, M. Y. A., and Au, S. K. A. (2006). Macro and Micro Behaviour of Soil Fracturing.

Solberg, P., Lockner, D., and Byerlee, J. D. (1980). "Hydraulic Fracturing in Granite under Geothermal Conditions." International Journal of Rock Mechanics and Mining Sciences, 17(1), 25-33.

Teufel, L. W., and Clark, J. A. (1984). "Hydraulic Fracture Propagation in Layered Rock - Experimental Studies of Fracture Containment." Society of Petroleum Engineers Journal, 24(1), 19-32.

Wang, Y. L., Scott, J. D., and Dusseault, M. B. (1994). "Borehole Rupture from Plastic Yield to Hydraulic Fracture - A Nonlinear Model Including Elastoplasticity." Journal of Petroleum Science and Engineering, 12(2), 97-111.

Warpinski, N. R., Mayerhofer, M. J., Vincent, M. C., Cipolla, C. L., and Lolon, E. P. "Stimulating Unconventional Reservoirs: Maximizing Network Growth While Optimizing Fracture Conductivity." Richardson Tex, Society of Petroleum Engineers, SPE114173.

Warpinski, N. R., Schmidt, R. A., and Northrop, D. A. (1982). "In-situ Stresses -The Predominant Influence on Hydraulic Fracture Containment." Journal of Petroleum Technology, 34(3), 653-664.

Warpinski, N. R., and Teufel, L. W. (1987). "Influence of Geologic Discontinuities on Hydraulic Fracture Propagation." Journal of Petroleum Technology, 39(2), 209-220.

Wu, R., Germanovich, L. N., Van Dyke, P. E., and Lowell, R. P. (2007). "Thermal Technique for Controlling Hydraulic Fractures." Journal of Geophysical Research-Solid Earth, 112(B5).

Yew, C. H. (1997). Mechanics of Hydraulic Fracturing, Gulf Publishing Company, Houston, Texas.

Yuster, S. T., and Calhoun, J. C. (1945). "Pressure Parting of Formations in Water Flood Operations." The Oil Weekly, 117(2), 38-42.

Zhang, X., Jeffrey, R. G., and Detournay, E. (2005). "Propagation of a Hydraulic Fracture Parallel to a Free Surface." international Journal for Numerical and Analytical Methods in Geomechanics, 29(13), 1317-1340.

Zhang, X., Jeffrey, R. G., and Thiercelin, M. (2009). "Mechanics of Fluid-Driven Fracture Growth in Naturally Fractured Reservoirs with Simple Network Geometries." Journal of Geophysical Research-Solid Earth, 114.

Zhou, J., Chen, M., Jin, Y., and Zhang, G. (2008). "Analysis of Fracture Propagation Behavior and Fracture Geometry Using a Tri-Axial Fracturing System in Naturally Fractured Reservoirs." International Journal of Rock Mechanics and Mining Sciences, 45, 1143-1152.

Zoback, M. D., Rummel, F., Jung, R., and Raleigh, C. B. (1977). "Laboratory Hydraulic Fracturing Experiments in Intact and Pre-Fractured Rock." International Journal of Rock Mechanics and Mining Sciences, 14(2), 49-58.

CHAPTER 7
CONCLUSIONS

7.1. SALIENT CONCLUDING REMARKS

Various geomaterials can be involved in thermal energy geo-systems, in which they are subjected to high temperature and stress. In order to understand various geomaterials response to relevant excitations, series of experimental and analytical studies along with a data compilation were performed, in which some mechanical, thermal and hydraulic properties were investigated. The scope of this work has included:

1- Data mining and interpretation of stress- and temperature-dependency of the thermal conductivity of intact rocks.

2- Evolution of mid-strain stiffness and thermal conductivity of various dry granular materials with stress, grain material, and particle surface treatment.

3- Evolution of mid-strain stiffness and thermal conductivity of binary mixture of natural soils with grain size distribution, stress, and pore fluids.

4- Evolution of small- and mid-strain stiffnesses, and thermal conductivity of oil sands with stress and temperature,

5- Evolution of hydraulic conductivity of pre-structured media with fabric and stress.

The detailed conclusions are presented at the end of each chapter. The main conclusions directly influencing thermal energy geo-systems follow.

1- Many deep geothermal reservoirs and potential sealed repositories may include intact rocks and the thermal conductivity of these rock masses is a key parameter for their efficient selection and design. Data compiled from the literature suggest:

- The thermal conductivity of most rocks with crystalline micro-structure and tight macro-structure decreases with temperature that is associated to: (1) the generation of micro-cracks between the randomly distributed minerals (poly-minerallic) and the randomly oriented crystals (mono-minerallic) due to the differential thermal expansion of components, and (2) sharp decrease in the mean free path of heat carrying phonons upon temperature rise.
- The thermal conductivity of intact rocks is stress-sensitive despite their low porosity; however, it reaches to an asymptotic value at a characteristic stress level.

2- In order to engineer the materials used in thermal energy geo-storage systems, their hydraulic, mechanical and thermal responses should be evaluated for different applications. The evolution of thermal conductivity with stress for different granular materials suggests:

- Stress enlarges the inter-particle contact areas and increases the inter-particle coordination number so that the contact thermal resistance decreases and the number of heat pathways increases.
- The quality and number of inter-particle contacts are the controlling factors in the heat conductance through granular materials.
- While the particle density could significantly affect the thermal conductivity of granular materials, the variation of mass density is not a sufficient indicator of the variation of the thermal conductivity.
- Hollow, fine, and mono-sized particles made of amorphous materials at dry condition can provide a very low thermal conductivity that is not stress-sensitive

(however can be temperature-sensitive, i.e., the thermal conductivity of amorphous materials increases with temperature).

- Patchy particle surface coating by metallic material and the mismatch between the electronic and phononic heat conduction through metallic and non-metallic materials hinders the beneficial effect of metals as the most efficient heat conductors.
- Liquid-saturation provides the highest increase in the thermal conductivity of granular materials because the liquid decreases the contact thermal resistance sisgificantly by replacing the insulating air in particles surface imperfections. Other physical properties of pore-filling liquid must be selected carefully based on the imposed conditions in different applications.
- 20 to 40 percent fine content in binary mixtures (constant mineralogy) can provide the highest packing density and the highest thermal conductivity by providing higher number of inter-particle coordination number. However, the mid-strain stiffness increases monotonically with fine content.

3- Thermal and mechanical responses of oil sand reservoirs upon thermally enhanced oil recovery are important in the safety and design of the stimulation and production wells.

- The thermal conductivity of oil sand decreases with temperature because of the crystalline micro-structure of sand particles (quartz-dominant), i.e., the mean free path of heat carrying phonons decreases with temperature.

- Sand particles are oil-coated. The increase in the small-strain shear stiffness with temperature verifies this fact because the oil flows out and the mineral-to-mineral contact that is the controlling factor in small-strain stiffness gets improved.
- Mid-strain stiffness of oil sand, which is an indicator of fabric change and particle rearrangement behavior of the medium, is independent of the temperature (independent of the presence of the oil).
- Viscoelastic (time-dependent) response of the oil sand is independent of temperature (independent of the presence of the oil hence mineral-controlled).

4- Seismic subsurface mapping techniques show that in most shale gas and geothermal reservoirs (mostly granite), there are three sets of mutually perpendicular joints that make a fully blocky named as a pre-structured medium. The efficiency of fluid and heat recovery from such medium by means of hydraulically enhanced methods strongly depends on the geometric characteristics of its structure (fabric).

- Kinematically-controlled extensive dilational distortion away from the main hydraulically induced open-mode discontinuity is the unique deformational characteristic of a pre-structured medium, and it enhances the hydraulic conductivity of the medium significantly.
- The effect of dilational distortion can be suppressed at very high stresses because of the rock block deformations and breakage.

- The rock blocks in the stimulated volume frictionally lock-in part of the openings generated due to dilation, and it keeps the productivity continuous even after depressurization.
- The fluid injection pressure to generate the main open-mode discontinuity depends on the structure and it can be significantly (4-10 times) higher than the overburden stress.

7.2. RECOMMENDATIONS FOR FUTURE WORK

- Other physical properties of intact rocks must be explored similarly and be formulated because they all are interwoven with each other to determine the true response of geomaterials subjected to coupled thermo-hydro-chemo-mechanical excitations.
- Physical properties of other types of geomaterials including soils and fractured rocks must be documented at high temperature and stress, and physically-meaningful relationships must be developed because they all have applications in engineering solutions for modern energy-geosystems.

There are many parameters and processes affecting the physical properties of geomaterials, listed below, that must be investigated:

- The effect of pore fluid properties.
- The effect of grain size distribution and shape.
- The effect of constituent crystals structure and orientation.
- The effect of macro-structure of the geomaterial: intensity, distribution, orientation, spacing, surface features, formation mechanisms, filling material of micro-cracks, joints, and faults.

- The effect of thermal and chemical decomposition of minerals
- The residual effects of stress path during the formation history in the past and the imposed stress path by current operations/processes.
- The effect of cyclic heating and cooling in dry and wet conditions (relevant to cyclic thermally enhanced resource recovery and geothermal energy extraction)
- The effect of boundary conditions.
- Research about the effect of time, during which high temperature and high stresses persist, on geomaterials properties and responses.

Research about metamorphism processes. The nature has already produced new materials with new properties by heating and loading geomaterials in a very long time (includes creep effects).

APPENDIX A

OTHER THERMAL PROPERTIES OF GEOMATERIALS AT HIGH TEMPERATURE AND STRESS

A.1. HEAT CAPACITY

Heat capacity is a fundamental physical property that affects the storage and transfer of heat in geomaterials. It is defined as the first derivation of heat content with respect to temperature; hence, it shows the amount of heat required to increase the temperature of a unit mass of a substance (1 kg) by a unit temperature (1 K). Pure water, at 15 ˚C and atmospheric pressure, has a heat capacity as high as four times of common rocks (4.18 $kJ.kg^{-1}.K^{-1}$); hence, water-saturated rocks have much higher heat capacity than dry rocks. Heat capacity C_p is defined for either specific mass [$kJ.kg^{-1}.K^{-1}$] or specific volume [$kJ.m^{-3}.K^{-1}$]. The specific heat capacity at constant pressure and the specific heat capacity at constant volume for solids at room temperature are equal to within 1%.

Table A.1 indicates the heat capacity of common rocks. Heat capacity of rocks appears to be dependent on the ratio of silica to alumina content. The lower is this ratio in a rock the higher is the heat capacity of that rock (Somerton, 1992). The high iron content decreases the heat capacity of shale.

Major minerals of acidic and intermediate rocks, feldspar, quartz, pyroxenes, amphiboles, and mica, have specific heat capacities from 0.65 to 0.8 $kJ.kg^{-1}.K^{-1}$. Mafic rocks have higher specific heat capacities than felsic rocks. Carbonates and fluorite may

reach and exceed 0.9 $kJ.kg^{-1}.K^{-1}$. Opaque oxides have values close to typical silicates. Sulphide minerals have low values ranging from 0.2 to 0.55 $kJ.kg^{-1}.K^{-1}$ (Kukkonen and Lindberg, 1998).

One way to determine the heat capacity of rocks is to calculate it using Kopp's law. Based on Kopp's law, the heat content of any compound material equals sum of the heat contents of its constituent elements. Having the heat content of rock-forming minerals (Kelley, 1960) and their volumetric fractions in rocks, we may calculate the volumetric heat capacity of multi-component rocks. The other alternative is to have mass of each component and its specific heat capacity as follows:

$$C_P = \sum_{i=1}^{n} \frac{C_{Pi} M_i}{M_{tot}} \qquad \text{(A-1)}$$

For saturated rocks with one or more fluids, the heat capacity of constituent elements and their volumetric fractions are used to obtain the heat capacity of the compound material:

$$\rho_b C_P = (1-n)\rho_s C_{Ps} + n(S_1\rho_1 C_{P1} + S_2\rho_2 C_{P2} + ... + S_n\rho_n C_{Pn}) \qquad \text{(A-2)}$$

where the parameters are defined below:

ρ_b: Density of fluid-saturated rock [$kg.m^{-3}$]

C_P: Specific heat capacity of fluid-saturated rock [$kJ.kg^{-1}.K^{-1}$]

$C_V = \rho_b.C_P$: Volumetric specific heat capacity of fluid-saturated rock [$kJ.m^{-3}.K^{-1}$]

n: Porosity of rock (V_{void}/V_{Total})

ρ_s: Mass density of solid particles [$kg.m^{-3}$]

C_{Ps}: Specific heat capacity of solid particles [$kJ.kg^{-1}.K^{-1}$]

S_n: Degree of saturation of the n-th fluid ($V_{n\text{-th fluid}}/V_{void}$)

ρ_n: Mass density of the n-th fluid [$kg.m^{-3}$]

C_{Pn}: Specific heat capacity of the n-th fluid [$kJ.kg^{-1}.K^{-1}$]

Heat capacity values for solid rock and pore-filling fluids must be measured at in-situ conditions (elevated temperatures and pressures).

A.1.1. Techniques to Measure the Heat Capacity of Rocks

Heat content is measured by an appropriate calorimeter and then heat capacity is derived. In this technique, the specimen with known mass m_s [kg] is heated up to a certain temperature T_s [K] in a vessel filled with boiling water. Then the specimen is transported to the calorimeter that has a known heat capacity C_C = 0.07 $kJ.K^{-1}$, known amount of water m_w [kg] with temperature T_w [K] and specific heat capacity C_{Pw} = 4.18 $kJ.kg^{-1}.K^{-1}$. The specific heat capacity of the specimen C_{Ps} [$kJ.kg^{-1}.K^{-1}$] is obtained by measuring the equilibrium temperature T_e [K] that the water and specimen reach inside the calorimeter:

$$C_{Ps} = \frac{C_C + C_{Pw} m_w}{m_s} \frac{T_e - T_w}{T_s - T_e} \qquad \text{(A-3)}$$

This method has shown 5% uncertainty, which results from the heat loss when the specimen is transported. Some contamination is brought to the water from fine-grained material in the pores of a porous material (Kukkonen and Lindberg, 1998).

The heat capacity of soils and rocks is measured by heat pulse method (King and Somerton, 1960; Campbell et al., 1991; Kluitenberg et al., 1993). In this measuring technique, two probes, one containing a heating wire and the other containing a thermocouple or a thermistor, are inserted into two symmetrically drilled holes (about 6 mm apart) inside a cylindrical specimen. Both devices are thermally coupled with the specimen by means of a proper material. The heating wire heats the medium for a

specified amount of time (8 s) and the thermocouple measures the temperature evolution over time. A model for conduction of instantaneously imposed heat away from an infinitely long line source is used to infer the heat capacity of the medium (Carslaw and Jaeger, 1959). In reality, however, the heat source is cylindrical, has a finite length, and is applied in a short time. Other assumptions include: the geomaterial under testing is a homogeneous and isotropic medium, there is no thermal contact resistance between the medium and the needle probes, and the needles have infinitesimal heat capacity and infinitely large thermal conductivity.

The temperature T [˚C] evolution in radial space r [m] away from the heat source and over time t [s] can be stated as a function of the heat imposed q [J] to the medium per length of heating wire Q [$J.m^{-1}$], the thermal diffusivity D_T [$m^2.s^{-1}$], and the volumetric heat capacity of the medium C_V [$kJ.kg^{-1}.K^{-1}$] as follows.

$$T(r,t) = \frac{q}{4\pi D_T t}\exp\left(\frac{-r^2}{4D_T t}\right) \tag{A-4}$$

$$q = \frac{Q}{C_V} \tag{A-5}$$

Maximum temperature T_m occurs at a characteristic time $t_m=r^2/4D_T$:

$$T_m = \frac{q}{e\pi r^2} \tag{A-6}$$

Then the volumetric heat capacity is computed as following:

$$C_V = \frac{Q}{e\pi r^2 T_m} \tag{A-7}$$

Measurement precision of temperature, input heat and probe spacing determine the precision of calculated volumetric heat capacity. For example, 0.1 ˚C precision in

temperature measurement is required to achieve 1% precision in heat capacity (Kluitenberg et al., 1993).

For dry rocks, the heat content is measured by Bunsen-type calorimeter which employs the method of mixtures (Kelley, 1941). The measurement technique is based on a comparative method, in which the heat content of unknown specimen is measured relative to the known heat content of platinum specimen.

Heat flux differential scanning calorimetry is a technique, in which we can measure how much heat is required to increase the temperature of a testing specimen. Powdered specimens are prepared for heat capacity measurements by this technique to ensure a proper thermal contact with the measuring crucible. Mass of the specimen is known m (80 mg), heat flux dQ/dt and the rate of increasing temperature dT/dt are measured between the testing specimen and a standard specimen (sapphire), and then the heat capacity of the specimen is calculated as following (Hirono and Hamada, 2010):

$$mC_P \frac{dT}{dt} = \frac{dQ}{dt} \tag{A-8}$$

A.1.2. Heat Capacity of Intact Rocks vs. Temperature

Variation of heat capacity of simple substances with temperature was formulated by Debye (1914). The heat capacity of all minerals is temperature-dependent. For instance, the specific heat capacity of quartz and olivine increases 10-15% when the temperature changes from 25 to 100 ˚C (Kukkonen and Lindberg, 1998). Average increase in specific heat capacity is 28% for igneous rocks, 26% for metamorphic rocks and 25% for sedimentary rocks when the temperature increases from 0 ˚C to 300 ˚C (Vosteen and Schellschmidt, 2003).

The heat capacity of rocks is also temperature-dependent, and it increases with increasing temperature. One study shows that while specific heat capacity increases with increasing temperature, it peaks at 550 ˚C probably because of α-β phase transition of quartz and then decreases at temperatures beyond that (Hirono and Hamada, 2010). Another study shows 12% increase in the heat capacity of granite, granodiorite, diorite, basalt and granulite when the temperature increase from 25 to 100 ˚C (England, 1978). Figure A.1 indicates increase in heat capacity of some types of rocks with increasing temperature in dry condition. Usually, the increase in heat capacity of rocks with increasing temperature is captured by a linear relationship with respect to temperature rise $\Delta T = T - To$ [˚F] and the corresponding heat capacity at T_o [˚F], C_{Po} [$Btu.lb^{-1}.{}^{\circ}F^{-1}$]:

$$C_P = C_{Po} + \beta.\Delta T \tag{A-9}$$

The heat capacity of saturated rocks by one or more fluids also increases with increasing temperature. The heat capacity of water and methane increases with both pressure and temperature.

The density of water has been expressed as a function of temperature T [˚C], volumetric thermal expansion of water at specified temperature β_w, and its density at 20 ˚C, ρ_{w20} [$kg.m^{-3}$], as follows (Holman, 1958):

$$\frac{\rho_w}{\rho_{w20}} = \frac{1}{1 + (T - 20)\beta_w} \tag{A-10}$$

where the volumetric thermal expansion of water is also expressed as a function of temperature:

$$\beta_w = 2.115 \times 10^{-4} + 1.32 \times 10^{-6} T + 1.09 \times 10^{-8} T^2 \tag{A-11}$$

Two models have been developed to predict the variation of the heat capacity of water with temperature at two different temperature ranges:

For $20 < T < 290$: $\rho_w C_{Pw} = 1.0145 - 0.44\times10^{-3}T$ (A-12)

For $290 < T < 373$: $\rho_w C_{Pw} = 0.885e^{-[0.481\times10^{-2}(T-290)+0.234\times10^{-3}(T-290)^2]}$ (A-13)

Density of rock solids has been expressed similarly as a function of temperature assuming ρ_{s20}=2650 kg.m^{-3} (Somerton and Selim, 1961; Somerton, 1992):

$$\frac{\rho_s}{\rho_{s20}} = \frac{1}{1+(T-20)\beta_s} \quad \text{(A-14)}$$

$$\beta_s = \frac{0.5\times10^{-4}}{T} \quad \text{(A-15)}$$

One of the existing models for the heat capacity of rocks with respect to temperature is (Somerton, 1992):

$$C_{Ps} = 0.108\times T^{0.155} \quad \text{(A-16)}$$

Volumetric heat capacity of solid rock will be:

$$\rho_s C_{Ps} = \frac{0.286T^{0.155}}{1+0.5\times10^{-4}(T-20)} \quad \text{(A-17)}$$

Having $\rho_s C_{Ps}$, $\rho_w C_{Pw}$, $\rho_o C_{Po}$, porosity n and degree of saturation of each pore-filling fluid, S_w and S_o, we can calculate $\rho_b C_{Pb}$ of the bulk medium (ignoring the effect of air at high saturations).

Variation of specific heat capacity of several rock types with increasing temperature was fitted by a number of polynomial equations with slightly different fitting coefficients (Nabelek et al., 2012; Miao et al., 2014). The original form of this equation is called Maier-Kelly function (Richet, 2001):

$$C_P = a + bT + cT^{-2} + dT^{-0.5} \quad \text{(A-18)}$$

Where a [kJ.kg^{-1}.K^{-1}] is the specific heat capacity at T = 0 K. b, c and d are other fitting parameters that have been proposed for several rock types (Nabelek et al., 2012).

A.1.3. Heat Capacity of Intact Rocks vs. Stress

Mass specific heat capacity is insensitive to effective confining stress while volumetric specific heat capacity increases with increasing confinement depending on the compressibility of the rock structure (Somerton, 1992) because the heat capacity of rock-forming minerals is higher than that of the air.

A.2. THERMAL DIFFUSIVITY

The thermal diffusivity of any material shows how fast the heat is transferred inside a medium under transient condition. In other words, how fast the temperature of different points inside a medium changes over time.

One dimensional heat diffusion equation, or simply called heat equation, is derived using the continuity of heat equation and the equation of Fourier's heat conduction. Suppose a very long rod of a homogeneous material with cross-section area of A [m^2]. A temperature gradient has been imposed to the rod so that the temperature T(x,t) [K] of every point on the rod x_1 [m] changes with time t [s]. Heat contained in an infinitesimal volume A.Δx [m^3] of rod is obtained by the temperature of that section of rod and the volumetric heat capacity C_p [kJ.m^{-3}.K^{-1}] of the material (C_p.T.A.Δx). In a time interval dt [s], this heat contained in the volume A.Δx changes because of the change in temperature:

$$\Delta Q = C_p \frac{\partial T}{\partial t} A.\Delta x.dt \quad \text{(A-19)}$$

On the other hand, heat q.A.dt flows into the section Δx of rod and heat $A.dt[q+(\partial q/\partial x)\Delta x]$ flows out of it because the temperature changes over time and space. q [$W.m^{-2}$] is the heat flowing through unit area at unit time. Accumulation of heat in the finite volume of rod is:

$$\Delta Q = -A(\frac{\partial q}{\partial x})\Delta x.dt \quad \text{(A-20)}$$

Equating equations 1 and 2 because of conservation of heat in the infinitesimal volume $A.\Delta x$, we obtain:

$$C_P \frac{\partial T}{\partial t} = -\frac{\partial q}{\partial x} \quad \text{(A-21)}$$

Fourier's heat conduction indicated that the evolution of temperature in space is proportional to the heat flowing through unit area q [$W.m^{-2}$] with proportionality coefficient of k [$W.m^{-1}.K^{-1}$], thermal conductivity of the material.

$$q = -k\frac{\partial T}{\partial x} \quad \text{(A-22)}$$

Combining the continuity equation above (Equation 3) with the equation of Fourier's law, we obtain the heat equation or heat diffusion equation:

$$\frac{k}{C_P}\frac{\partial^2 T}{\partial x^2} = \frac{\partial T}{\partial t} \quad \text{(A-23)}$$

The coefficient of thermal diffusivity D_T [m^2/s] is equal to k/C_p in equation 5. Dividing the volumetric heat capacity by the mass density ρ [$kg.m^{-3}$], the specific heat capacity per unit mass is obtained:

$$D_T = \rho \frac{k}{C_P} \tag{A-24}$$

A.2.1. Techniques to Measure the Thermal Diffusivity of Rocks

Laser-flash technique is a non-contact method that avoids the thermal contact resistance between the measuring apparatus and testing specimen (Abdulagatov et al., 2006). Graphite and silver coating on the surfaces of the specimen suppresses the direct radiative heat transfer, so the pure conduction phenomenon is captured. A laser source sends a pulse through the specimen, which has been placed inside a furnace filled with Ar gas, and the temperature evolution inside the specimen is recorded on a detector. When the phonon, generated at the bottom of the specimen, reaches to the top surface, it emits an infrared radiation which is recorded by an Indium Antimonide (InSb) detector. Thermal diffusivity is calculated using the following equation, in which *l* is the specimen thickness (5.13 mm) and t_{50} is the time when the upper surface of the sample reaches half of the maximum temperature (Hirono and Hamada, 2010; Miao et al., 2014):

$$D_T = 0.1388 \frac{l^2}{t_{50}}$$

A.2.2. Thermal Diffusivity of Intact Rocks vs. Temperature

The thermal diffusivity of intact rocks decreases with increasing temperature. It is usually be found to be proportional to the reciprocal of the absolute temperature (Seipold and Gutzeit, 1980). This can be also seen in Equation (6) above that based on experimental observations thermal conductivity usually decreases, the specific heat capacity increases, and the mass density remains almost constant with temperature; hence, the thermal

diffusivity decreases upon temperature rise. 25-44% decrease in thermal conductivity of all three types of rocks results in 42-54% decrease in their thermal diffusivity (Vosteen and Schellschmidt, 2003). The thermal diffusivity of granulite, amphibolite and gneiss decreases by 35-45% with increasing temperature from 20 to 450 ˚C (Ray et al., 2008). Higher decrease on 50-75% is reported for various rocks from different origins for temperature increase of 25-525 ˚C Hanley et al., 1978. A high value of 82% decrease is also reported for clinopyroxenes (Hofmeister and Pertermann, 2008). Another study shows that thermal diffusivity of rocks decreases from 2 to 0.5 mm^2/s upon temperature rise from 25 to 950 ˚C and concludes that the hot middle-lower crust (z = m) acts as an effective insulator (Whittington et al., 2009).

Experimental studies show that the thermal diffusivity of tested rocks decreases with increasing temperature up to 600 ˚C and then stays constant at 600-800 ˚C. This transition in behavior is because of α-β phase transition of quartz (Hirono and Hamada, 2010). However, other experimental studies show that the thermal diffusivity approaches to an asymptote at about 1130 ˚C (Hofmeister and Pertermann, 2008). Figure A.2 shows that the thermal diffusivity of plutonic rocks decreases with increasing temperature and reaches to an asymptote at high temperatures.

Saturation by water increases the thermal diffusivity of rocks. This increase is measured about 24% for granite, basalt, granodiorite, sandstone, marble, limestone, quartzite (Hanley et al., 1978).

A.3. VOLUMETRIC THERMAL EXPANSION

Thermal expansion of a non-metallic solid is determined by two factors: internal stress generated by temperature change and the elastic stiffness of the material. In many

non-metallic crystals both those factors show considerable anisotropy which leads to expansion coefficients and associated Gruneisen parameters varying significantly with temperature and from one material to another (Guy K. White: Thermal expansion of non-metals).

Temperature rise increases the amplitude of lattice vibration and this causes all materials to expand (Yates et al., 1972). During this process, the shape and size of any material change. Coefficient of volumetic thermal expansion for homogeneous materials and cubic crystals is defined as follows:

$$\beta = \frac{1}{V}\left(\frac{\partial V}{\partial T}\right)$$

Crystal structure, temperature and heat capacity of minerals affect their thermal expansion. Temperature, effective stress, porosity, distribution of pores and cracks, and properties of pore-filling fluid affect the thermal expansion of rocks (Siegesmund et al., 2000).

Minerals with cubic crystals expand isotropically. Minerals with other shapes (hexagonal and tetragonal), however, experience anisotropic thermal expansion. Rocks usually contain a variety of different minerals in type, shape, and fabric, i.e., rocks show anisotropic thermal expansion. Quartz and mica cause the major part of thermal expansion in rocks.

Volumetric thermal expansion is higher and more anisotropic for quartz-rich rocks because of higher and more anisotropic thermal expansion of quartz. Mica minerals are sheet-like and orient accordingly to make parallel structure. This special heterogeneous structure favors more anisotropic thermal expansion. The distribution of pores and cracks also affects the value of thermal expansion in different directions. Granite with

anisotropically distributed pores and cracks shows a very anisotropic thermal expansion (Cooper and Simmons, 1977). In layered rock masses or sheet-like minerals, thermal expansion is minimum perpendicular to the orientation of layers. Grains expand and fill the pores and pre-existing fractures, i.e., the thermal expansion manifest less perpendicular to the direction of bedding plane and aligned cracks.

Thermal expansion of most materials increases with increasing temperature due to increasing the amplitude of lattice vibration. The anisotropy of thermal expansion decreases at high temperatures due to preferred orientation of thermal cracks in oppose to randomly distributed original ones (Huotari and Kukkonen, 2004). However, the thermal expansion of minerals and rocks is in the order of 10^{-5} $^{\circ}C^{-1}$ (Tables A.1 and A.2). This means that mass density variation upon increasing temperature can be neglected (Vosteen and Schellschmidt, 2003). Figure A.3 shows the variation of the coefficient of volumetric thermal expansion versus temperature.

The effect of effective confining stress is erratic. For example, the thermal expansion of diorite increases upon loading while that of granite decreases with loading (Larson, 2001). Bulk volumetric thermal expansion was approximated having the volume fraction, Young's modulus and volumetric thermal expansion of constituents (Cooper and Simmons, 1977):

$$\beta = \frac{\sum \beta_i E_i V_i}{\sum E_i V_i}$$

Table A.1. Selected thermal properties of common rocks.

Rock type	**Heat capacity C_p [kJ.kg^{-1}.˚C^{-1}]**	**Coefficient of volumetric thermal expansion β [˚C^{-1}]**	**Thermal diffusivity α [mm^2/s]**
Granite	0.72-0.95 0.77-0.83 (T=99˚C)	8×10^{-6}	0.91-1.90
Granodiorite	0.75-1.02 0.79-0.82 (T=99˚C)		0.52
Gabbro	0.98	5.4×10^{-6}	0.97
Diabase	0.87	5.4×10^{-6}	
Diorite	0.78-1.00 0.80 (T=99˚C)	2.9×10^{-6}	0.64
Andesite		2.9×10^{-6}	
Rhyolite		3.3×10^{-6}	1.9
Basalt	0.84-1.23	2.3×10^{-6}	0.53

Table A.1.Continued. Selected thermal properties of common rocks.

Rock type	Heat capacity C_p [kJ.kg^{-1}.˚C^{-1}]	Coefficient of volumetric thermal expansion β [˚C^{-1}]	Thermal diffusivity α [mm^2/s]
Quartzitic Sandstone	0.85-0.92 0.18-0.26 (T=50˚C)	4.2×10^{-6}	0.72-1.05 1.09-2.36 (T=50˚C)
Shale	0.63		
Siltstone	0.79-0.87		1.08
Gypsum	1.08		0.96-1.10
Rock salt		12×10^{-4}	3.1 (T=50˚C)
Anhydrite			1.7-2.6 (T=50˚C)
Limestone	0.84-0.92	3.3×10^{-6}	
Dolomite	0.80-0.92		0.99
Coal	1.26		
Gneiss	1.10		0.75-1.5
Tonalite gneiss	0.83-0.83 (T=99˚C)	8.1×10^{-6}	1.30
Mica gneiss	0.79-0.85 (T=99˚C)	9.5×10^{-6}	1.17
Marble	0.88	2.9×10^{-6}	
Quartzite		11×10^{-6}	
Schist	1.10		0.96-1.85
Amphibolite	1.13		0.68

Table A.1.Continued. Selected thermal properties of common rocks.

Rock type	Heat capacity C_p [kJ.kg^{-1}.˚C^{-1}]	Coefficient of volumetric thermal expansion β [˚C^{-1}]	Thermal diffusivity α [mm^2/s]
Slate		9×10^{-6}	
Granulite	0.810-0.816 (T=99˚C)		1.2-1.5

Sources: Dane, Jr., 1942; Birch and Clark, 1940a; Birch et al., 1942; Kappelmeyer and Haenel, 1974; Kjorholt et al., 1992; Somerton, 1992; Poelchau et al., 1997; Sharma, 1997; Kukkonen and Lindberg, 1998; Scharli and Rybach, 2001; Cote and Konrad, 2005a; ASHRAE, 2009; Nabelek et al., 2010; Eppelbaum et al., 2014; www.britanica.com; www.engineeringtoolbox.com.

Table A.2. Selected Thermal properties of common rock-forming minerals.

Mineral	**Heat capacity C_p [kJ.kg^{-1}.˚C^{-1}]**	**Coefficient of volumetric thermal expansion β [˚C^{-1}]**
Quartz	0.750-0.753	8×10^{-4} (∥) 14×10^{-4} (⊥)
K-feldspar	Orthoclase: 0.628-0.650 Microcline: 0.670-0.690	5×10^{-4} (∥) 0 (⊥)
Plagioclase (Na/Ca-feldspar)	0.711-0.837	14.14×10^{-6}
Muscovite	0.760	35.37×10^{-6}
Biotite	0.770	
Amphiboles	Hornblende: 0.650-0.750	Hornblende: 600×10^{-4} (∥) 500×10^{-4} (⊥) (T=100 ˚C)

Table A.2.Continued. Selected thermal properties of common rock-forming minerals.

Mineral	Heat capacity C_p [$kJ.kg^{-1}.^{\circ}C^{-1}$]	Coefficient of volumetric thermal expansion β [$^{\circ}C^{-1}$]
Pyroxene	Enstatite: 0.800 (T=60˚C) Diopside: 0.700-0.750	
Olivine	Forsterite: 0.980 Fayalite: 0.840	
Zircon	0.610 (T=60˚C)	
Garnet	0.740 (T=58˚C)	15.46×10^{-6}
Sillimanite	0.743 (T=0˚C)	13.29×10^{-6}
Calcite	0.800-0.880	400×10^{-4} (∥) 1900×10^{-4} (⊥) (T=100 ˚C)
Dolomite		22.58×10^{-6}
Gypsum		72.5×10^{-6}

Table A.2.Continued. Selected thermal properties of common rock-forming minerals.

Mineral	Heat capacity C_p [kJ.kg^{-1}.˚C^{-1}]	Coefficient of volumetric thermal expansion β [˚C^{-1}]
Magnetite	0.600 (T=0˚C)	
Hematite	0.620-0.628	25×10^{-6}
Halite		12×10^{-4}
Fluorite	0.900	
Pyrite	0.500-0.520	
Chalcopyrite	0.540 (T=50˚C)	
Sphalerite	0.450 (T=0˚C)	
Galena	0.207 (T=0˚C)	

Sources: Birch and Clark, 1940a; Birch and Clark, 1940b; Sass, 1965; Horai and Simmons, 1969; Skinner, 1969; Horai, 1971; Cermak and Rybach, 1982; Rybach and Cermak, 1987; Diment and Pratt, 1988; ASHRAE, 2009; Fei, 1995.

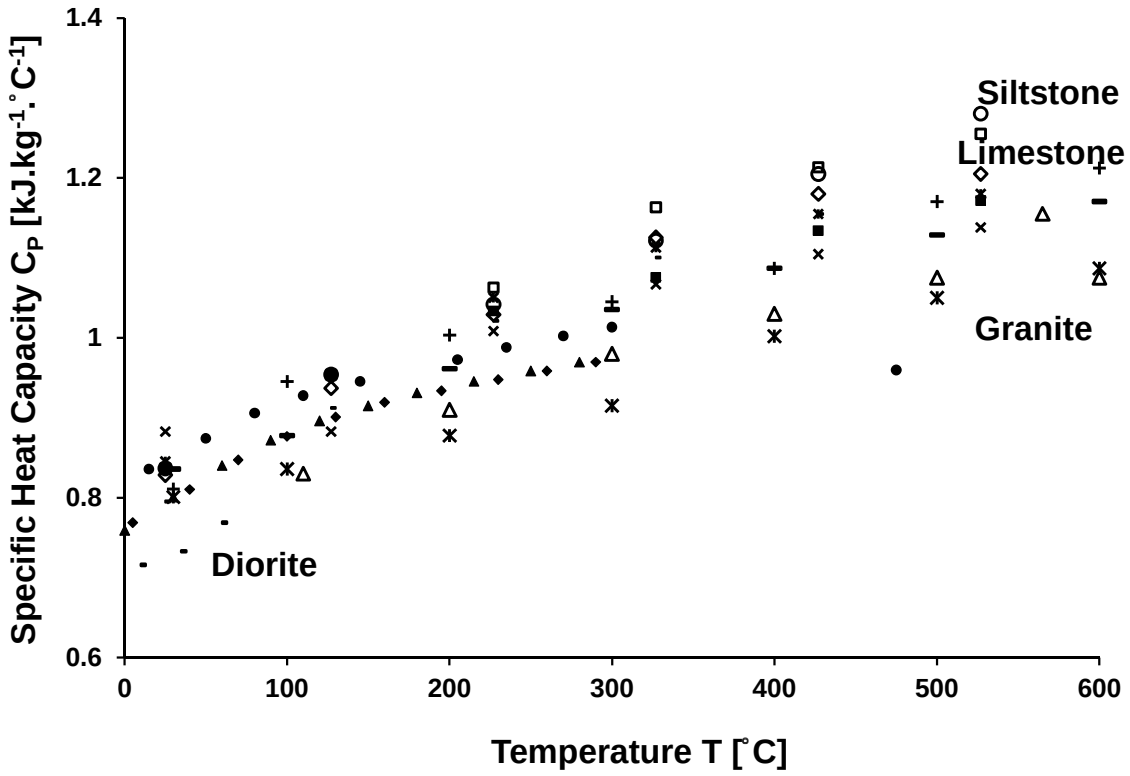

Figure A.1. The specific heat capacity of rocks versus temperature – Data from: Kjorholt et al., 1992; Somerton, 1992; Vosteen and Schellschmidt, 2003; Dwivedi et al., 2008; Hirono and Hamada, 2010.

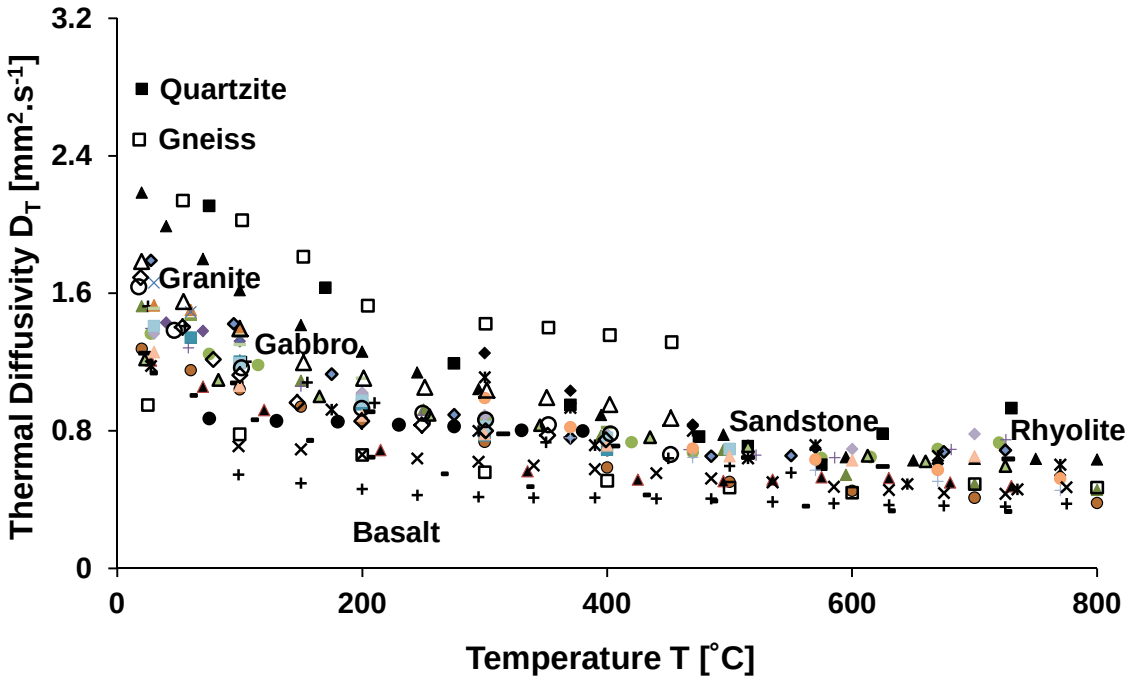

Figure A.2. The thermal diffusivity of rocks versus temperature – Data from: Hanley et al., 1978; Durham and Abey, 1981b; Seipold, 1998; Dwivedi et al., 2008; Whittington et al., 2009; Hirono and Hamada, 2010; Eppelbaum et al., 2014; Miao et al., 2014.

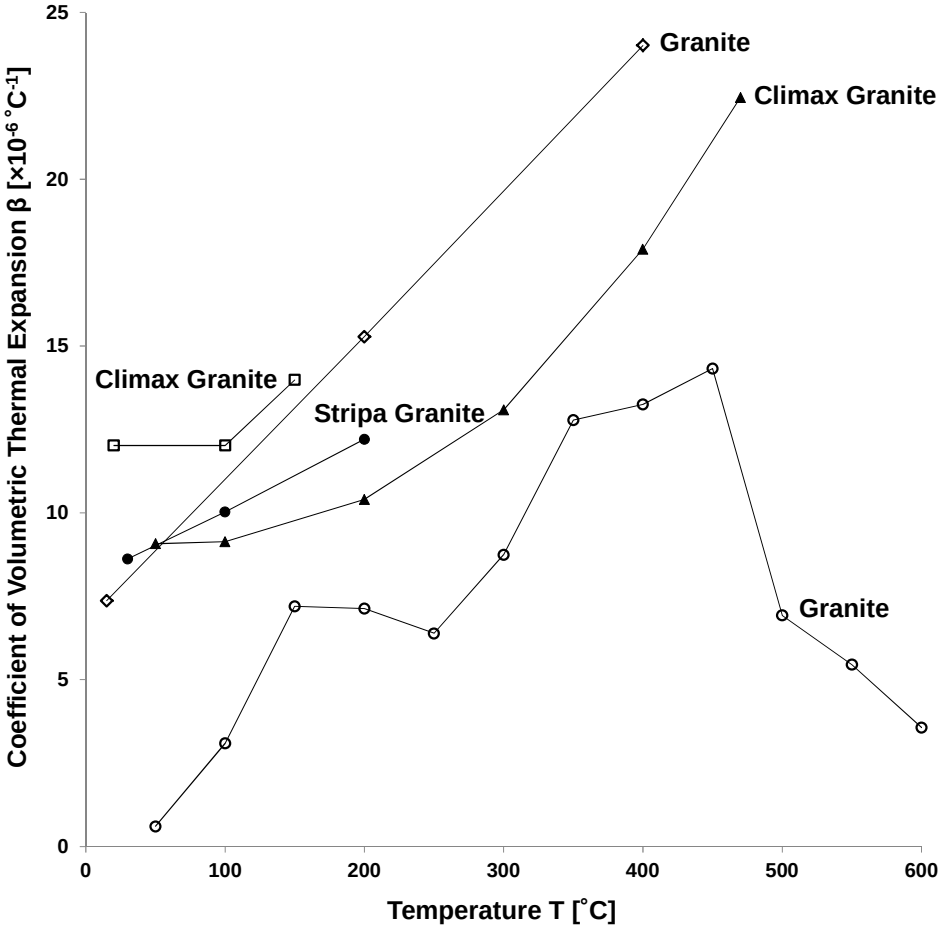

Figure A.3. The coefficient of volumetric thermal expansion versus temperature – Data from: Heuze, 1983; Zhao et al., 2012.

A.4. REFERENCES

Abdulagatov, I. M., Emirov, S. N., Abdulagatova, Z. Z., and Askerov, S. Y. (2006). "Effect of Pressure and Temperature on the Thermal Conductivity of Rocks." *Journal of Chemical and Engineering Data*, 51(1), 22-33.

ASHRAE (2009). *ASHRAE Handbook - Fundamentals (I-P Edition)*, American Society of Heating, Refrigerating and Air-Conditioning Engineers, Inc.

Birch, F., and Clark, H. (1940a). "The Thermal Conductivity of Rocks and Its Dependence upon Temperature and Composition-Part 1." *American Journal of Science*, 238(9), 613-635.

Birch, F., and Clark, H. (1940b). "The Thermal Conductivity of Rocks and Its Dependence upon Temperature and Composition-Part 2." *American Journal of Science*, 238(8), 529-558.

Birch, F., Schairer, J. F., and Spicer, H. C. e. (1942). "Handbook of Physical Constants." *Special Papers (Geological Society of America)*.(36), 1-325.

Campbell, G. S., Calissendorff, C., and Williams, J. H. (1991). "Probe for Measuring Soil Specific Heat Using a Heat Pulse Method." *Soil Science Society of America Journal*, 55(1), 291-293.

Carslaw, H. S., and Jaeger, J. C. (1959). *Conduction of Heat in Solids*, Clarendon Press, Oxford.

Cermak, V., and Rybach, L. (1982). "Thermal Conductivity and Specific Heat of Minerals and Rocks." *Physical Properties of Rocks*, Springer, Berlin, Heidelberg, 213-256.

Cote, J., and Konrad, J. M. (2005a). "Thermal Conductivity of Base-Course Materials." *Canadian Geotechnical Journal*, 42(1), 61-78.

Diment, W. H., and Pratt, H. R. (1988). *Thermal Conductivity of Some Rock-Forming Minerals: A Tabulation*, Denver, CO : U.S. Geological Survey ; [Denver, Colo. : Books and Open-File Reports Section, distributor], 1988.

Durham, W. B., and Abey, A. E. (1981b). "Thermal Conductivity and Diffusivity of Climax Stock Quartz Monazite at High Pressure and Temperature." Lawrence Livermore National Laboratory Report.

Dwivedi, R. D., Goel, R. K., Prasad, V. V. R., and Sinha, A. (2008). "Thermo-Mechanical Properties of Indian and other Granites." *International Journal of Rock Mechanics and Mining Sciences*, 45(3), 303-315.

England, P. C. (1978). "Some Thermal Considerations of Alpine Metamorphism - Past, Present and Future." *Tectonophysics*, 46(1-2), 21-40.

Eppelbaum, L., Kutasov, I., and Pilchin, A. (2014). "Applied Geothermics." <https://symbiose.uqo.ca/apps/LoginSigparb/LoginPourRessources.aspx?url=http://dx.doi.org/10.1007/978-3-642-34023-9>.

Hanley, E. J., Dewitt, D. P., and Roy, R. F. (1978). "The Thermal Diffusivity of Eight Well-Characterized Rocks for the Temperature Range 300–1000 K." *Engineering Geology*, 12, 31-47.

Heuze, F. E. (1983). "High-Temperature Mechanical, Physical and Thermal-Properties of Granitic-Rocks - A Review." *International Journal of Rock Mechanics and Mining Sciences*, 20(1), 3-10.

Hirono, T., and Hamada, Y. (2010). "Specific Heat Capacity and Thermal Diffusivity and their Temperature Dependencies in a Rock Sample from Adjacent to the Taiwan Chelungpu Fault." *Journal of Geophysical Research-Solid Earth*, 115.

Hofmeister, A. M., and Pertermann, M. (2008). "Thermal Diffusivity of Clinopyroxenes at Elevated Temperature." *European Journal of Mineralogy*, 20(4), 537-549.

Horai, K. (1971). "Thermal Conductivity of Rock-Forming Minerals." *Journal of Geophysical Research*, 76(5), 1278-1308.

Horai, K.-i., and Simmons, G. (1969). "Thermal Conductivity of Rock-Forming Minerals." *Earth and Planetary Science Letters*, 6, 359-368.

Kappelmeyer, O., and Haenel, R. (1974). *Geothermics with Special Reference to Application*, Berlin, Gebrüder Borntraeger, 1974.

Kelley, K. K. (1941). "Contributions to the Data on Theoretical Metallurgy." *the entropies of inorganic substances; revision (1940) of data and methods of calculation*, 434, 1-115.

King, M., and Somerton, W. (1960). "Measurement and Calculation of Specific Heats of rocks." Lawrence Berkeley Laboratory, California, USA, 12.

Kjorholt, H., Dahlo, T. S., and Broch, E. (1992). *Geotechnical Design of Air-Cushion Surge Chambers*.

Kluitenberg, G. J., Ham, J. M., and Bristow, K. L. (1993). "Error Analysis of Heat Pulse Method for Measuring Soil Volumetric Heat Capacity." *Soil Science Society of America Journal*, 57(6), 1444-1451.

Kukkonen, I., and Lindberg, A. (1998). "Thermal Properties of Rocks at the Investigation Sites: Measured and Calculated Thermal Conductivity, Specific Heat Capacity and Thermal Diffusivity." L. Eskola, ed., Posiva, Finland, 32.

Miao, S. Q., Li, H. P., and Chen, G. (2014). "Temperature Dependence of Thermal Diffusivity, Specific Heat Capacity, and Thermal Conductivity for Several Types of Rocks." *Journal of Thermal Analysis and Calorimetry*, 115(2), 1057-1063.

Nabelek, P. I., Hofmeister, A. M., and Whittington, A. G. (2012). "The Influence of Temperature-Dependent Thermal Diffusivity on the Conductive Cooling Rates of Plutons and Temperature-Time Paths in Contact Aureoles." *Earth and Planetary Science Letters*, 317, 157-164.

Nabelek, P. I., Whittington, A. G., and Hofmeister, A. M. (2010). "Strain Heating as a Mechanism for Partial Melting and Ultrahigh Temperature Metamorphism in Convergent Orogens: Implications of Temperature-Dependent Thermal Diffusivity and Rheology." *Journal of Geophysical Research - Part B - Solid Earth*, 115(B12), (17 pp.).

Poelchau, H. S., Baker, D. R., Hantschel, T., Horsfield, B., and Wygrala, B. (1997). "Basin Simulation and the Design of the Conceptual Basin Model." *Petroleum and Basin Evolution*, D. Welte, B. Horsfield, and D. Baker, eds., Springer Berlin Heidelberg, 3-70.

Ray, L., Roy, S., and Srinivasan, R. (2008). "High Radiogenic Heat Production in the Kerala Khondalite Block, Southern Granulite Province, India." *International Journal of Earth Sciences*, 97(2), 257-267.

Richet, P. (2001). *The Physical Basis of Thermodynamics: With Applications to Chemistry*, Springer US.

Rybach, L., and Cermak, V. (1987). "The Depth Dependence of Heat-Production in the Continental Lithosphere, Derived from Seismic Velocities." *Geophysical Research Letters*, 14(3), 311-313.

Sass, J. H. (1965). "The Thermal Conductivity of Fifteen Feldspar Specimens." *Journal of Geophysical Research*, 70(16), 4064.

Scharli, U., and Rybach, L. (2001). "Determination of Specific Heat Capacity on Rock Fragments." *Geothermics*, 30(1), 93-110.

Seipold, U. (1998). "Temperature Dependence of Thermal Transport Properties of Crystalline Rocks - A General Law." *Tectonophysics*, 291(1-4), 161-171.

Seipold, U., and Gutzeit, W. (1980). "Measurements of the Thermal-Properties of Rocks under Extreme Conditions." *Physics of the Earth and Planetary Interiors*, 22, 272-276.

Sharma, P. V. (1997). *Environmental and Engineering Geophysics*, Cambridge University Press.

Somerton, W. H. (1992). *Thermal Properties and Temperature-Related Behavior of Rock/Fluid Systems*, Elsevier, California.

Somerton, W. H., and Selim, M. A. (1961). "Additional Thermal Data for Porous Rocks-Thermal Expansion and Heat of Reaction." *Society of Petroleum Engineers Journal*, 1(4), 249-253.

Vosteen, H. D., and Schellschmidt, R. (2003). "Influence of Temperature on Thermal Conductivity, Thermal Capacity and Thermal Diffusivity for Different Types of Rock." *Physics and Chemistry of the Earth*, 28(9-11), 499-509.

Whittington, A. G., Hofmeister, A. M., and Nabelek, P. I. (2009). "Temperature-Dependent Thermal Diffusivity of the Earth's Crust and Implications for Magmatism." *Nature*, 458(7236), 319-321.

Yates, B., Cooper, R. F., and Pojur, A. F. (1972). "Thermal-Expansion at Elevated-Temperatures .2. Aluminum-Oxide - Experimental-Data between 100 and 800 K and their Analysis." *Journal of Physics Part C Solid State Physics*, 5(10), 1046-&.

Zhao, Y., Wan, Z., Feng, Z., Yang, D., Zhang, Y., and Qu, F. (2012). "Triaxial Compression System for Rock Testing under High Temperature and High Pressure." *International Journal of Rock Mechanics and Mining Sciences*, 52, 132-138.

APPENDIX B

DESIGN SHEETS FOR HIGH STRESS AND HIGH TEMPERATURE TESTING DEVICE

All parts are made of stainless steel:

$\sigma_{yield} := 200 \cdot MPa$

$E := 200 \cdot GPa$

$\tau_f := \frac{\sigma_{yield}}{2}$

$\nu := 0.3$

Assumed cell geometric characteristics:

$A := D^2 \cdot \frac{\pi}{4}$

$A = 4.56 \times 10^{-3}\ m^2$

Vertical loading using a hydraulic cylinder:

$M := 10000 \cdot kg$

$F := M \cdot g$

$F = 9.807 \times 10^4\ N$

Vertical and horizontal stresses:

$\sigma_{vertical} := \frac{F}{A} = 2.15 \times 10^7\ Pa$

$K_o := 0.5$

$\sigma_{horizontal} := K_o \cdot \sigma_{vertical} = 1.075 \times 10^7\ Pa$

Loading frame: Upper Beam

Assumed beam geometric characteristics:

Beam length: $L := 5.85 \cdot in$

Beam width: $b := 1.5 \cdot in$

Beam Height: $h := 2 \cdot in$

Uniform loading centered on the beam:

Load width: $d := 2 \cdot in$

Total force applied: $F = 9.807 \times 10^{4} N$

Total stress applied: $q := \frac{F}{d \cdot b}$

$q = 5.067 \times 10^{7} Pa$

Total load per lenght: $w := q \cdot b$

$w = 1.93 \times 10^{6} \frac{kg}{s^2}$

Given

Supports reaction force: $R_A := 4000N$

$R_B := 30000N$

Vertical force equilibrium: $R_A + R_B = F$

Bending moment equilibrium: $F \cdot \frac{L}{2} = R_B \cdot L$

$$Find(R_A, R_B) = \begin{pmatrix} 4.903 \times 10^{4} \\ 4.903 \times 10^{4} \end{pmatrix} N$$

Shear force and bending moment:

For $0 < x < 0.0489$ m

$x_1 := 0\text{m}, 0.001\text{m}.. 0.049\text{m}$

$V_1 := \frac{F}{2}$

$V_1 = 4.903 \times 10^4 \text{N}$

$M_1(x_1) := V_1 \cdot x_1$

$M_1(0) = 0$

$M_1(0.049 \cdot \text{m}) = 2.403 \times 10^3 \text{J}$

For $0.0489\text{ m} < x < 0.0997$ m

$x_2 := 0\text{m}, 0.001\text{m}.. 0.0508\text{m}$

$V_2(x_2) := \frac{F}{2} - q \cdot b \cdot x_2$

$V_2(0\text{m}) = 4.903 \times 10^4 \text{N}$

$V_2(0.0254\text{m}) = 0\,\text{N}$

$V_2(0.0508\text{m}) = -4.903 \times 10^4 \text{N}$

$V_{max} := V_2(0\text{m}) = 4.903 \times 10^4 \text{N}$

$M_2(x_2) := M_1(0.0489\text{m}) + \frac{F}{2} \cdot x_2 - \left(q \cdot b \cdot x_2^{\,2}\right) + \frac{q \cdot b \cdot x_2^{\,2}}{2}$

$M_2(0\text{m}) = 2.398 \times 10^3 \text{J}$

$M_2(0.0254\text{m}) = 3.02 \times 10^3 \text{J}$

$M_2(0.0508\text{m}) = 2.398 \times 10^3 \text{J}$

$M_{max} := M_2(0.0254\text{m}) = 3.02 \times 10^3 \text{J}$

For 0 < x < 0.0489 m (and reverse for 0.0997 < x < 0.1486 m):

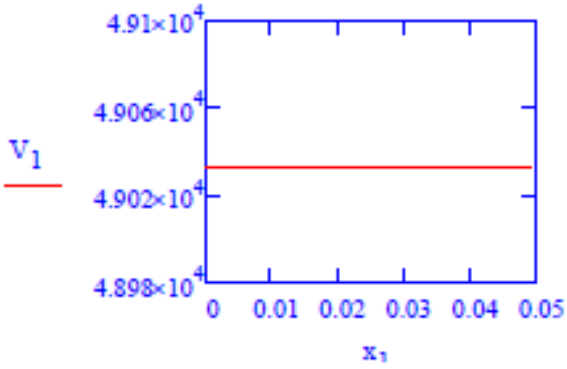

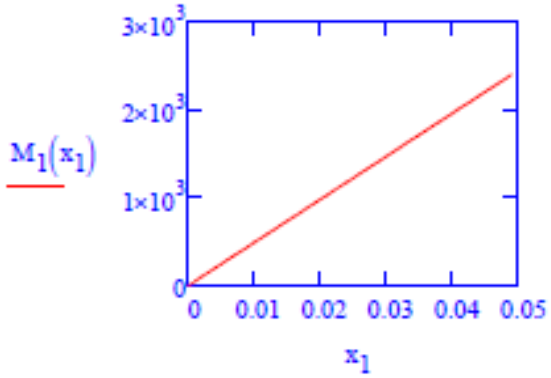

For 0.0489 m < x < 0.0997 m (part of the beam under the uniform load: 0.0508 m):

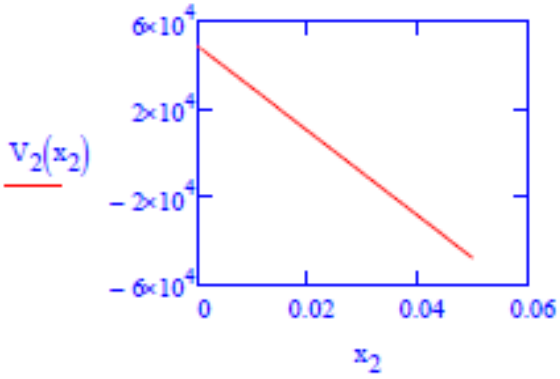

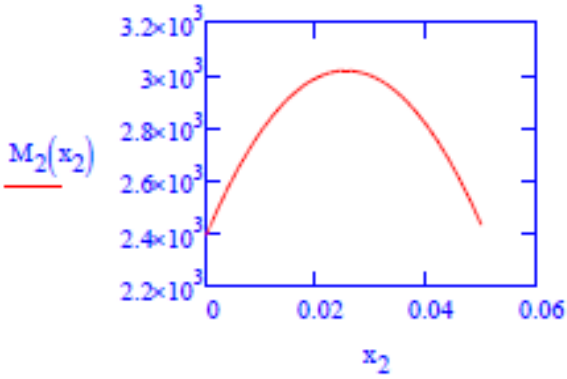

Neutral fiber on the beam cross-section:

$$N_f := \frac{h}{2}$$

$$N_f = 0.025\,m$$

Area moment of inertia of the beam cross-section:

$$I := \frac{b \cdot h^3}{12}$$

$$I = 4.162 \times 10^{-7}\,m^4$$

Maximum tensile stress caused by bending moment:

$$\sigma_{max} := \frac{M_{max} \cdot N_f}{I}$$

$$\sigma_{max} = 1.843 \times 10^{8}\,Pa$$

Maximum shear stress:

$$\tau_{max} := \frac{V_{max}}{b \cdot h}$$

$$\tau_{max} = 2.533 \times 10^{7}\,Pa$$

Check the beam for the tensile stress caused by bending moment:

$$\sigma_{max} = 167\ MPa < \sigma_{yield} = 200\ MPa$$

Check the beam for shear stress:

$$\tau_{max} = 23\ MPa < \tau_f = 100\ MPa$$

Rods under tension:

Assumed rod diameter:

$$DD := 1 \cdot in$$

Applied tensile stress:

$$\sigma_t := \frac{\frac{F}{2}}{\frac{\pi}{4} \cdot DD^2}$$

$$\sigma_t = 9.677 \times 10^7 \, Pa$$

check the rod for tension:

$$\sigma_t = 97 \text{ MPa} < \sigma_{yield} = 200 \text{ MPa}$$

Nut height:

$$hh := \frac{DD}{2}$$

Acting shear stress:

$$\tau_{act} := \frac{\frac{F}{2}}{\pi \cdot DD \cdot hh}$$

$$\tau_{act} = 4.838 \times 10^7 \cdot Pa$$

Check the threads of the nut and the rod for the shear stress:

$$\tau_{act} = 48 \text{ MPa} < \tau_f = 100 \text{ MPa}$$

Thickness of the cell wall to have zero lateral strain:

Inner radius of the cell:

$$r_i := \frac{D}{2}$$

$$r_i = 0.038\,m$$

Stress applied on the wall inside and outside of the cell:

$$P_i := \sigma_{horizontal}$$

$$P_i = 1.075 \times 10^7\,Pa$$

$$P_o := 0.1 \cdot MPa$$

Radial strain is limited to 0.0001 on the inner wall:

$$r := 0.0381 \cdot m$$

$$\varepsilon_r := -(10)^{-4}$$

$$r_o := \sqrt{\frac{r_i^2\left(E \cdot \varepsilon_r \cdot r^2 + 0.7 \cdot r^2 \cdot P_i\right)}{1.3 \cdot r_i^2\left(P_i - P_o\right) + E \cdot \varepsilon_r \cdot r^2 + 0.7 \cdot r^2 \cdot P_o}}$$

Outer radius of the cell:

$$r_o = 0.055\,m$$

Thickness of the cell wall:

$$t := r_o - r_i$$

$$t = 0.016\,m$$

Given

$r := 0.06m \qquad \sigma_r := -10MPa \qquad \sigma_\theta := 3MPa$

Radial stress in a thick-walled cylinder: $\sigma_r = \frac{\left(r_i^2 \cdot P_i - r_o^2 \cdot P_o\right)}{\left(r_o^2 - r_i^2\right)} - \frac{\left(P_i - P_o\right) r_i^2 \cdot r_o^2}{\left(r_o^2 - r_i^2\right) \cdot r^2}$

Hoop stress in a thick-walled cylinder: $\sigma_\theta = \frac{\left(r_i^2 \cdot P_i - r_o^2 \cdot P_o\right)}{\left(r_o^2 - r_i^2\right)} + \frac{\left(P_i - P_o\right) r_i^2 \cdot r_o^2}{\left(r_o^2 - r_i^2\right) \cdot r^2}$

$$\text{Find}\left(\sigma_r, \sigma_\theta\right) = \begin{pmatrix} -1.075 \times 10^7 \\ 2.495 \times 10^7 \end{pmatrix} Pa$$

$\sigma := \sigma_r - \nu \cdot \sigma_\theta$

$\varepsilon_r := E \cdot \varepsilon_r$

$\sigma = -2 \times 10^7 Pa$

$r := 0.0509m$

$A := \frac{r_i^2 \cdot P_i - r_o^2 \cdot P_o}{r_o^2 - r_i^2}$

$B := \frac{\left(P_i - P_o\right) \cdot r_i^2 \cdot r_o^2}{\left(r_o^2 - r_i^2\right) \cdot r^2}$

$\sigma_r := A - B$

$\sigma_\theta := A + B$

$S := \sigma_r - \nu \cdot \sigma_\theta := 0.7 \cdot A - 1.3 \cdot B$

$S := \varepsilon_r \cdot E$

$S = -2 \times 10^7 Pa$

$$\frac{\left(r_i^2 \cdot P_i - r_o^2 \cdot P_o\right)}{\left(r_o^2 - r_i^2\right)} - \frac{\left(P_i - P_o\right) r_i^2 \cdot r_o^2}{\left(r_o^2 - r_i^2\right) \cdot r^2} - \nu \cdot \left[\frac{\left(r_i^2 \cdot P_i - r_o^2 \cdot P_o\right)}{\left(r_o^2 - r_i^2\right)} + \frac{\left(P_i - P_o\right) r_i^2 \cdot r_o^2}{\left(r_o^2 - r_i^2\right) \cdot r^2} \right] - E \cdot \varepsilon$$

Predict the deformation of the specimen:

Experimental results on dry quartzitic sand:

$\sigma_1 := 82 \cdot kPa$ $\varepsilon_1 := 0.00275$

$\sigma_2 := 2656 \cdot kPa$ $\varepsilon_2 := 0.02111$

$$C_c := \frac{\varepsilon_2 - \varepsilon_1}{\log\left(\frac{\sigma_2}{\sigma_1}\right)}$$

$C_c = 0.012$

$\sigma_3 := 20 \cdot MPa$

$$\varepsilon_3 := C_c \cdot \log\left(\frac{\sigma_3}{\sigma_2}\right) + \varepsilon_2$$

$\varepsilon_3 = 0.032$

$h_o := 3in$

$\Delta h := h_o \cdot \varepsilon_3$

$\Delta h = 2.421 \times 10^{-3}\, m$

Rough Checking:

$\sigma := 22 \cdot MPa$

$d := 3 \cdot in$

$F := \pi \cdot \frac{d^2}{4} \cdot \sigma$ $\quad F = 1.003 \times 10^5 N$

$\sigma y := 215 \cdot MPa$ $\quad drod := \left(\frac{F}{\sigma y} \cdot \frac{4}{\pi} \right)^{\frac{1}{2}}$ $\quad drod = 24.375 \cdot mm$

$\varepsilon t := 10^{-4}$ $\quad E := 200 \cdot GPa$ $\quad t := \frac{\sigma \cdot 0.5 \cdot d}{2 \cdot \varepsilon t \cdot E}$ $\quad t = 20.955 \cdot mm$

HRS MT-1026 & A-106

http://www.specialtypipe.com/steel-pipe-and-tube-inventory/inventory-results.aspx?od=5

cross beam

$b := 2 \cdot in$ $\quad L := 6 \cdot in$ $\quad h := \sqrt{\frac{3}{2} \cdot \frac{F \cdot L}{\sigma y \cdot b}}$ $\quad h = 1.804 \cdot in$ $\quad b = 2 \cdot in$ $\quad L := 8.5 \cdot in$

base $\quad h := 1.75$ $\quad b := 8.5$ $\quad L := 8.5 \cdot in$

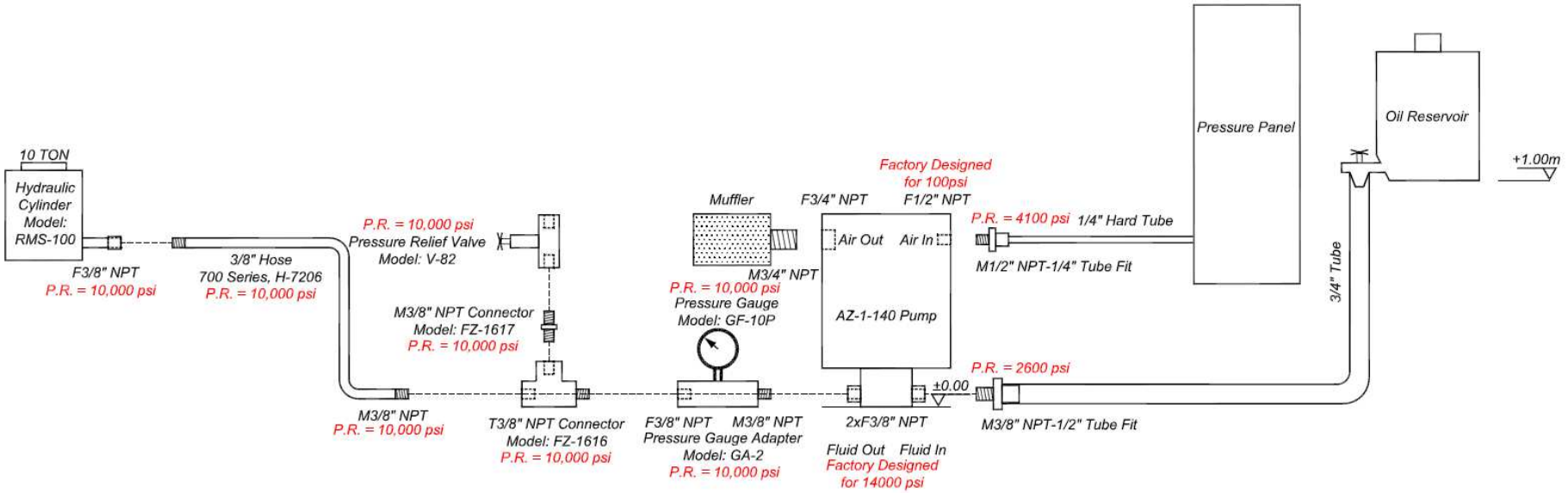

Figure B.1. Pressure circuit and used products for the high stress and high temperature testing device (developed for testing oil sand).